Copyright

by

Benjamin Arledge Fulcher

2012

The Thesis Committee for Benjamin Arledge Fulcher
Certifies that this is the approved version of the following thesis:

Evaluation of Systems Containing Negative Stiffness Elements for Vibration and Shock Isolation

APPROVED BY
SUPERVISING COMMITTEE:

Carolyn C. Seepersad, Supervisor

Preston S. Wilson, Co-Supervisor

Michael R. Haberman, Co-Supervisor

Evaluation of Systems Containing Negative Stiffness Elements for Vibration and Shock Isolation

by

Benjamin Arledge Fulcher, B.S.M.E

Thesis

Presented to the Faculty of the Graduate School of

The University of Texas at Austin

in Partial Fulfillment

of the Requirements

for the Degree of

Master of Science in Engineering

The University of Texas at Austin

May 2012

Dedication

To my family and to my loving wife, Meagan.

Acknowledgements

It was a pleasure to work with such a knowledgeable and friendly team throughout the project. Each member contributed in various ways to my research, providing valuable insights which were essential to my work.

I first wish to express my appreciation to Dr. Carolyn Seepersad for her continued support during my research. She was always willing to offer advice, and her knowledge of design was very helpful. I would also like express my appreciation to Dr. Michael Haberman for his constant willingness to help me answer any questions regarding dynamic testing and analysis. I would like to thank Dr. Preston S. Wilson for sharing his modeling expertise and knowledge of system dynamics whenever needed. I wish to thank Dr. David Shahan for providing many insights across a large range of topics, many of which are key components of this research. Without the help of Dr. Shahan, specifically in modeling the behavior of buckled beams, much of the following work would not have been possible.

I would like to thank Mark Phillips, Nicole Guckert, and Courtney Shell, who provided much support in working with the Selective Laser Sintering machine. I appreciate the support of Dr. Moss Shimek and my colleagues Jordan Matthews, Danny Johnson, Timothy Klatt, Pete Backlund, Julia O'Rourke, Cassandra Telenko, Nathan Putnam, and Ben Gully who provided useful feedback to my presentations. Finally, I would like to thank my wife, Meagan, and my family for providing much personal support throughout the project.

BENJAMIN ARLEDGE FULCHER

The University of Texas at Austin

May 2012

Abstract

Evaluation of Systems Containing Negative Stiffness Elements for Vibration and Shock Isolation

Benjamin Arledge Fulcher, MSE

The University of Texas at Austin, 2012

Supervisors: Carolyn C. Seepersad

Michael R. Haberman

Preston S. Wilson

The research presented in this thesis focuses on the modeling, design, and experimentation of systems containing negative stiffness mechanisms for both vibration and shock isolation. The negative stiffness element studied in this research is an axially compressed beam. If a beam is axially compressed past a critical value, it becomes bistable with a region of negative stiffness in the transverse direction. By constraining a buckled beam in its metastable position through attaching a stiff linear spring in mechanical parallel, the resulting system can reach a low level of dynamic stiffness and therefore provide vibration isolation at low frequencies, while also maintaining a high load-carrying capacity. In previous research, a system containing an axially compressed beam was modeled and tested for vibration isolation [7]. In the current research, variations of this model were studied and tested for both vibration and shock isolation. Furthermore, the mathematical model used to represent the compressed beam in [7] was

improved and expanded in current research. Specifically, the behavior exhibited by buckled beams of transitioning into higher-mode shapes when placed under transverse displacement was incorporated into the model of the beam. The piecewise, nonlinear transverse behavior exhibited by a first-mode buckled beam with a higher-mode transition provides the ability of a system to mimic an ideal constant-force shock isolator.

Prototypes manufactured through Selective Laser Sintering were dynamically tested using a shaker table. Vibration testing confirmed the ability of a system containing a constrained negative stiffness element to provide enhanced vibration isolation results with increasing axial compression on a beam. However, the results were limited by the high sensitivity of buckled beam behavior to geometrical and boundary condition imperfections. Shock testing confirmed the ability of a system containing a buckled beam with a higher-mode transition to mimic the theoretically ideal constant-force shock isolator.

Table of Contents

List of Tables

List of Figures

Chapter 1

Introduction

1.1 MOTIVATION

Vibrations and shocks occur frequently in nearly every environment. The response of a mechanical system to these loading types can be harmful if not taken into account during the design process. The Mark V Special Operations Craft, a boat designed to carry Special Operations Forces at high speeds across long distances, encounters high levels of vibration and shock loading due to the slamming of waves against the hull of the boat. This loading can cause injuries and discomfort to the passengers if not properly accounted for. The photograph in Figure 1.1 shows an image of the Mark V Special Operations Craft.

Figure 1.1. *Mark V Special Operations Craft [1]*

In order to alleviate issues such as injury of personnel in the Mark V due to shock and vibration, the Defense Advanced Research Projects Agency, or DARPA, has initiated an effort to passively mitigate various loading types under one system through assemblies of Structural Logic Units, or SLUs. SLUs represent any passive, mechanical component with a corresponding constitutive relationship that describes its dynamic behavior. Springs, dampers, and masses are basic linear SLUs, whereas other mechanical components such as buckled beams represent SLUs with more complicated nonlinear behavior. An SLU Assembly, or SLUA, could ideally respond differently and beneficially to alternate loading types. For example, an SLUA could be designed to protect a person from vibratory loading in one instant and shock loading in another. Nonlinear behavior is needed to provide the capability of passively altering the response of a system to accommodate various loading types. Two systems containing nonlinear SLUs that display negative stiffness are studied in this thesis. One system is designed to decouple a mass from vibratory loading and the other is designed to decouple a mass from shock loading.

In the design of traditional linear vibration isolation devices, one must compromise between achieving levels of low stiffness and maintaining the ability to support large loads. Negative stiffness has been studied and put to use in recent years as a method of reaching both goals. For example, a stiff supporting spring can be used to support a large load, requiring small levels of compression to do so. The addition of a negative stiffness element in parallel with this supporting spring lowers the overall dynamic stiffness of the system, providing improved vibration isolation characteristics. This lowering of the dynamic stiffness does not detract from the load carrying capacity of the system, as the supporting spring fully carries the load even with the addition of negative stiffness.

Negative stiffness is becoming, or may already be, a well-known term within the field of dynamics. Minus K Technology[1] is one company which has put negative stiffness to use in recent years to produce state of the art vibration isolation tables [9]. By exploiting this quality of various nonlinear components, many have demonstrated the ability to vastly improve vibration isolation performances [5],[6],[10],[11]. Theory suggests that bistable components containing negative stiffness could improve shock isolation performances as well.

1.2 Previous Work

In vibration applications, the use of nonlinear spring behavior has been shown to enhance vibration isolation performance while still enabling a high level of static stiffness. Negative-Stiffness-Mechanisms or NSMs have been successfully used in parallel with linear elements to produce this phenomenon [4]. Bistable elements, which can achieve stability in two different states, are examples of NSMs. A unique characteristic of bistable elements is a region of negative stiffness, or negative slope, in the force-displacement constitutive relationship. A well-known bistable mechanism is a buckled beam, as illustrated in Figure 1.2.

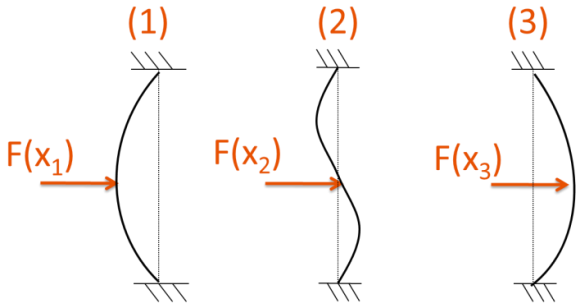

Figure 1.2. *Bistable element [7]*

[1] www.minusk.com

States (1) and (3) shown in Figure 1.2 are the two stable equilibriums of a buckled beam. State (2) is a meta-stable state, which is stable in a mathematical sense but not from a practical standpoint, as any minute imperfections or forces will cause the beam to snap to either of states (1) or (3). For small amounts of compression on the endpoints of the beam, the transverse constitutive relationship can be approximated by a third-order polynomial. For buckled beams, this third-order polynomial contains a region of negative stiffness, as shown in Figure 1.3.

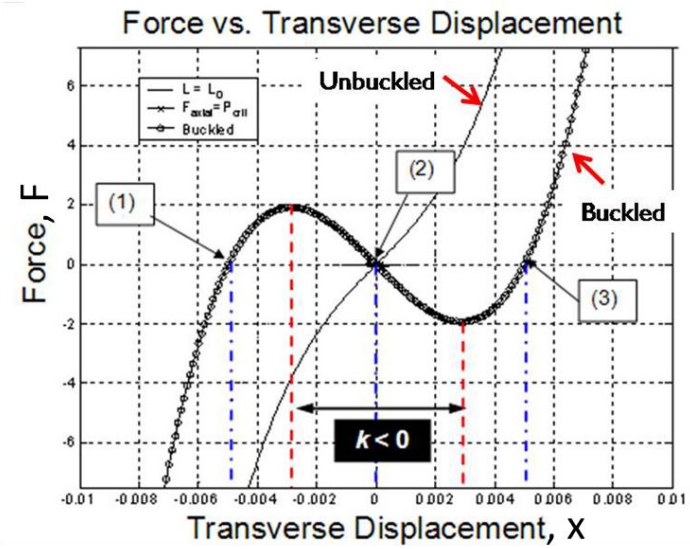

Figure 1.3. *Transverse force-displacement constitutive relationship of a buckled beam [8]*

Also shown in Figure 1.3 is the force versus displacement relationship of an unbuckled beam. As compressive forces are applied to the endpoints of the beam, the *F(x)* curve transitions from the unbuckled curve to the buckled curve. States (1), (2), and (3) shown in Figure 1.3 directly correspond with those shown in Figure 1.2. At each of the states, zero force acts on the beam, corresponding to stability in states (1) and (3) and meta-stability in state (2). If an infinitesimal force is applied to the midpoint of the beam while

it rests in either of states (1) and (3), the beam will deflect and provide an equal and opposite reaction force. However, if an infinitesimal force is applied the midpoint of the beam while it rests in state (2), the beam must snap to one of its stable configurations in order to reach equilibrium and oppose the infinitesimal force.

Minus K Technology, a California-based company, has successfully capitalized on the use of the negative stiffness region in buckled beams to produce passive vibration isolation systems with high performance [4]. A general representation of the concept employed by Minus K can be seen in Figure 1.4.

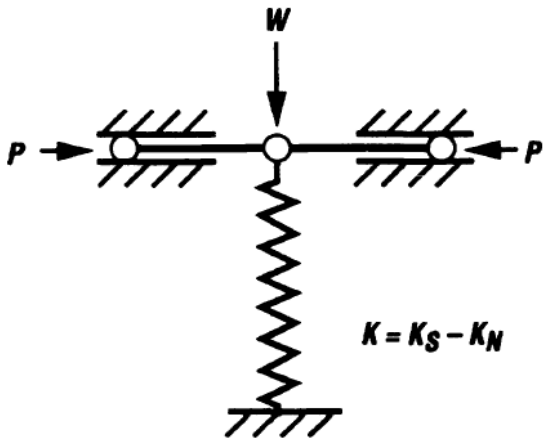

Figure 1.4. *Minus K system concept [4]*

The concept depicted in Figure 1.4 consists of a constrained beam in parallel with a spring. Once weight W is placed on the spring and fully supported, compressive forces P are placed on the ends of the beam to reduce the transverse stiffness of the beam. With enough force P, the beam enters into a negative stiffness regime, thereby cancelling some of the positive stiffness provided by the spring. The overall system stiffness, then, is equal to K, the positive stiffness minus the negative stiffness. In this case, K is the

dynamic stiffness of the system, whereas the static stiffness is the stiffness of the spring itself. Thus, the system is able to achieve low levels of dynamic stiffness and resonance frequency, while still maintaining high levels of static stiffness and the ability to support a relatively heavy load. In fact, some refer to this type of system as a "high-static—low-dynamic stiffness", or HSLDS, system [5],[6]. A particular Minus K system was shown to provide between 10 and 100 times more isolation than a high-performance air table, as shown in Figure 1.5 [9]. Note the shift in resonance frequency from that of the air table to that of the Minus K isolation table. This shift represents the ability of the Minus K table to provide isolation at lower frequencies than the air table. Any value of transmissibility below 0 dB, as listed in the right-hand vertical axis of Figure 1.5, means that the mass experiences vibrations of less amplitude than that of the input vibrations. Thus, the Minus K table provides isolation for frequencies greater than roughly 0.7 Hz, whereas the high performance air table provides isolation for frequencies greater than roughly 4 Hz. Furthermore, within the isolation frequency ranges of the devices, the Minus K table isolates the mass to a greater extent than does the air table.

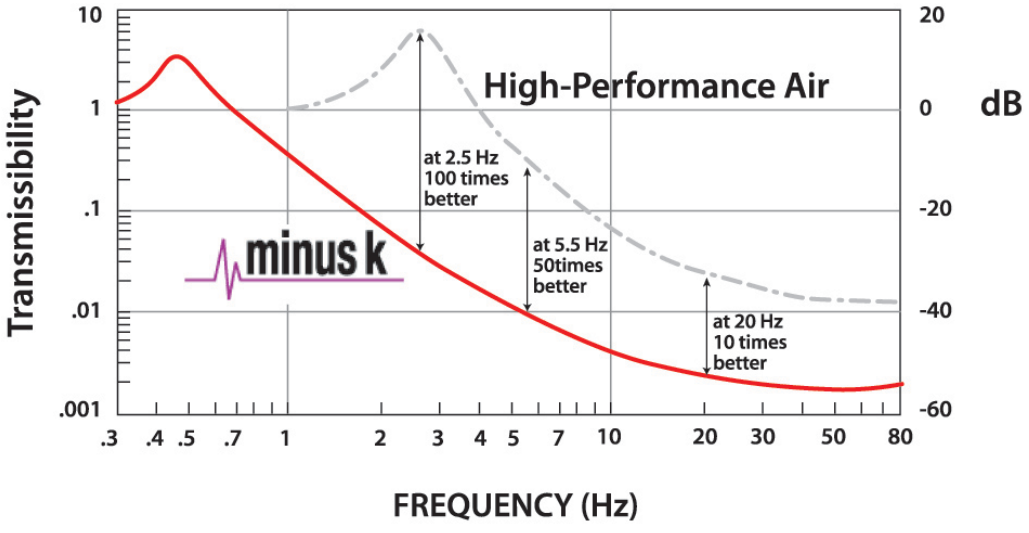

Figure 1.5. *Minus K versus high-performance air [9]*

Kashdan [7] further demonstrated this phenomenon through a system manufactured by Selective Laser Sintering. This system, displayed in Figure 1.6, directly embodies the concept shown in Figure 1.4, where the combination of a linear spring and an axially compressed beam are used to isolate a mass from a base vibration load. Kashdan performed transmissibility testing on this system, demonstrating a trend of decreasing resonance frequency with increased axial compression on the beam. The system developed by Kashdan is expanded upon in this thesis.

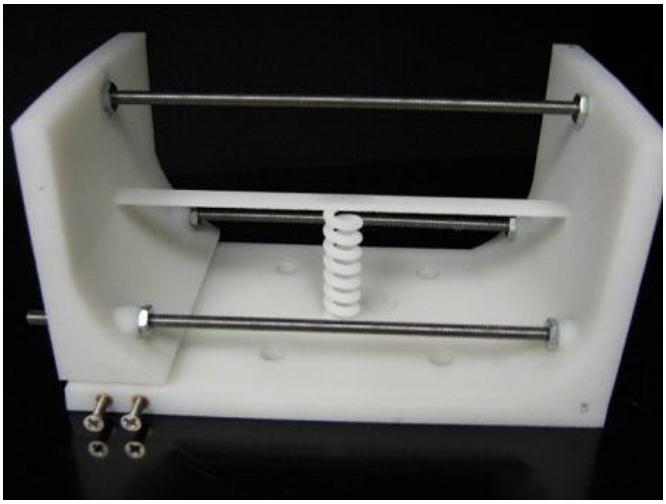

Figure 1.6. *Vibration isolation system studied in [7]*

Other NSMs have been studied for vibration isolation as well. Mizuno [10] proposed an isolation system containing a magnetic element as the NSM. Mizuno, Toumiya, and Takasaki also realized a system in which a linear actuator served as the NSM [11]. It is interesting to note that NSMs have been studied for use in a number of applications aside from isolation. Cottone has studied the use of NSMs for energy harvesting [12]. Lakes [13] has demonstrated the ability of embedded NSMs to provide extreme levels of material damping. While NSMs have been extensively studied for vibration isolation, to the author's knowledge the use of negative stiffness for shock

isolation has not been studied in depth. In addition to vibration isolation, NSMs are studied for shock isolation in the current research. However, whereas in the vibration isolation concept the NSM is constrained to operate about its meta-stable region, in the shock isolation concept the NSM is designed to operate throughout its full nonlinear regime. The nonlinear snap-through behavior exhibited by bistable mechanisms is used to provide an initially stiff and subsequently soft constitutive relationship, which is beneficial for shock isolation.

1.3 GOALS

The two primary goals of this research are to study the use of NSMs for vibration isolation and shock isolation.

In order to study the use of NSMs for vibration isolation, numerical simulations and experimental measurements of vibration isolation systems were performed and the results juxtaposed. As a part of this task, a bond graph model was created to predict the dynamic response of the systems. The constitutive relationship of each sub-component of the systems is derived or determined for use in the bond graph model. Furthermore, prototypes of the systems were fabricated through the use of Selective Laser Sintering (SLS) and tested for transmissibility. In order to save both time and cost, the prototypes were given modular features such that the sub-components are readily interchangeable. Transmissibility curves were measured for various levels of axial compression on the beams in order to demonstrate decreasing resonance frequency with increasing axial compression. Various beam topologies were investigated in order to demonstrate that the use of multiple beams in a given system yields greater reductions of stiffness per unit of axial beam compression. The effects of beam coupling techniques on the ability of the

system to reach low levels of dynamic stiffness were studied as well. Differences between analytical predictions and experimental results are discussed.

The shock isolation concept is studied using a similar methodology. Simulations and experimental measurements were performed and the results compared. As a part of this task, bond graph models were determined for the shock isolation system, the individual sub-components characterized, and a modular prototype was fabricated using SLS. As nonlinearities in the system prevent the derivation of a closed-form analytical solution, MATLAB's Simscape toolbox was used to perform numerical simulations. The prototype was tested under base shock loading in order to demonstrate the ability of the system to provide isolation at a threshold level of acceleration. Differences between analytical predictions and experimental results are discussed.

1.4 Overview of Research and Thesis

This thesis is organized into three main sections: system modeling, system design, and experimentation and results. Each section contains two main subsections: vibration isolation and shock isolation.

1.4.1 Modeling the Systems

Because manufacturing processes are both time consuming and expensive, the systems were modeled and simulated in an effort to fully understand their behavior prior to fabrication. The vibration isolation systems were modeled through the use of bond graphing and simulated through a closed-form transmissibility solution. Transmissibility represents the ratio of output vibration to input vibration amplitudes, meaning that a system provides isolation when transmissibility is less than unity, or 0 dB. The shock isolation system was modeled through the use of bond graphing and numerically

simulated using Simscape. In simulating the system, input and output accelerations were recorded in order to demonstrate a reduction in output acceleration.

Bond graphing and Simscape modeling are closely related such that one can quickly create a Simscape model after studying a bond graph. Because Simscape is readily scriptable through the MATLAB environment, it was the software chosen to carry out the numerical simulations of each system.

1.4.2 System Design

An experimental prototype of each system was designed based off of the prototype presented in Figure 1.6. The prototypes were given sliding walls to provide axial compression on the beams, adjustable through the use of threaded rods. A clamping mechanism was included on the walls such that beams can be interchanged in a given system. Furthermore, bolt holes were provided at the base of the system to facilitate the interchanging of constraining springs. For the shock isolation system, a platform was included such that additional mass or additional systems can be bolted to the top of the system.

CAD models were created for each system, transferred to the Selective Laser Sintering (SLS) software and fabricated. SLS is an additive manufacturing technique that uses a laser to sinter powder together, layer-by-layer, until a solid part is formed. SLS was used to create prototypes in this research due to its ability to quickly fabricate a part directly from a CAD file as well as the high level of design freedom it provides. These characteristics are particularly beneficial for testing prototypes which are often altered to accommodate new ideas. As opposed to high precision machining, Selective Laser Sintering can have relatively high uncertainty in the post-manufactured dimensions.

Thus, the ability to interchange small components within the system saves both time and money.

1.4.3 Experimentation and results

Each system was tested for its dynamic response. The vibration isolation systems were tested for transmissibility, whereas the shock isolation system was tested for its acceleration response to an input shock load. A LabWorks Inc. ET-139 shaker table was used to force each system at its base. Vibration isolation systems were forced with velocity chirp signals, and the shock isolation system with low frequency velocity square waves. Strain gauges were used to track compression levels in beams for the vibration isolation systems. In addition, tensile testing was used to determine material properties and various component values. Due to the temperature sensitivity of Nylon 11 and the inability of the SLS HiQ Sinterstation to precisely control temperatures in the build chamber, material properties of the SLS sintered Nylon 11 can vary significantly from build to build. Therefore, tensile bars and springs were created and tested to determine material properties and spring constants for each build. Once the response characteristics of each system were measured, they were compared against analytical predictions in order to verify the models. The usefulness of the systems for isolation is discussed as well.

Chapter 2

Vibration Isolation: Modeling

2.1 Introduction to Vibration Isolation

Passive physical systems are comprised of energy storage and energy dissipative elements. In a mechanical system, energy can be stored as kinetic energy in masses or as potential energy in springs, and energy can be dissipated by a variety of physical mechanisms (typically viscosity and friction related) which are usually modeled as dashpots or dampers. Thus, a mechanical system is a system composed of any combination of masses, springs, and dampers.

Vibration excitation of a mechanical system can create a wide array of responses within the system. For a linear, one degree-of-freedom system, the response motion of the mass is well defined mathematically as a function of excitation frequency. At low frequencies, the load is directly transmitted from the source to the mass. At the resonance frequency of the system, the amplitude of the motion reaches a maximum. At frequencies above resonance, the amplitude of motion monotonically decreases with increasing frequency. The transmissibility curve illustrated in Figure 2.1 is a representation of the response of a linear, single degree-of-freedom base-excited system to a range of harmonic inputs. Although the systems studied for vibration isolation in this thesis contain nonlinear components, they are assumed to operate within linear ranges of displacement under sufficiently low amplitude forcing. Therefore, their transmissibility curves look very similar to the illustration in Figure 2.1. Note that transmissibility is the

ratio of output amplitude to input amplitude, and is represented in units of $\mathrm{dB}=20\log_{10}(\mathrm{output}/\mathrm{input})$ in Figure 2.1.

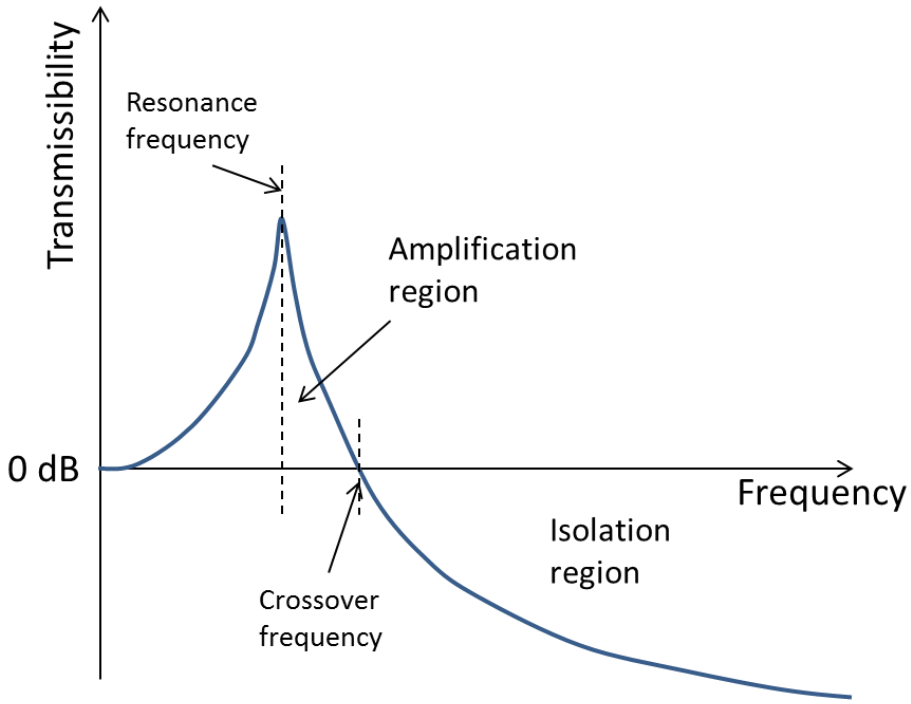

Figure 2.1. *Example transmissibility curve*

As displayed in Figure 2.1, an isolation region exists where transmissibility is less than 0dB. Within this region, the vibration experienced by the mass is of lower amplitude than that of the base. For any system designed to provide isolation from a particular frequency, operating well within the isolation region is highly desirable. In order for the system to have the capability of isolating the mass from low frequency vibrations, a low resonance frequency is necessary.

The resonance frequency of a linear, single degree-of-freedom system is defined primarily by two parameters: stiffness and mass. Decreasing spring stiffness and/or increasing mass lowers the resonance frequency, thus shifting the peak in Figure 2.1 to

the left. As the resonance frequency approaches zero, the mass can be isolated from all real values of input excitation frequency. However, given a linear spring, approaching zero frequency resonance presents the following difficulty: the spring experiences greater and greater static deflection as the stiffness decreases and/or the mass increases. Increasing the static deflection decreases the feasibility of a given system for most real-world applications due to space limitations. Thus, for purely linear isolation systems, a compromise must be made which accounts for static deflection as well as frequency isolation range. However, systems containing nonlinear negative stiffness components have been shown to contain both high static stiffness and low resonance frequency.

2.2 Discussion of Three Systems

The vibration isolation systems studied in this thesis are based on the system previously designed and tested by Kashdan [7]. A photograph of this system, previously shown in Figure 1.6, is reproduced in Figure 2.2. The system is composed of sintered Nylon 11 and consists of a linear spring in parallel with a beam. The threaded rods connecting the walls of the system are used to place axial compression on the beam. Altering the axial compression can be used to tune the local transverse stiffness of the beam, thereby altering the overall dynamic stiffness of the system to a desired level. Kashdan demonstrated a trend of decreasing resonance frequency with increasing axial compression in [7], although the predicted transmissibility curves did not agree closely with experimental measurements.

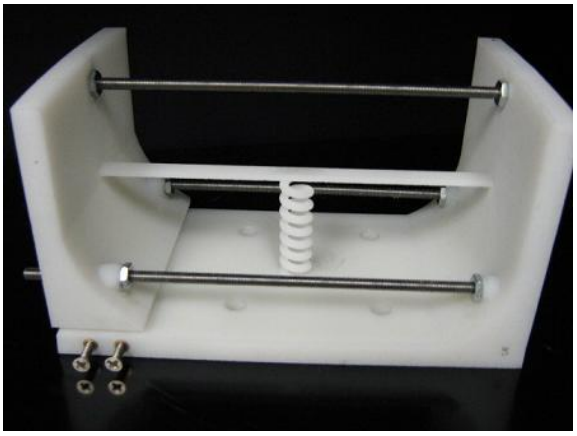

Figure 2.2. *Vibration isolation system from [7]*

In addition to the system illustrated in Figure 2.2, two closely-related systems were studied and are characterized in the following paragraphs. The first of these systems consists of two horizontally spaced beams in parallel with a linear spring. The second of these systems consists of two vertically spaced beams in parallel with a linear spring. In both systems, the dimensions of each beam are designed to be equivalent to the dimensions of the beam in Figure 2.2. The objectives of studying these designs were three-fold: to determine whether the interaction of multiple beams in various layouts improves the ability of the system to reach low levels of dynamic stiffness, to demonstrate a broader range of resonant peak reduction with a given level of axial beam compression, and to further validate analytical models against experimental data. CAD images of the two double-beam systems are shown in Figure 2.3.

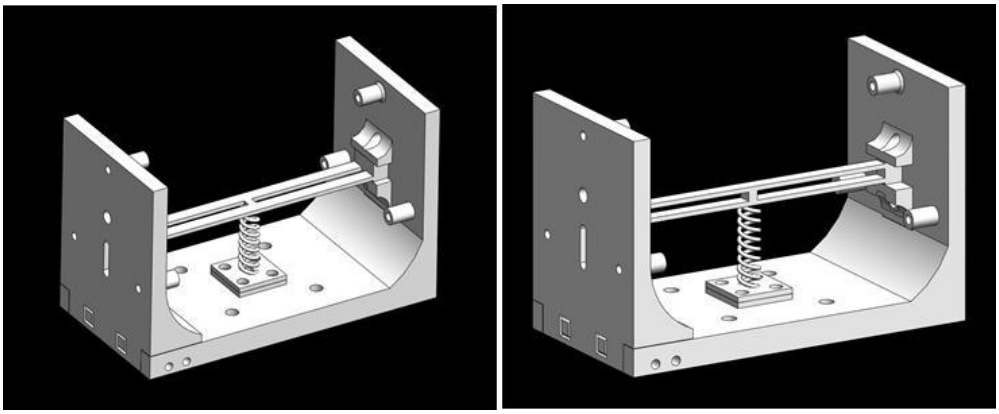

Figure 2.3. *CAD images of uncoupled double-beam system (left) and coupled double-beam system (right)*

2.3 Derivation of Analytical Model: A Bond Graph Approach

2.3.1 Introduction to Bond Graphing

Bond graphing is a physical system modeling technique invented by Henry Paynter in 1959 [14]. Bond graphs track power transfer throughout a system in a general sense, and thus, one can use bond graphing to model systems consisting of multiple energy domains. Bond graphing breaks a system down into a graph of connected energy storing and dissipating elements, power conversion elements (transformers and gyrators), and sources, conceptually similar to an electric circuit model. Power flow between elements is represented through the bonds that connect these components. 1-junctions and 0-junctions represent power distribution junctions within the system. Specifically, 1-junctions represent junctions of common flow, and 0-junctions represent junctions of common effort. 1-junctions and 0-junctions are also referred to as effort-differencing (common flow) and flow-differencing (common effort) junctions, respectively. Once the bond graph is created, one can systematically derive the state equations governing the behavior of the system. An example of a mechanical system and its bond graph can be seen in Figure 2.4.

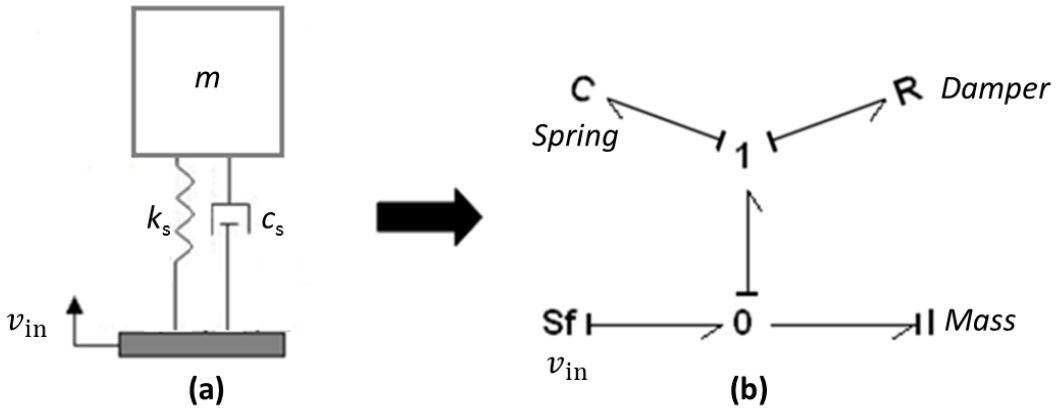

Figure 2.4. *(a) Base-excited mechanical system and (b) the equivalent bond graph model.*

In a bond graph, capital letters 'C', 'R', and 'I' represent the energy storing and dissipating elements. 'C' represents capacitance, and a 'C' element is one that stores potential energy, such as a spring. 'R' represents resistance, and an 'R' element is one that dissipates energy, such as a damper. 'I' represents inertia, and an 'I' element is one that stores kinetic energy, such as a mass. 'I' and 'C' elements, if independent, represent independent states in the system, which, generally speaking, are momentum and position. 'I' elements represent momentum states, whereas 'C' elements represent position states.

The short lines attached at the end and running perpendicular to each bond are called causality strokes. Causality strokes reveal whether a 'C' or 'I' element is independent or dependent, and thus the number of independent states in the system. If the stroke falls next to an element, the element is said to impose flow on the system. If the stroke falls on the opposite side of the bond from the element, the element is said to impose effort on the system. 'C' and 'I' elements and effort and flow sources all have a "preferred" causality. 'C' elements and effort sources prefer to impose effort on the system, whereas 'I' elements and flow sources prefer to impose flow on the system. When 'C' and 'I' elements are assigned their preferred causality, they are shown to be

independent elements. Otherwise, they are shown to be dependent. 'R' elements do not have a preferred causality as they do not represent system states. Assigning causality to a bond graph is simple and straightforward; however, the details of doing so can be found in [15] and will not be discussed in this thesis.

Each bond in the bond graph represents an effort and a flow, and therefore the flow of power (effort × flow) throughout the system. The direction of the arrow corresponds with the direction of positive (with respect to the model's coordinate system) power flow. Effort and flow are generalized constitutive variables, meaning they are the variables which constitute generalized power. By definition, power is equal to the product of effort and flow. For example, in a translational mechanical sense, power equals the product of force (effort) and velocity (flow), and in an electrical sense, power equals the product of voltage (effort) and current (flow). Discussion of generalized power yields the conclusion that the underlying behavior of components in all energy domains, including hydraulic, pneumatic, thermal, and others, is equivalent from a mathematical standpoint.

2.3.2 System Bond Graph

The vibration isolation systems from Figure 2.2 and Figure 2.3 can be modeled as a linear spring in parallel with a nonlinear spring and a damper, all connected between a base and a mass. The three systems can be represented by the same model because the extra beams in the double-beam systems simply provide additional beam stiffness. Thus, the beams in each of the double-beam systems can be lumped into a single, stiffer beam. In modeling the systems, the following assumptions were made: viscoelastic losses in the spring can be represented by an equivalent viscous, frequency dependent damper, the system is constrained to motion along only one axis; and losses in the beam are

negligible. Accounting for losses in the beam adds complicated nonlinearities into the equations of motion, thereby preventing the derivation of an analytical transfer function.

The resulting system schematics and bond graph are shown in Figure 2.5. Assuming uniaxial motion allows the conversion from the schematic in Figure 2.5(a) to that in Figure 2.5(b). To derive the bond graph in Figure 2.5(c), it can be first noted that the base and the mass share a common force. Thus, these two components are connected by a common effort 0-junction. Further, the relative velocities of the two springs and damper are equivalent since they are in mechanical parallel. This observation allows the connection of these three components with a common flow 1-junction. To connect the two resulting pieces of the bond graph, note that the difference in velocity between the base and the mass is equal to the relative velocity of the springs and damper. Then, observing that 0-junctions are flow-differencing junctions, the 0-junction can be connected to the 1-junction. Mathematically, this connection means that the input velocity minus the velocity of the springs and damper equals the mass velocity. Note in Figure 2.5 that $F_t(\delta_s)$ is used to represent the transverse constitutive relationship of the beam, where δ_s is the compression of the linear spring. Unlike the linear components, because the beam displays nonlinear behavior a constant cannot be used in the schematics to represent the beam.

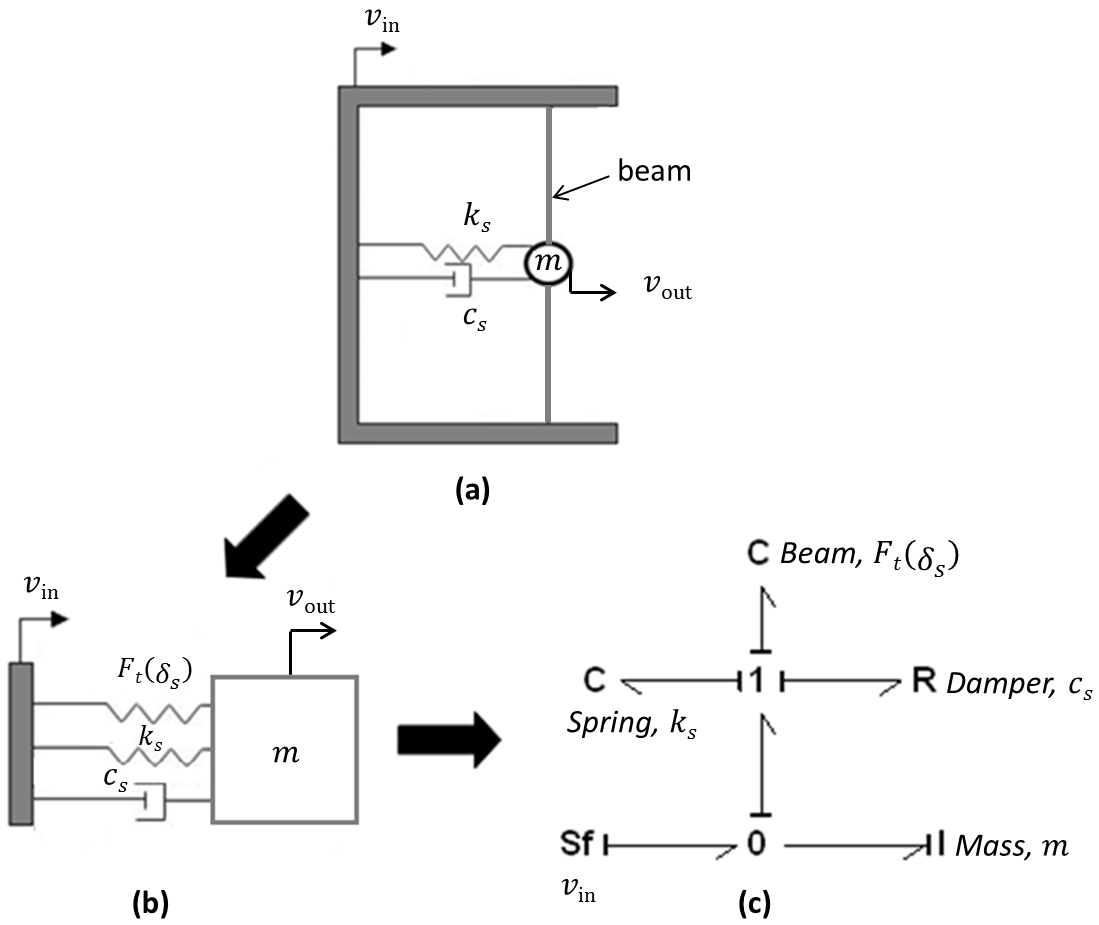

Figure 2.5. *(a) Vibration isolation system schematic, (b) reduced schematic, and (c) bond graph*

2.3.3 Constitutive Relationships

In the following paragraphs, the terms listed in Table 2.1 are used to represent various system parameters and variables.

Table 2.1. *System parameters, variables, and constants*

Notation	Description
k_N	Linearized beam stiffness (Equation 2.14)
k_s	Linear spring stiffness (Equation 2.15)
K	Linearized total system stiffness (Equation 2.33)
c_s	Equivalent viscous damper coefficient (Equation 2.17)
m	Dynamic mass of system (Equation 2.20)
δ_s	Linear spring compression
η	Material loss factor (material property from [7])
l_0	Free beam length
l_c	Compressed beam length
w	Width of beam
h	Thickness of beam
A	Cross-sectional area of beam, $A = wt$
u_y	Transverse beam displacement
u_x	Axial beam displacement
P_{cr1}	First-mode critical buckling load for beam
$u_{x,cr1}$	First-mode critical buckling displacement for beam (Equation 2.11)
F_s	Spring force
F_c	Damper force
F_t	Transverse beam force (Equations 2.9, 2.13)
d	Spring wire diameter
D	Spring mean coil diameter
L_f	Free length of spring
N_a	Number of active coils in spring (Equation 2.16)
p	Spring pitch
v_{in}	Velocity input to the base of the system
v_m	Velocity of the mass, output velocity
E	Young's Modulus (material constant)
I	Area moment of inertia of beam, $I = \frac{wh^3}{12}$
G	Shear modulus (material constant)

Prior to deriving equations of motion from the bond graph to predict the behavior of the system, the individual components within the system must first be characterized. Characterization of each component involves determining its constitutive relationship along with any corresponding coefficients. Table 2.2 lists the constitutive relationships for mechanical components.

Table 2.2. *Constitutive relationships of bond graph elements*

Element	Constitutive Law	Linear Case
'C', Spring	$F = \Phi(\delta)$	$F = k\delta$
'R', Damper	$F = \Phi(v)$	$F = cv$
'I', Mass	$v = \Phi(P)$	$v = \frac{P}{m}$

2.3.3.1 Beam

Constitutive relationships of linear elements are simple and readily available. However, the systems under study here contain a beam that is a nonlinear spring element whose constitutive relationship must be derived. In previous work, Kashdan [7] used the schematic in Figure 2.6 to model the beam.

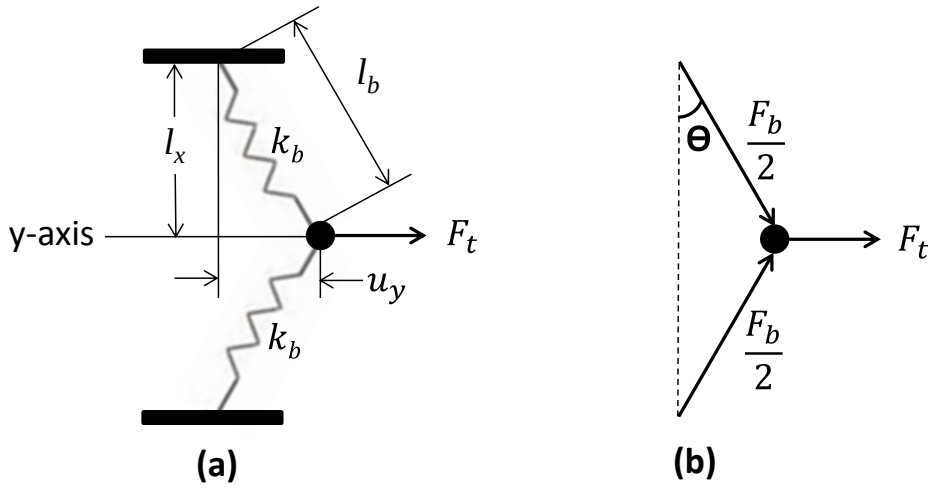

Figure 2.6. *Beam as modeled in [7]*

A more accurate relationship can be derived by considering the first-mode shape of a beam and performing energy calculations. The following derivation stems from work done by Alabuzhev et al. in [17]. Consider a beam held at a constant axial compression u_x by force P, as shown in Figure 2.7(a). Since the axial stiffness of a beam is $\frac{AE}{l_0}$, the beam contains potential energy according to:

$$U_c = \frac{1}{2}\frac{AE}{l_0}u_x^2, \tag{2.1}$$

where u_x represents the change in length of the beam due to compression. Now consider a force F_t acting transversely to hold the midpoint of the beam at a fixed vertical displacement, u_y, as in Figure 2.7(b).

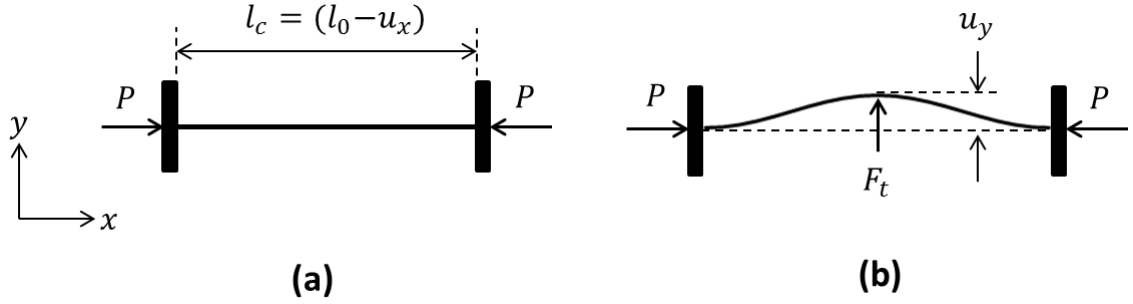

Figure 2.7. *(a) Compressed horizontal beam and (b) compressed beam experiencing transverse force*

Assume the resulting deflected beam shape is described by the first-mode shape of a buckled beam with fixed ends:

$$y(x) = \frac{u_y}{2}\left(1 - \cos\left(\frac{2\pi x}{l_c}\right)\right), \tag{2.2}$$

where u_x is the transverse displacement resulting from force F_t. The reduction in compression in the beam is equal to the arc length of the beam less the original compressed length. Using the standard formula for calculating the arc length of a curve, $L = \int_a^b \sqrt{1 + \left(\frac{d}{dx}f(x)\right)^2}\, dx$, the arc length of the beam is defined:

$$\begin{aligned} L(y(x)) &= \int_0^{l_c} \sqrt{1 + \left(\frac{d}{dx}\frac{u_y}{2}(1 - \cos\left(\frac{2\pi x}{l_c}\right)\right)^2}\, dx \\ &= \int_0^{l_c} \sqrt{1 + \left(\frac{\pi u_y}{l_c}\sin\left(\frac{2\pi x}{l_c}\right)\right)^2}\, dx. \end{aligned} \tag{2.3}$$

Using the approximation made by Vangbo in [18], the arc length becomes:

$$L(y(x)) \cong \int_0^{l_c} 1 + \frac{1}{2}\left(\frac{\pi u_y}{l_c}\sin\left(\frac{2\pi x}{l_c}\right)\right)^2 dx = \frac{u_y^2\pi^2}{4l_c} + l_c. \tag{2.4}$$

Subtracting the compressed length from this result yields the decrease in axial compression due to force F. This decrease in axial compression causes the potential energy due to compression to decrease accordingly. The decrease in potential energy is referred to as ΔU_c and is defined in Equation 2.5:

$$\Delta U_c = \frac{1}{2}\frac{AE}{l_0}\left(u_x^2 - \frac{u_y^2\pi^2}{4l_c}\right)^2. \tag{2.5}$$

The application of force F also introduces bending energy into the beam. This bending energy can be quantified as follows:

$$U_b = \frac{EI}{2}\int_0^{l_c}\left(\frac{d^2}{dx^2}y(x)\right)^2 dx = \frac{EI}{2}\int_0^{l_c}\left(2\left(\frac{\pi}{l_c}\right)^2 u_y\cos\left(\frac{2\pi x}{l_c}\right)\right)^2 dx. \tag{2.6}$$

Performing the integral in Equation 2.6 yields the following term for bending energy:

$$U_b = \frac{\pi^4 EI}{l_c^3}u_y^2. \tag{2.7}$$

The work done by force F_t over distance u_y, then, equals the total change in energy from the initial compressed state of the beam to its final bent shape. Thus,

$$\begin{aligned} F_t &= \frac{\partial U}{\partial u_y} = \frac{\partial}{\partial u_y}(\Delta U_c + U_b) \\ &= \frac{\partial}{\partial u_y}\left(\frac{1}{2}\frac{AE}{l_0}\left(u_x - \left(\frac{u_y^2\pi^2}{4l_c}\right)\right)^2 + \frac{\pi^4 EI}{l_c^3}u_y^2\right) \end{aligned} \tag{2.8}$$

$$= \frac{AE}{l_0}\left(u_x - \left(\frac{u_y^2\pi^2}{4l_c}\right)\right)\left(-\frac{1}{2}\frac{u_y\pi^2}{l_c}\right) + \frac{2\pi^4 EI}{l_c^3}u_y.$$

Collecting terms and simplifying Equation 2.8 yields the transverse constitutive relationship of the beam:

$$F_t(u_y) = 2\pi^4 EI\left[u_y\left(\frac{1}{l_c^3} - \frac{A}{4Il_0l_c\pi^2}u_x\right) + \frac{A}{16Il_0l_c^2}u_y^3\right]. \tag{2.9}$$

Now, the critical first-mode buckling load of a beam with both ends fixed is defined as follows [20]:

$$P_{\mathrm{cr1}} = \frac{4\pi^2 EI}{l_0^2}. \tag{2.10}$$

Given that the axial stiffness of a beam is $\frac{AE}{l_0}$, the critical deflection, then, is:

$$u_{x,\mathrm{cr1}} = \frac{P_{\mathrm{cr1}}}{\left(\frac{AE}{l_0}\right)} = \frac{4\pi^2 I}{Al_0}. \tag{2.11}$$

Assuming that the beams are placed under small compression levels, meaning $l_c \sim l_0$, allows us to rewrite Equation 2.9 in terms of $u_{x,\mathrm{cr1}}$:

$$F_t(u_y) = \frac{2\pi^4 EI}{l_0^3}\left[u_y\left(1 - \frac{u_x}{u_{x,\mathrm{cr1}}}\right) + \frac{A}{16I}u_y^3\right]. \tag{2.12}$$

For the vibration isolation systems, small beam deflections can be assumed. This allows us to neglect the third-order term in Equation 2.12, yielding the following result:

$$F_t(u_y) = \frac{2\pi^4 EI}{l_0^3}\left(1 - \frac{u_x}{u_{x,\mathrm{cr1}}}\right)u_y. \tag{2.13}$$

Thus, for the vibration isolation systems, the constitutive relationship of the beams is linearized according to Equation 2.13. This linearization allows us to define a new term k_N to represent the negative stiffness of the beam:

$$k_N = \frac{2\pi^4 EI}{l_0^3}\left(1 - \frac{u_x}{u_{x,\mathrm{cr1}}}\right). \tag{2.14}$$

Examining Equation 2.14, it is clear that the beam enters a region of negative stiffness when $u_x > u_{x,\mathrm{cr1}}$. Although this chapter involves a linearized model of the beam, when dealing with shock isolation in Chapter 3 the full nonlinear constitutive relationship from Equation 2.12 is utilized and expanded upon.

2.3.3.2 Spring

As displayed in Table 2.2, the constitutive relationship of a linear spring is simply Hooke's law, $F = k\delta$, where δ represents the amount of compression in the spring. From [19], the spring constant, k, can be calculated from the dimensions and material properties of the spring through:

$$k_s = \frac{d^4 G}{8D^3 N_a}. \tag{2.15}$$

In the systems under study, both ends of the spring are plain and ground, and thus

$$N_a = \frac{L_0}{p} - 1, \tag{2.16}$$

where p is the pitch of the spring, defined as the distance from the center of one coil to an adjacent coil.

2.3.3.3 Damper

The constitutive relationship of a linear viscous damper relates force and relative velocity through $F = c_s v$. For a viscoelastic spring, the equivalent viscous damper coefficient, c_s, can be calculated through the following equation [16]:

$$c_s = \frac{k_s \eta}{\omega}. \tag{2.17}$$

Note that c_s is a frequency dependent parameter. Thus, this model is more accurate for systems excited at a particular frequency or within a limited frequency range, rather than for systems experiencing a wide range of frequencies.

2.3.3.4 Mass

The constitutive relationship of a mass is $v = \frac{P}{m}$. For the systems under study, the mass of concern is the mass that is vibrating when a load is applied. During measurements performed for the present work, the primary mass is simply that of the accelerometer mounted at the output port of the system. Other masses that should be taken into account are the effective dynamic masses of the beam and spring. From [20], the dynamic mass of a vibrating beam is

$$m_{\text{beam,dyn}} = 0.384 m_{\text{beam}}, \tag{2.18}$$

and from [16], the dynamic mass of a spring is

$$m_{\text{spring,dyn}} = \frac{1}{3} m_{\text{spring}}. \tag{2.19}$$

Thus, the overall mass of the system is equal to the sum of the three masses, or

$$m = m_{\text{accelerometer}} + m_{\text{beam,dyn}} + m_{\text{spring,dyn}}. \tag{2.20}$$

2.3.4 State Equations and Transmissibility Function

The next modeling step is to derive the state equations and transmissibility function governing the systems' dynamic behavior. The state equations can be systematically derived from the bond graph in Figure 2.5(c) as shown in the next paragraph. These equations can then be used to determine a transmissibility transfer function relating the input velocity to the output mass velocity.

2.3.4.1 State Equations

State equation derivation from a bond graph begins with labeling each bond with an effort and a flow, as shown in Figure 2.8. By convention, efforts are labeled on the upper or left-hand side of each bond, whereas flows are labeled on the lower or right-hand side. In general, efforts are labeled in terms of forces and flows in terms of velocities. However, since the state variable of a mass is momentum, and the state variable of a spring is compression, efforts connected to the mass are labeled as the time derivative of momentum, $\dot{P}_m$, and flows connected to the springs are labeled as the time derivative of compression, $\dot{\delta}_s$. This labeling is important because state equations may contain only state variables and their time derivatives, and constants.

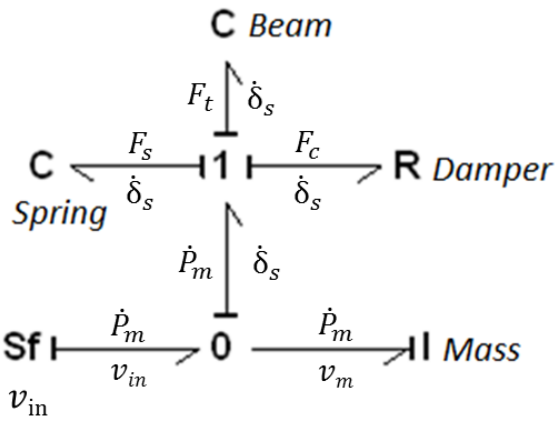

Figure 2.8. *Labeled vibration system bond graph*

Note that all forces connected to the 0-junction are given the same label, as 0-junctions are common effort junctions. Similarly, all velocities connected to a 1-junction are given the same label, as 1-junctions are common flow junctions.

Considering the 0-junction as a flow-differencing junction, the following can be written:

$$v_{\text{in}} - \dot{\delta}_s - v_m = 0. \tag{2.21}$$

Substituting the constitutive relationship for a mass from Table 2.2 into Equation 2.21 and rearranging,

$$\dot{\delta}_s = v_{\text{in}} - \frac{P_m}{m}. \tag{2.22}$$

Equation 2.22 is the first of two state equations. The second state equation can be determined by considering the 1-junction as an effort-differencing junction. From this consideration, the following can be written:

$$\dot{P}_m - F_s - F_t - F_c = 0. \tag{2.23}$$

Substituting the constitutive relationships for a linear spring and damper from Table 2.2, along with the transverse, linearized constitutive relationship of the beam from Equation 2.13 into Equation 2.23 and rearranging,

$$\dot{P}_m = k_s\delta_s + k_N\delta_s + c_s\dot{\delta}_s. \tag{2.24}$$

Inserting Equation 2.22 into this result yields the second and final state equation:

$$\dot{P}_m = k_s\delta_s + k_N\delta_s + c_s\left(v_{\text{in}} - \frac{P_m}{m}\right). \tag{2.25}$$

The two state equations are condensed into matrix form, also known as state-space form, below:

$$\begin{bmatrix}\dot{\delta}_s \\ \dot{P}_m\end{bmatrix} = \begin{bmatrix}0 & -\frac{1}{m} \\ (k_s + k_N) & -\frac{c_s}{m}\end{bmatrix}\begin{bmatrix}\delta_s \\ P_m\end{bmatrix} + \begin{bmatrix}v_{\text{in}} \\ c_s v_{\text{in}}\end{bmatrix}. \tag{2.26}$$

2.3.4.2 Transmissibility Transfer Function

The systems' time-domain behavior can be simulated by specifying an input velocity and solving the two state equations through the use of a first-order differential equation solver, such as ode45 from MATLAB. However, in vibration isolation, frequency-domain behavior contains more information regarding the usefulness of a system. As mentioned in Section 2.1, the mass is isolated from frequencies at which

transmissibility is less than 0 dB. The transmissibility transfer function can be derived from the state equations as described in the following paragraph.

Taking the time derivative of Equation 2.25 yields the following:

$$\ddot{P}_m = k_s\dot{\delta}_s + k_N\dot{\delta}_s + c_s\left(\dot{v}_{\text{in}} - \frac{\dot{P}_m}{m}\right). \tag{2.27}$$

By substituting Equation 2.22 for $\dot{\delta}_s$ into Equation 2.27, a second-order differential equation is obtained in terms of momentum:

$$\ddot{P}_m = k_s\left(v_{\text{in}} - \frac{P_m}{m}\right) + k_N\left(v_{\text{in}} - \frac{P_m}{m}\right) + c_s\left(\dot{v}_{\text{in}} - \frac{\dot{P}_m}{m}\right). \tag{2.28}$$

Rearranging, this becomes:

$$\ddot{P}_m + c_s\frac{\dot{P}_m}{m} + (k_s + k_N)\frac{P_m}{m} = c_s\dot{v}_{\text{in}} + (k_s + k_N)v_{\text{in}}. \tag{2.29}$$

Since momentum is the product of mass and velocity, Equation 2.29 can be rewritten as follows:

$$\ddot{v}_m + c_s\frac{\dot{v}_m}{m} + (k_s + k_N)\frac{v_m}{m} = c_s\frac{\dot{v}_{\text{in}}}{m} + (k_s + k_N)\frac{v_{\text{in}}}{m}. \tag{2.30}$$

Taking the Laplace transform of Equation 2.30 yields the following expression in the Laplace domain:

$$s^2v_m + s\frac{c_s}{m}v_m + \frac{(k_s + k_N)}{m}v_m = s\frac{c_s}{m}v_{\text{in}} + \frac{(k_s + k_N)}{m}v_{\text{in}}. \tag{2.31}$$

Replacing s with $j\omega$ and separating variables yields the transmissibility transfer function between v_{in} and v_m in the frequency domain:

$$T(\omega) = \frac{v_m}{v_{\text{in}}} = \frac{\left(j\omega\frac{c_s}{m} + \frac{(k_s + k_N)}{m}\right)}{\left(-\omega^2 + j\omega\frac{c_s}{m} + \frac{(k_s + k_N)}{m}\right)}. \tag{2.32}$$

In order to simplify the transfer function, a parameter K is introduced which represents the total system stiffness. K is simply the sum of the spring and beam stiffnesses as follows:

$$K = k_s + k_N. \tag{2.33}$$

The transfer function can now be written as:

$$T(\omega) = \frac{v_m}{v_{in}} = \frac{\left(j\omega\frac{c_s}{m} + \frac{K}{m}\right)}{\left(-\omega^2 + j\omega\frac{c_s}{m} + \frac{K}{m}\right)} = \frac{\left(j2\zeta\left(\frac{\omega_n}{\omega}\right) + \left(\frac{\omega_n}{\omega}\right)^2\right)}{\left(j2\zeta\left(\frac{\omega_n}{\omega}\right) + \left(\frac{\omega_n}{\omega}\right)^2 - 1\right)}, \tag{2.34}$$

where ω_n is the resonance frequency, defined as $\omega_n = \sqrt{\frac{K}{m}}$, and ζ is the damping ratio, defined by $\zeta = \frac{c_s}{2m\omega_n}$. This transfer function is used to simulate the responses of the three vibration isolation systems to harmonic base excitation.

2.4 Simulations and Discussion

The dimensions and material properties used to execute the vibration simulations are listed in Table 2.3. Refer to Table 2.1 for notation. When calculating spring stiffness from the values in Table 2.3, the stiffness value must be multiplied by two as a double-helix spring is used in the vibration isolation designs.

Table 2.3. *Dimensions and properties in vibration simulations*

l_0	0.155 m	p	0.01 m
h	0.0025 m	E	1225e6 Pa (from [7])
w	0.008 m	G	477e6 Pa (from [7])
D	0.01 m	eta	0.03 (from [7])
d	0.00213 m	ρ	975 kg/m^3
L_f	0.043 m		

2.4.1 Note on System Buckling Limit

The critical first-mode buckling displacement for a beam, previously listed in Equation 2.11, occurs at the compression level in which the transverse stiffness equals zero. However, in the systems under study, the spring acts to prevent the beam from buckling into the first mode at the expected compression level. The first-mode critical buckling limit of the system can be found by determining the compression level at which the total system stiffness equals zero. Setting Equation 2.33 to zero,

$$k_\mathrm{s} + k_\mathrm{N} = 0 = k_s + \frac{2\pi^4 EI}{l_0^3}\left(1 - \frac{u_{x,\mathrm{cr1}}^{\mathrm{sys}}}{u_{x,\mathrm{cr1}}}\right). \tag{2.35}$$

Thus, the first-mode buckling limit of the system is defined below:

$$u_{x,\mathrm{cr1}}^{\mathrm{sys}} = \left(\frac{k_\mathrm{s} l_0^3}{2\pi^4 EI} + 1\right) u_{x,\mathrm{cr1}}. \tag{2.36}$$

The relationship in Equation 2.36 is important because it represents the maximum theoretical amount of compression the beams can receive before the systems become bistable, or in the case of the linearized models, unstable. From a practical standpoint, the system is never fully unstable, as it tends to reach equilibrium at one of the bistable

states. In order to ensure stability in the linearized model, however, the following simulations are made for compression levels below $u_{x,\mathrm{cr1}}^{\mathrm{sys}}$.

2.4.2 Single-Beam System

The plots in Figure 2.9 represent the expected dynamic behavior of the single-beam system loaded under various amounts of pre-compression. Each peak represents the resonance of the system at a particular compression level. As displayed in Figure 2.9, increasing the amount of axial compression in the beam decreases both the resonance frequency of the system and the magnitude of the transmissibility at resonance. Theoretically, the resonance frequency approaches zero as u_x approaches $u_{x,\mathrm{cr1}}^{\mathrm{sys}}$. In reality, practical limitations prevent the system from reaching zero frequency resonance. However, a system whose overall dynamic stiffness is lower than the positive stiffness of the supporting spring represents an improvement over the traditional mass-spring-damper vibration isolation system. The benefits of having both a stiff static spring to support a mass and a compliant dynamic spring to provide vibration isolation are present in such a system.

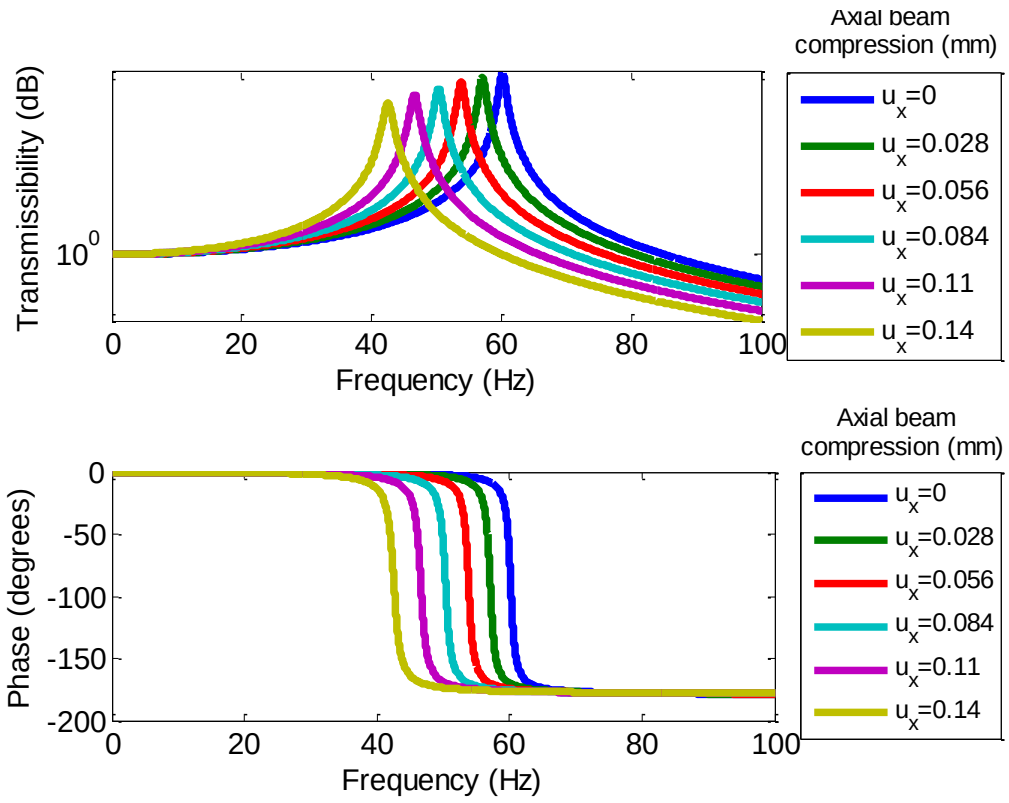

Figure 2.9. *Simulated transmissibility (upper plot) and phase (lower plot) of single-beam system*

2.4.3 Double-Beam Systems

Because the two double-beam systems have the same dynamic model, their dynamic simulations are identical. As previously mentioned, the goals of investigating the two double-beam cases include determining whether either orientation enhances the ability to achieve low levels of dynamic stiffness, as well as demonstrating a larger reduction in resonance frequency for a given level of compression than in the single-beam design. Investigating these systems also provides further opportunity to validate the theoretical models derived in Section 2.3 against experimental data.

The plots in Figure 2.10 represent the predicted dynamic behavior of the double-beam systems. As in the single-beam system, the resonance frequency decreases with increasing axial compression on the beam. Compared with the single-beam system, the decrease in resonance of the double-beam systems from zero to 0.14 mm compression is much more drastic. Because the stiffness of the beams drops much more rapidly with compression than in the single-beam design, the double-beam designs can achieve a greater level of negative stiffness to counteract a more positively stiff spring. In any case, if the systems do not reach their first-mode buckling limit prior to the beams reaching a higher-mode buckling limit, the beams will buckle into a higher mode. Once the beams buckle into a higher mode, the transverse negative stiffness of the beams stays constant with respect to increasing axial compression [20]. Since the double-beam stiffnesses decrease more rapidly with compression than the single-beam stiffness, the double-beam systems have the ability to counteract a more positively stiff spring prior to buckling into a higher mode. Therefore, if a stiffer spring is used in parallel with the double-beams, the system can support a larger mass while still maintaining low dynamic stiffness. The coupling link in the coupled double-beam design is meant to delay second-mode buckling to a higher compression level by restricting rotation at the midpoint of the beams. Delaying second-mode buckling would allow the beams to reach a greater level of negative stiffness prior to buckling into a higher mode.

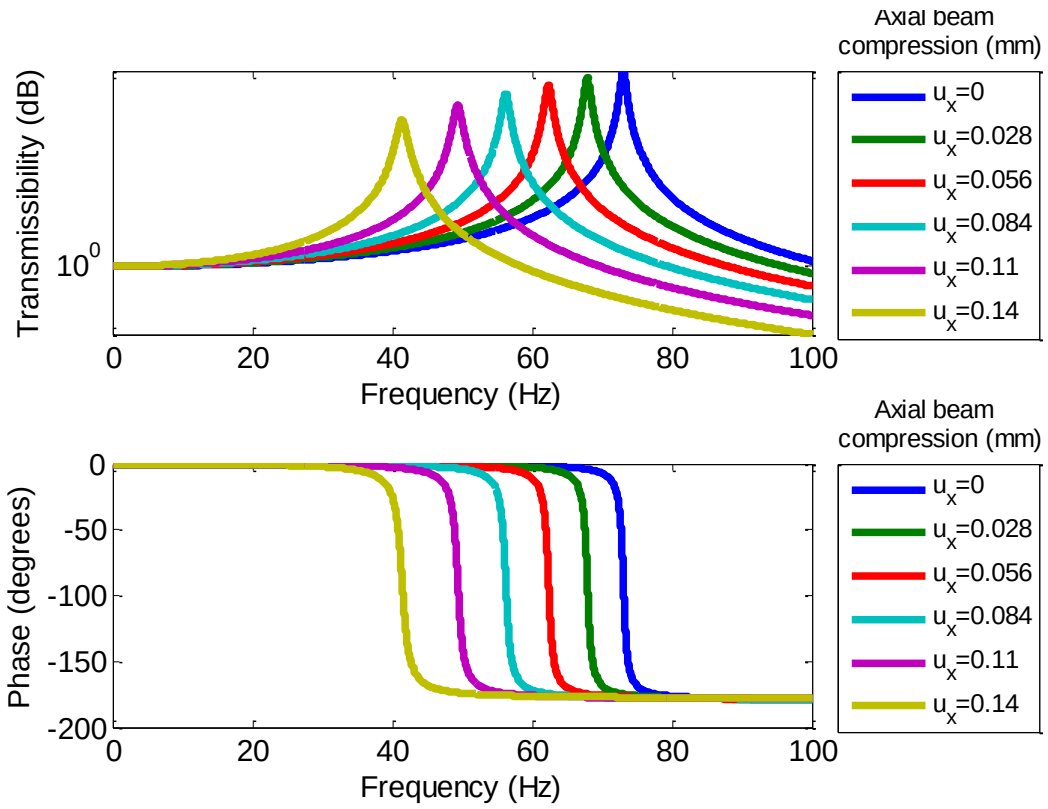

Figure 2.10. *Simulated transmissibility (upper plot) and phase (lower plot) of double-beam system*

2.5 SUMMARY

In this chapter, an analytical model based on bond graphing was developed to describe a vibration isolation system in three configurations. Individual components of the system were characterized, state equations were generated from the bond graph, and a transfer function was derived from the state equations. While the derivation yields a similar result as that derived in [7], two primary improvements have been made. The beam, modeled as two pinned springs in [7], was modeled more accurately in this chapter as a fixed-fixed beam in its first-mode shape. Furthermore, whereas the transfer function in [7] represents a system whose beam and spring are in series, the transfer function in

this chapter represents the beams and springs in parallel. This derivation provides a more accurate model of the tests discussed in Chapter 5.

MATLAB was used to create plots of the transfer functions for the single-beam and double-beam cases. The models predict the resonant frequencies of the systems to decrease with increasing axial compression on the beam. In the double-beam systems, the resonance frequency decreases at a higher rate with respect to increasing beam compression. This represents a system that can support a larger mass than in the single-beam system while still achieving desirable vibration isolation performance.

Chapter 3

Shock Isolation: Modeling

3.1 Introduction to Shock Isolation

Shock excitations cause a system to experience high levels of acceleration over a short period of time. In most cases, high levels of acceleration are a detriment to the performance of a system for a variety of reasons. Humans and equipment can be harmed if various thresholds of acceleration are exceeded. In the case of a boat travelling at high speeds across a wavy ocean surface, the slamming of the boat against each wave can cause harm to a human on board. Thus, the need for a mechanical isolation system to mitigate the shock transmitted from the boat to the human is evident.

Two conflicting goals often form the basis of shock isolator design: low acceleration transmission and low isolator deflection. In the case of a mechanical system undergoing an acceleration shock at its foundation, the desire to reduce the acceleration transmitted to the payload mass exists in order to prevent harm to the payload. Geometric limitations typically create the need to minimize the amount deflection in the isolating device as well. These goals are inherently conflicting because, for example, the use of a stiff spring will keep the deflection of an isolator low but will result in a high amount of acceleration transmitted from the base to the mass.

These two goals lead to the discussion of shock isolation in terms of work and energy. The force experienced by the mass is equal to the force transmitted through the isolating mechanism, and it is related to the acceleration of the mass through Newton's

second law, $F = ma$. Work is the integral of a force with respect to the displacement over which it acts, which, in the case of a constant force, is the product of the isolator force and the isolator deflection. Most shock loads can be represented in terms of a parameter known as an instantaneous velocity shock, or V [1]. For an acceleration shock load, V is simply equal to the integral of the acceleration with respect to time. V is related to the amount of kinetic energy imparted into the isolator by the shock through:

$$E_k = \frac{1}{2}mV^2 \tag{3.1}$$

A shock isolator absorbs the kinetic energy and can store it as potential energy and/or dissipate it through thermal energy. For a lossless system, the work done on the isolating mechanism can be written in terms of potential energy through:

$$W = E_p = \int_0^{\delta} F d\delta \tag{3.2}$$

where δ is the deflection and F is the force experienced by the isolator. The concept of stored energy is readily understood through force versus displacement plots, as shown in Figure 3.1.

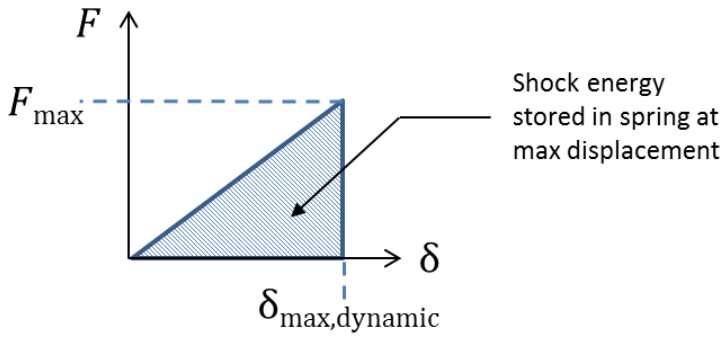

Figure 3.1. *Linear shock isolator potential energy storage*

As shown in Figure 3.1, the system continues to deflect until all kinetic energy imparted by the shock is stored as potential energy, after which oscillatory motion ensues.

With this knowledge in mind, the concept of an ideal shock isolator can be formed. An ideal shock isolator is one that imparts no more than a desired threshold level of acceleration to the mass while keeping the deflection required to do so to a minimum [3]. Thus, harmful acceleration levels can be avoided and space requirements are minimized. The ideal shock isolator is represented in Figure 3.2 through a force versus displacement curve. This case is considered to be ideal because the maximum deflection experienced by the isolator, $\delta_{\text{max,dynamic}}$, represents the minimum deflection required to isolate a mass from given shock load while transmitting no more than an acceleration of $\frac{F_{\text{max}}}{m}$ to the mass.

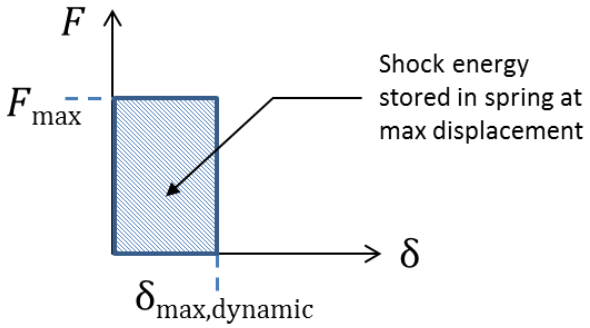

Figure 3.2. *Ideal shock isolator potential energy storage*

Due to the shape of the curve in Figure 3.2, an ideal shock isolator can also be known as a constant force isolator. Whether or not it is explicitly stated, the goal of most systems designed for shock isolation is to approach the ideal case represented in Figure 3.2. In fact, the force versus displacement plot of a standard mass-spring-damper (MSD) system optimized for a given shock load mimics the ideal case. However, due to rate

dependencies of the damper, a standard MSD system optimized for a given shock load is not optimal for a most other shock loads.

A typical linear MSD system was simulated in order to demonstrate its ability to approach the ideal case as well as to highlight potential drawbacks of the system. Table 3.1 summarizes the parameters used for this demonstration.

Table 3.1. *Parameters of linear mass-spring-damper simulation*

m	1.5 kg
k	1682.86 N/m
c	41.8 Ns/m
A_s	10 g's
T_s	0.01 s

In Table 3.1, A_s represents the amplitude and T_s represents the time duration of the shock load. The shape of the shock load for this particular case is versine. The versine acceleration profile is illustrated in Figure 3.3 and can be calculated according to the following formula:

$$a_{\text{in}}(t) = \frac{A_s}{2}\left(1 - \cos\left(\frac{2\pi t}{T_s}\right)\right). \tag{3.3}$$

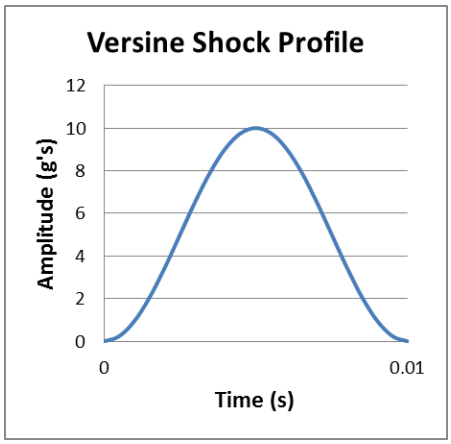

Figure 3.3. *Versine shock profile*

Values k and c were determined using fminsearch, a Nelder-Mead based optimization algorithm from MATLAB. The goals of the optimization were to keep acceleration below 1.45 g's while minimizing isolator compression.

The images in Figure 3.4 show a typical MSD system along with its force versus displacement plot for a particular input acceleration shock load. The damper causes the initial steep slope in Figure 3.4(b) because its force is directly proportional to its relative velocity. Since a shock load is a rapid acceleration, the damper initially reacts to high velocity. The force in Figure 3.4(b) reaches a plateau at around 21.5 N. Thus, the isolated mass experiences no more than roughly 21.5 N of force, or ~1.45 g's of acceleration. Because much of the energy is dissipated by the damper, the isolator requires significantly less deflection for a given level of g's transmitted than in the lossless case presented in Figure 3.1. Thus, adding a rate-dependent damper to the linear, lossless case and optimizing yields a design which more closely mimics ideal. However, the linear MSD system does not demonstrate this ideal behavior when the input shock amplitude is varied, as is discussed in the next paragraph.

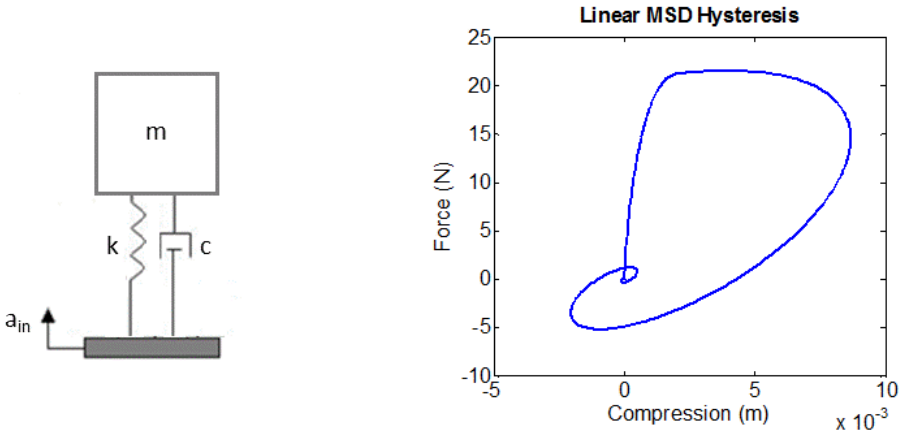

Figure 3.4. *(a) Mass-spring-damper system and (b) force versus displacement response to a shock*

To demonstrate the need for an improved system to provide ideal shock isolation under various loading conditions, the linear MSD system discussed in the previous paragraph was simulated under shock inputs of various amplitudes. Figure 3.5 shows the response of the system to shock loads of increasing input amplitudes.

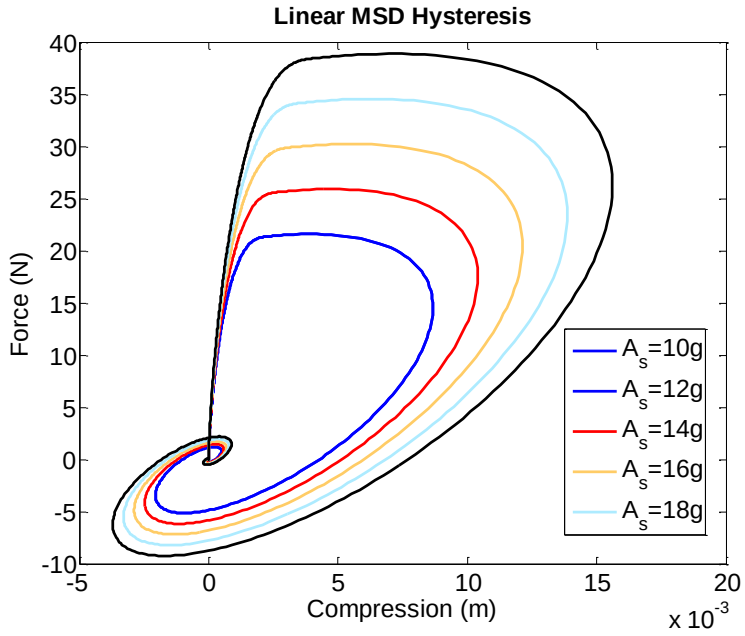

Figure 3.5. *Force versus displacement response of linear MSD system to various shock input amplitudes*

Although the optimized linear MSD maintains the near ideal characteristics of high initial stiffness and constant force isolation for each case in Figure 3.5, the maximum force transmitted to the mass increases as the input amplitude increases. Therefore, as the input shock amplitude increases, the acceleration felt by the mass exceeds the specified acceleration limit of 1.45 g. The system studied for shock isolation in the current research resolves this issue by relying on capacitive elements to provide the ideal shock isolation characteristics rather than on a dissipative element. Because capacitive elements are insensitive to velocity, nonlinear behavior within capacitive

elements can be exploited to provide near ideal shock isolation for a variety of input shocks.

An additional benefit of harnessing nonlinear capacitive elements for shock isolation is the ability to provide high initial static stiffness. Because the linear MSD system relies on a dissipative element to increase the initial stiffness of the system when under shock loading, the system is not as stiff under static loading when no relative velocity is present to excite the damper. The use of a nonlinear capacitive element to provide the initial stiffness allows a system to maintain high levels of stiffness for both static and dynamic loading. High initial static stiffness in a shock isolator could provide many potential benefits for dynamic isolation in general. For example, if the shock isolation system is placed in series with a vibration isolation system, the shock isolation system can directly transmit low frequency vibrations. Thus, the vibration isolation system could solely be active for vibration input loading, and if hard stops are present in the vibration isolation system, the shock isolation system could be solely active for shock input loading.

3.2 DISCUSSION OF SYSTEM

The system investigated in this research approaches ideal shock isolation through the use of a nonlinear negative stiffness element. Similar to the vibration isolation system, the shock isolation system consists of a beam in parallel with linear springs. However, unlike the vibration isolation system in which the beam is held at its meta-stable state by a constraining spring, the beam in the shock isolation system begins at one of its stable first-mode buckled states (refer back to Figure 1.3). Figure 3.6 shows schematics of the shock isolation system along with the bond graph model of the system. Note that $F_{\mathrm{t}}(\delta_{\mathrm{s}})$ and $F_{\mathrm{OWD}}(\delta_{\mathrm{s}})$ are used to represent the constitutive relationships of the

beam and of a nonlinear one-way damper, respectively. Because these components are nonlinear, constants cannot be used to represent their behavior in the schematics.

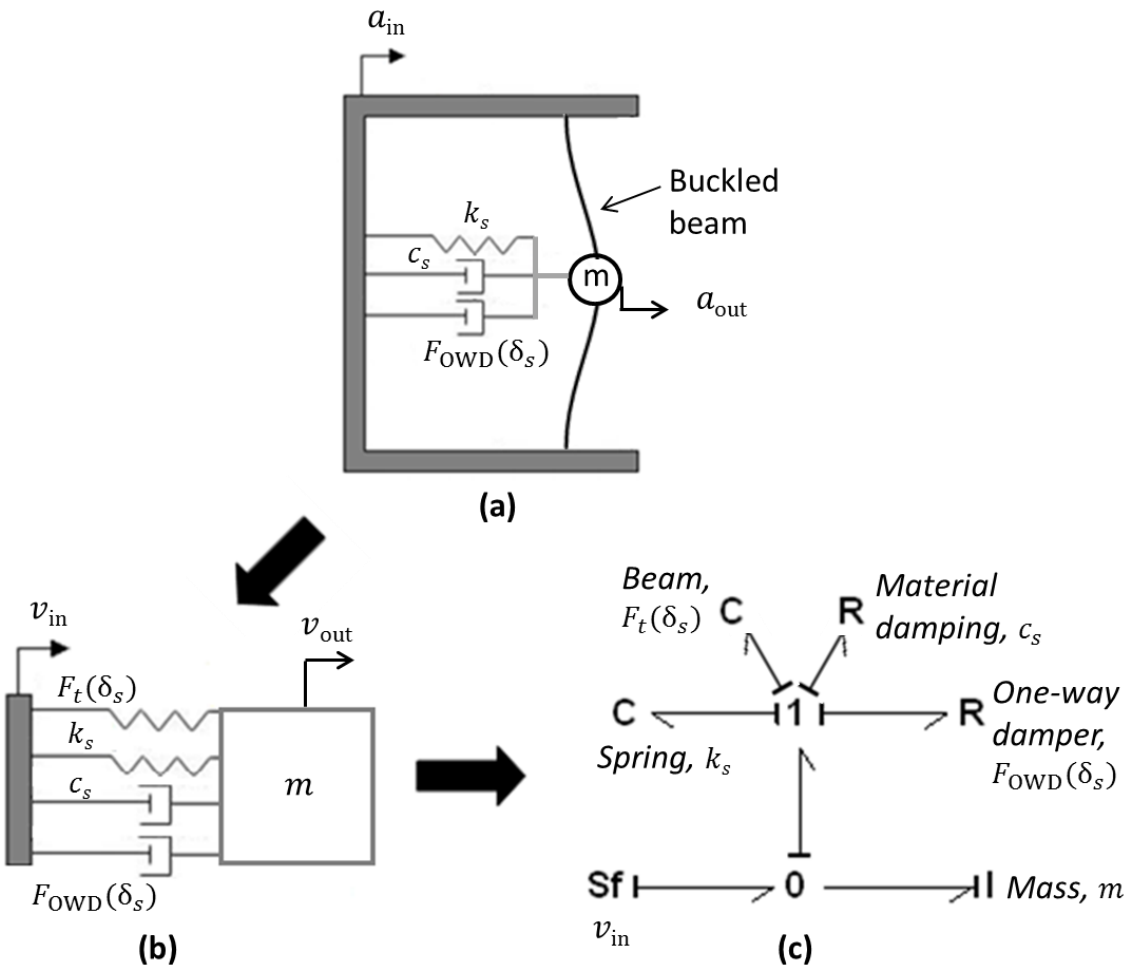

Figure 3.6. *Shock isolation schematics and bond graph*

Once the beam is buckled to a desired level, linear springs, whose stiffnesses sum to equal the absolute value of the negative stiffness of the beam at its meta-stable state, are added at free length in parallel with the beam. Thus, when the system is initially compressed the stiffness is very high, equating to the sum of the linear spring stiffness and the linearized stiffness of the beam at the first-mode buckled state. However, as the

beam is further compressed into its negative stiffness region, the stiffnesses of the beam and springs sum to zero yielding a total system stiffness of zero. This behavior essentially mimics a switch that causes the shock isolation system to engage at a particular force threshold. A one-way damper is added in parallel with the spring and beam as well, which gives zero dissipation for compressive velocities and high dissipation for tensile velocities. This addition enables the system to maintain its near-ideal force switching capability during compressive loading but still dissipate energy as the system returns to steady-state. The schematics in Figure 3.6 illustrate the shock isolation concept.

3.3 Derivation of Analytical Model

Due to the similarities in the vibration and shock isolation systems, the dynamic bond graph model of the shock isolation system in Figure 3.6(c) is nearly identical in form to the vibration isolation model presented in Figure 2.8(c). Furthermore, the constitutive equations of the linear components are equivalent. However, significant changes are made in the equation used to represent F_t, the transverse force in the beam. Additional nonlinear damping is added in the form of a one-way damper as well. These changes are discussed in the following paragraphs.

In addition to the notation described in Table 2.1, the terms in Table 3.2 are used to represent various parameters and variables for the shock isolation system.

Table 3.2 *Additional parameters*

Notation	Description
u_{y0+}	Positive first-mode location (Equation 3.6)
P_{cr3}	Third-mode critical buckling load for beam (Equation 3.9)
$u_{x,cr3}$	Third-mode critical buckling displacement for beam (Equation 3.10)
$k_{N,3}$	Third-mode negative stiffness constant (Equation 3.11)
F_{thresh}	System force threshold (Equation 3.15)
$\sigma_{b,max}$	Maximum bending stress in beam (Equation 3.23)
σ_a	Axial stress in beam (Equation 3.24)
$\sigma_{t,max}$	Maximum tensile stress in beam (Equation 3.25)
Δ_{max}	Dimensionless compression limit for beam (Equation 3.27)
$k_{b,init}$	Initial beam stiffness (Equation 3.28)
$k_{sys,init}$	Initial system stiffness (Equation 3.31)
c_{OWD}	Damping coefficient of one-way damper
A_s	Shock pulse amplitude
T_s	Shock pulse time duration

3.3.1 Third-Mode Buckled Beam

3.3.1.1 Zero-Shift

In the vibration isolation model of the beam, oscillations are assumed to be small and to occur at the meta-stable location. This allows for a simplified linear constitutive model of the beam. In the shock isolation design, the full nonlinear behavior of the beam is essential to the design and must be taken into account. Thus, Equation 2.12, which describes the nonlinear behavior of a first-mode buckled beam about its meta-stable location, is used as starting point to develop the new relationship. Equation 2.12 is reproduced below:

$$F_{\mathrm{t}}(u_y) = \frac{2\pi^4 EI}{l_0^3}\left[u_y\left(1 - \frac{u_x}{u_{x,\mathrm{cr1}}}\right) + \frac{A}{16I}u_y^3\right] \tag{3.4}$$

In the shock isolation design, the starting point of the beam is at one of its bistable states rather than at its meta-stable state as in the vibration isolation designs. The first change made to Equation 3.4 is therefore a shift in u_y to a stable state. To determine the locations of the first-mode stable states, Equation 3.4 is set equal to zero and solved for u_y. Factoring a u_y term out of the bracketed portion,

$$\frac{2\pi^4 EI}{l_0^3}u_{\mathrm{y}}\left[\left(1 - \frac{u_x}{u_{x,\mathrm{cr1}}}\right) + \frac{A}{16I}u_y^2\right] = 0. \tag{3.5}$$

Solving for u_y from this result yields:

$$u_{y0} = 0, \pm\sqrt{\frac{16I\left(\frac{u_x}{u_{x,\mathrm{cr1}}} - 1\right)}{A}}. \tag{3.6}$$

Equation 3.6 can be simplified by dividing the I term by A, to give:

$$u_{y0} = 0, \pm 2\sqrt{\frac{1}{3}h^2\left(\frac{u_x}{u_{x,\mathrm{cr1}}} - 1\right)}, \tag{3.7}$$

where the first solution, $u_{y0} = 0$, represents the meta-stable location of the beam and the nonzero solutions represent the bistable locations of the beam. In further discussions, the positive nonzero solution is referred to as u_{y0+}. Shifting the midpoint of the beam to the u_{y0+} stable location and once again assuming $l_{\mathrm{c}} \sim l_0$ results in the following modified constitutive relationship:

$$F_{\mathrm{t}}(u_y) = \frac{2\pi^4 EI}{l_0^3}\left[(u_y - u_{y0+})\left(1 - \frac{u_x}{u_{x,\mathrm{cr1}}}\right) + \frac{A}{16I}(u_y - u_{y0+})^3\right], \tag{3.8}$$

where $u_y = u_{y0+}$ now represents the meta-stable location of the beam and $u_y = 0, 2u_{y0+}$ represent the bistable locations.

3.3.1.2 Third-Mode Effects

In the shock isolation design, the beam is constrained to pass between bistable first-mode states through its third-mode shape, as depicted in Figure 3.7. In general, if a beam is compressed past its third-mode buckling limit, it will still pass between stable states through the second mode when a transverse displacement is applied. However, if rotation is constrained at the midpoint of the beam, the beam will pass between first-mode states through its third-mode shape. The third-mode shape can be calculated from formulas presented in [18].

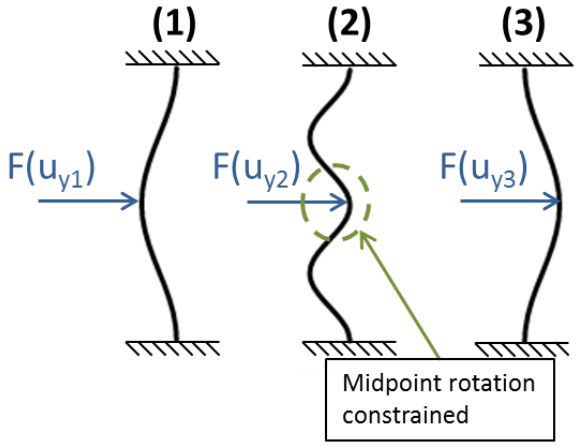

Figure 3.7. *Third-mode buckled beam*

In further discussions, the buckling of a beam into any mode other than its first mode is referred to as "higher-mode buckling." Higher-mode buckling is a primary factor

in the success of the shock isolation concept presented in this research. When a beam is buckled into the first mode it is relatively stiff in the transverse direction. However, once the beam buckles into a higher mode its stiffness instantly becomes a constant, negative value. The transverse force versus displacement curve of a higher-mode buckled beam, then, is a piecewise combination of a third-order polynomial with a negatively sloped line, as shown in Figure 3.8. This piecewise behavior provides the capability of the beam to act as a force switch that activates at a particular force threshold. It also allows for a wide array of possible constitutive curves for a given beam. Without higher-mode buckling, a beam would not be able to display the piecewise switching capability shown in Figure 3.8. Rather, the constitutive equation of the beam would be represented only by the standard third-order polynomial presented in Equation 3.8.

States (1), (2), and (3) shown in Figure 3.8 correspond with those displayed in Figure 3.7. FEA modeling has shown that the nonlinear portion of the curve closely matches the behavior predicted by Equation 3.8. It has also revealed that, for a given buckling mode, the linear portion of the curve has a negative slope that can be found by solving for the meta-stable stiffness of the beam. Between the intersections of the nonlinear and linear curves, the linear curve dominates.

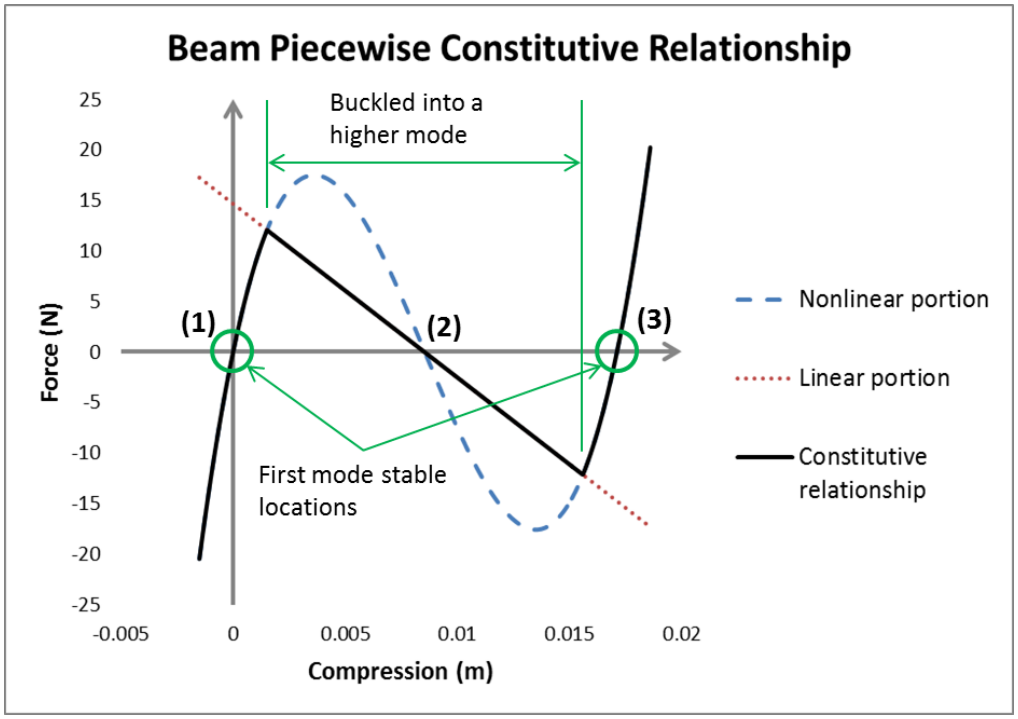

Figure 3.8. *Full piecewise constitutive relationship of a higher-mode buckled beam*

Since the beam is constrained to buckle into the third mode in this research, the slope in the linear portion of the constitutive relationship can be found by solving for the meta-stable stiffness of the beam at its third-mode buckling limit. The third-mode critical buckling load of a beam with both ends fixed is [20]:

$$P_{\text{cr3}} = \frac{4(2\pi)^2 EI}{l_0^2} \tag{3.9}$$

The third-mode critical buckling displacement of a beam with both ends fixed can be found by dividing this result by the axial stiffness of the beam as follows:

$$u_{x,\text{cr3}} = \frac{P_{\text{cr3}}}{\left(\frac{AE}{l_0}\right)} = \frac{4(2\pi)^2 I}{A l_0} \tag{3.10}$$

Plugging this limit into Equation 2.14, which expresses the linearized stiffness of a beam at its meta-stable location, yields the following third-mode buckled negative stiffness:

$$k_{\mathrm{N},3} = \frac{2\pi^4 EI}{l_0^3}\left(1 - \frac{u_{x,\mathrm{cr3}}}{u_{x,\mathrm{cr1}}}\right) \tag{3.11}$$

The overall transverse constitutive relationship of the third-mode buckled beam can be formulated by combining the linear and nonlinear portions of curve as follows:

$$F_{t,3}(u_y) = \begin{cases} \min\left(\begin{matrix} k_{N,3}(u_y - u_{y0+}), \\ \frac{2\pi^4 EI}{l_0^3}\left[(u_y - u_{y0+})\left(1 - \frac{u_x}{u_{x,\mathrm{cr1}}}\right) + \frac{A}{16I}(u_y - u_{y0+})^3\right] \end{matrix}\right), u_y \le u_{y0+} \\ \max\left(\begin{matrix} k_{N,3}(u_y - u_{y0+}), \\ \frac{2\pi^4 EI}{l_0^3}\left[(u_y - u_{y0+})\left(1 - \frac{u_x}{u_{x,\mathrm{cr1}}}\right) + \frac{A}{16I}(u_y - u_{y0+})^3\right] \end{matrix}\right), u_y > u_{y0+} \end{cases}, \tag{3.12}$$

where $u_y = u_{y0+}$ represents the metastable position of the beam. At values of u_y less than or equal to this position, the minimum of the linear and nonlinear equations is used. Otherwise, the maximum of the two equations is used. Equation 3.12 describes the fully nonlinear, third-mode buckled behavior of a beam, and it is the constitutive relationship used to represent the beam in the shock isolation system.

To fully display the force switching capability of the proposed system, the force versus displacement curve of a third-mode buckled beam in parallel with a linear spring is illustrated in Figure 3.9. If the positive stiffness of the linear spring and the absolute value of the negative stiffness of the third-mode buckled beam are equal, the force plateaus at a constant threshold value. Otherwise, the force slopes either upward or downward while the beam is buckled in the third mode.

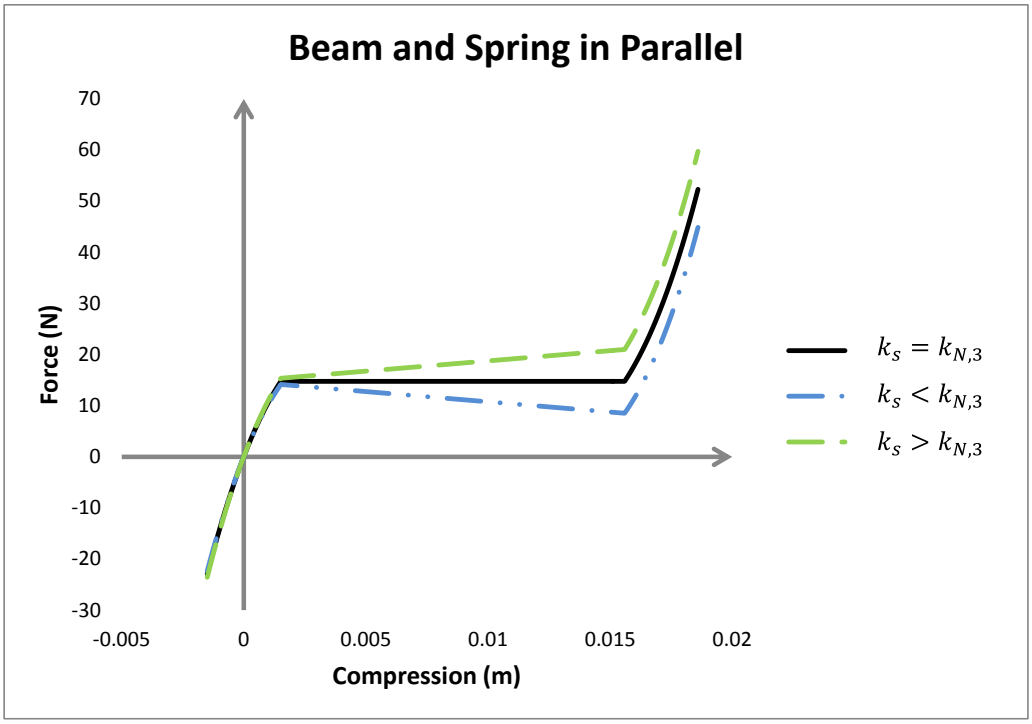

Figure 3.9. *Force versus displacement of a third-mode buckled beam and spring in parallel*

3.3.2 One-Way Damper

Adding an appropriate amount of typical linear, viscous damping to the shock isolation system would aid the system in returning to steady state quickly and at reasonable velocity and acceleration levels. However, doing so would also distort the near ideal force versus displacement curve provided by the beam and spring in parallel. Therefore, the desire exists to keep damping to a minimum while the system is undergoing compression. However, in order to dissipate the energy of a shock load, damping should be present while the system is returning to steady state. From these two considerations, the concept of a one-way damper is formed. A one-way damper is a damper that provides dissipation for tensile velocities and zero dissipation for

compressive velocities, or vice versa. Therefore, the constitutive relationship of a one-way damper can be formulated as follows:

$$F_{\mathrm{OWD}}(v) = \begin{cases} c_{\mathrm{OWD}} v, & v \geq 0 \\ 0, & v < 0 \end{cases}. \tag{3.13}$$

From a practical standpoint, true one-way damping is impossible to achieve. However, achieving relatively low damping levels for compressive velocities and high damping levels for tensile velocities is highly desirable for this design. Section 3.4 shows system simulations comparing the effects of one-way damping versus typical damping and zero damping.

3.3.3 Relevant Design Parameters

The following parameters are of particular importance for the shock isolation design: force threshold level, negative stiffness constant (from Equation 3.11), compression limit, and initial stiffness.

The force threshold is reached when the beam buckles into its third-mode. At this point, the positive stiffness of the springs negate the negative stiffness of the beam, resulting in near-zero stiffness. Because the force remains constant throughout the linear region of the constitutive relationship of the beam, one can solve for the force threshold level simply by summing the linear portion of the beam's curve with the linear constitutive relationship of a spring.

$$F_{\mathrm{thresh}} = k_{N,3}\left(\delta_s - u_{y0+}\right) + k_s \delta_s. \tag{3.14}$$

Equating k_s to $\left|k_{N,3}\right|$, collecting terms and simplifying,

$$F_{\mathrm{thresh}} = -k_{N,3} u_{y0+}. \tag{3.15}$$

The compression limit can be defined such that the beam does not plastically deform while buckled into the third mode. The standard formula for bending stress is $\sigma_b = \frac{My}{I}$, where M represents bending moment and y represents distance to the central bending axis. For the third-mode buckled beam, maximum values for M and y occur at $x = 0$ and $y = \frac{h}{2}$, respectively, where x is the central axis of the beam and y is the height of the beam from its central axis. The standard formula for bending moment is $M = I\frac{d^2y}{dx^2}$, where y represents the mode shape of the beam. Therefore, the maximum bending stress in the beam can be determined as follows:

$$\sigma_{b,\max} = \frac{E\left(\frac{d^2y}{dx^2}\Big|_{x=0}\right)h}{2}. \tag{3.16}$$

From [18], the mode shape of a third-mode buckled beam is

$$y = A_3\left[1 - \cos\left(\frac{4\pi x}{l_c}\right)\right]. \tag{3.17}$$

To determine the third-mode amplitude, A_3, the arc length of the beam after buckling is assumed to be roughly equal to the compressed length of the beam at its third-mode buckling limit. Using the approximation made by Vangbo [18] for arc length,

$$l_0 - u_{x,\mathrm{cr3}} = \int_0^{l_c}\left[1 + \frac{(dy/dx)^2}{2}\right]dx. \tag{3.18}$$

Taking the derivative of Equation 3.17 with respect to x, this result can be rewritten as follows:

$$l_0 - u_{x,\mathrm{cr3}} = \int_0^{l_c}\left[1 + \frac{1}{2}\left(\frac{4\pi A_3}{l_c}\sin\left(\frac{4\pi x}{l_c}\right)\right)^2\right]. \tag{3.19}$$

Integrating this result,

$$l_0 - u_{x,\mathrm{cr3}} = l_c + \frac{4}{l_c}(A_3\pi)^2. \tag{3.20}$$

Recalling the relationship for compressed length, $l_c = l_0 - u_x$, A_3 can be solved for in terms of u_x:

$$A_3 = \frac{1}{2\pi}\sqrt{(u_x - u_{x,\mathrm{cr3}})l_c}. \tag{3.21}$$

Taking the second derivative of Equation 3.17 with respect to x and inserting A_3 from Equation 3.21 yields the following:

$$\frac{d^2y}{dx^2} = \frac{8\pi}{l_c^2}\sqrt{(u_x - u_{x,\mathrm{cr3}})l_c}\cos\left(\frac{4\pi x}{l_c}\right). \tag{3.22}$$

Substituting Equation 3.22 into Equation 3.16 and assuming $l_c \sim l_0$ yields the maximum bending stress for a third-mode buckled beam in terms of u_x, the axial compression on the beam:

$$\sigma_{b,\max}(u_x) = \frac{4E\pi h}{l_0^2}\sqrt{(u_x - u_{x,\mathrm{cr3}})l_0}. \tag{3.23}$$

The axial stress in the beam should also be taken into account. Since compressive forces in the third-mode buckled beam equal P_{cr3}, the compressive stress can be found by using the standard formula for axial stress,

$$\sigma_a = \frac{F}{A} = \frac{P_{\mathrm{cr3}}}{A}. \tag{3.24}$$

The maximum tensile stress in the beam, then, can be found by subtracting the compressive axial stress from the maximum bending stress, or

$$\sigma_{t,\max} = \sigma_{b,\max} - \sigma_a. \tag{3.25}$$

In order to translate the maximum tensile stress into a compression limit, it is set equal to the yield stress of the material, S_y. Then, solving for u_x in terms of S_y, the following limit for compression is obtained:

$$u_{x,\max} = \left(\frac{\left(S_y + \frac{P_{\text{cr3}}}{A} \right)}{4E\pi h} \right)^2 l_0 + u_{x,\text{cr3}}. \tag{3.26}$$

In order to represent the compression limit in non-dimensional terms, a parameter Δ is introduced which equals the compression divided by the free length of the beam. The compression limit in terms of Δ can thus be written as follows:

$$\Delta_{\max} = \left[\left(\frac{\left(S_y + \frac{P_{\text{cr3}}}{A} \right) l_0}{4E\pi h} \right)^2 l_0 + u_{x,\text{cr3}} \right] l_0. \tag{3.27}$$

The compression should be kept to less than $\Delta_{\max}$ in order to avoid plastic deformation of the beam.

The initial stiffness of the system can be found by summing the stiffness of the linear springs with the linearized stiffness of the beam when $u_y = 0$. Taking the derivative of the nonlinear portion of Equation 3.12 and setting u_y to zero yields the initial stiffness of the beam,

$$k_{b,\text{init}} = \frac{2\pi^4 EI}{l_0^3} \left[\left(1 - \frac{u_x}{u_{x,\text{cr1}}} \right) + \frac{3A}{16I} \left(-u_{y0+} \right)^2 \right]. \tag{3.28}$$

Substituting in the definition of u_{y0+} from Equation 3.6 simplifies this result to:

$$k_{b,\text{init}} = \frac{4\pi^4 EI}{l_0^3}\left(\frac{u_x}{u_{x,\text{cr1}}} - 1\right), \tag{3.29}$$

where $k_{b,\text{init}}$ is the initial stiffness of the beam. Adding the total stiffness of the springs to $k_{b,\text{init}}$ gives the initial stiffness for the system:

$$k_{\text{sys,init}} = \frac{4\pi^4 EI}{l_0^3}\left(\frac{u_x}{u_{x,\text{cr1}}} - 1\right) + k_s. \tag{3.30}$$

When k_s is chosen to equal the absolute value of the negative stiffness in the beam, as in this design, $k_{\text{sys,init}}$ becomes the following:

$$k_{\text{sys,init}} = \frac{2\pi^4 EI}{l_0^3}\left(\frac{2u_x + u_{x,\text{cr3}}}{u_{x,\text{cr1}}} - 3\right). \tag{3.31}$$

The initial stiffness of the system is important because the higher the stiffness, the closer the system is to replicating the ideal shock isolation curve.

3.3.4 Viscoelastic Damping

Recall from Section 2.3.3.3 that the viscoelastic damping in the springs is frequency dependent. In the shock isolation system, the inputs are transient pulses which do not excite the system at any particular frequency. For a linear system, the frequency value used to determine the dashpot coefficient could be accurately chosen as the resonance frequency of the system. However, as nonlinear systems do not have a constant stiffness, a resonance frequency cannot be determined. Therefore, for purposes of modeling the viscoelastic loss in the spring, the frequency value used to determine the

dashpot coefficient is the natural frequency corresponding to the linearized initial system stiffness, or

$$\omega_n = \sqrt{\frac{k_{\text{sys,init}}}{m}}. \tag{3.32}$$

Then, from Equation 2.17,

$$c_s = \frac{k_s \eta}{\sqrt{\frac{k_{\text{sys,init}}}{m}}}. \tag{3.33}$$

3.3.5 State Equations

Because the dynamic bond graph models of the shock and vibration isolation systems are nearly identical, the state equations are nearly identical as well. In fact, the first state equation, Equation 2.22, remains unchanged. The differences in the second state equation, Equation 2.25, lie in the nonlinear components present in the shock isolation system. Since the beam is now represented by a nonlinear constitutive relationship, the $k_N \delta_s$ terms are replaced by $F_{t,3}$ defined in Equation 3.12. Furthermore, the effect of one-way damping can be directly added to the second state equation since it acts in parallel with the spring and beam. Thus, Equation 2.25 can be rewritten as follows:

$$\dot{P}_m = k_s \delta_s + F_{t,3}\{\delta_s\} + F_{\text{OWD}}\left\{v_{\text{in}} - \frac{P_m}{m}\right\} + c_s\left(v_{\text{in}} - \frac{P_m}{m}\right). \tag{3.34}$$

In Equation 3.34, $f\{u\}$ notation is used to denote "f as a function of u." The nonlinearities present in the system prevent the state equations from being reformulated into state-space form as in Equation 2.26.

3.4 Simulations and Discussion

3.4.1 Simscape Model

Due to the nonlinearities in the shock isolation system, no closed-form solution to the state equations is available. Therefore, in order to predict the response of the system to a shock input, numerical integration routines must be applied. Simscape, a MATLAB based simulation software, was used to numerically solve the state equations. Simscape utilizes a graphical user interface (GUI) which allows the user to connect various mechanical elements to build a system schematic. Each mechanical element is mathematically represented by a constitutive relationship. The connections between blocks represent the mathematical connectivity between the elements. While Simscape does not explicitly generate state equations, the connections between elements along with the constitutive relationships of the elements implicitly define the state equations. Figure 3.10 shows the Simscape model used to simulate the shock isolation system. The physical system is encapsulated by a dashed-line box.

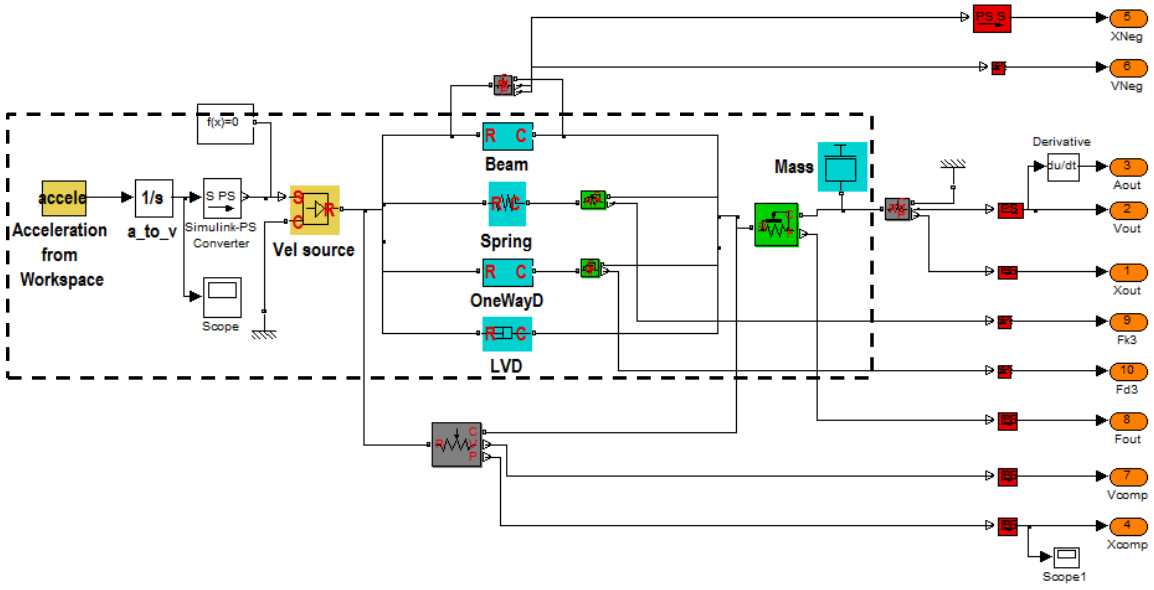

Figure 3.10. *Simscape model of shock isolation system*

The primary objects to notice in Figure 3.10 are those with bold-font descriptions. The physical energy storing elements are highlighted in blue, and the inputs to the system are highlighted in yellow. Apart from these objects, the rest of the Simscape model represents signal manipulation to convert and store data. The arrangement of the inputs and physical elements matches that of the physical schematic present in Figure 3.10. The vertical alignment and connectivity of the beam, spring, one-way damper (OneWayD), and linear viscous damper (LVD) makes it easy to observe that these elements are mechanically in parallel. Furthermore, since these components are positioned in between the input velocity and the mass, one can accurately deduce that they represent the isolating mechanism.

3.4.2 Shock Response

The geometrical parameters, material properties, and shock input parameters in Table 3.3 are used in simulating the shock isolation system. The design parameters described in Section 3.3.3 are calculated and listed as well. The shape of the shock load is versine. In the simulations, the shock isolation system is considered to operate vertically. Absolute motion of the base and mass is considered positive in the upward direction. Relative motion between the base and mass is considered positive when the system is undergoing compression. The beam is initially at rest in the upward first-mode buckled shape, and the springs are initially at free length.

Table 3.3. *Shock isolation simulation parameters*

l_0	0.2 m	S_y	30e6 Pa
h	0.00243 m	E	1614e6 Pa
w	0.0122 m	F_{thresh}	21.363 N
δ	0.01	k_N	-1.7201e3 N/m
k_s	1.7201e3 N/m	Δ_{max}	0.02
c_s	0.542 Ns/m	$k_{sys,init}$	2.4185e4 N/m
c_{OWD}	200 Ns/m	A_s	10 g
m	1.5 kg	T_s	0.01

3.4.2.1 Without One-Way Damping

As demonstrated in Figure 3.11 and Figure 3.12, without a one-way damper the system exhibits ring-down behavior for an extended period of time. The positive accelerations are kept less than or equal to a threshold value of ~1.4 g's, but when the system returns back to its initial state it is met with high levels of acceleration in the opposite direction. These high levels of negative acceleration are due to the very stiff nature of the beam at its starting location. Figure 3.11 displays the first few oscillations of the system after experiencing a shock load. The system follows the force versus compression curve in Figure 3.12 with very little hysteresis per oscillation. The force levels out at a threshold value of ~21 N, as calculated and documented in Table 3.3.

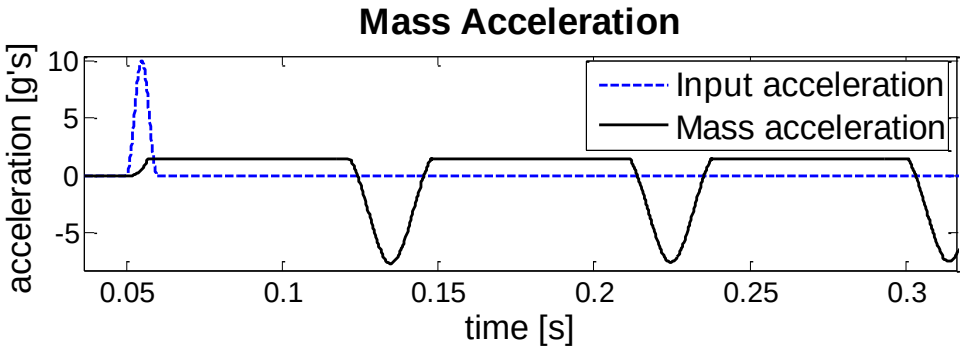

Figure 3.11. *Acceleration versus time shock response, without one-way damper*

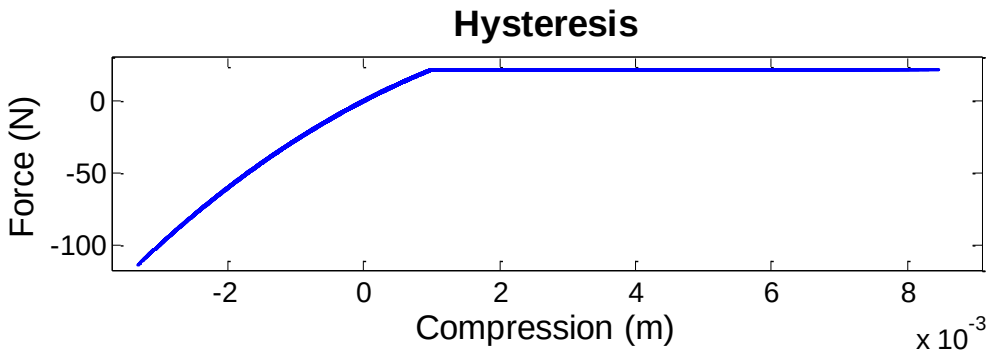

Figure 3.12. *Hysteretic shock response, without one-way damper*

3.4.2.2 With One-Way Damping

With one-way damping, the system is able to dissipate energy while decompressing after the shock load. This dissipation allows the system to return to its starting point at a much lower relative velocity than in the previous case. Thus, when the system decompresses back into its initial shape, it requires much lower levels of deceleration to return to zero relative velocity. Figure 3.13 displays the acceleration response of the mass to the input shock load. The positive acceleration levels out at ~1.4g's while the negative acceleration reaches a maximum magnitude of less than 1g.

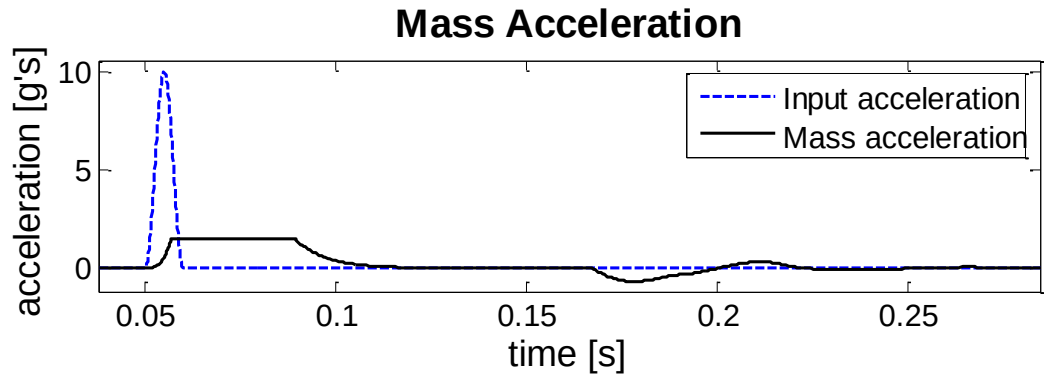

Figure 3.13. *Acceleration versus time shock response, with one-way damper*

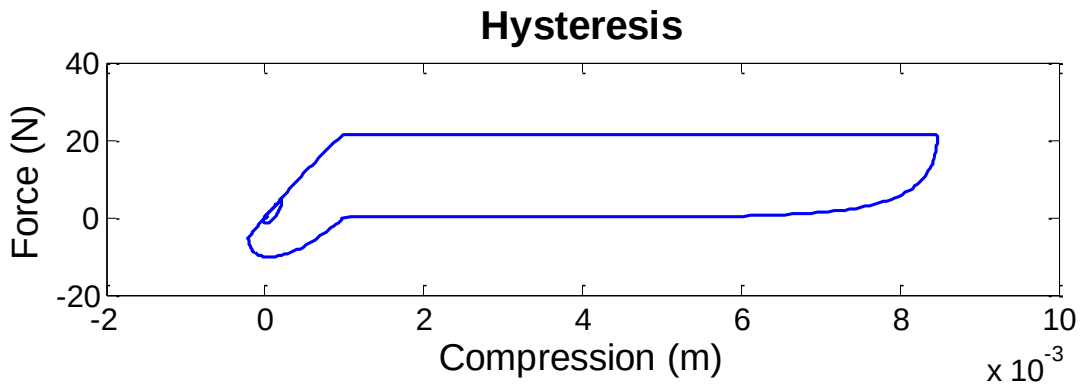

Figure 3.14. *Hysteretic shock response, with one-way damper*

The system follows the force versus displacement curve in Figure 3.14 with large amounts of hysteresis per oscillation. The sum of the areas within the loops on the hysteresis plot represents the total amount of energy dissipated. The one-way damper allows the shock isolation system to follow a near-ideal force switching path during compression, while also allowing the system to decompress at a reasonably low relative velocity. Thus, both positive and negative accelerations, and compression levels, can be kept low.

An additional benefit of utilizing a one-way damper is that the system can maintain its near-ideal characteristics for alternate shock loads. Figure 3.15 displays

hysteretic curves of the system excited by various shock input amplitudes. For the cases in which A_s is less than or equal to 16 g, the system maintains its near-ideal performance. It is important to note, however, that if the system reaches its lower first-mode buckled shape, the system stiffness increases dramatically along with the transmitted force and acceleration. This behavior can be referred to as bottoming out. The case in which A_s equals 18 g displays this stiffening effect.

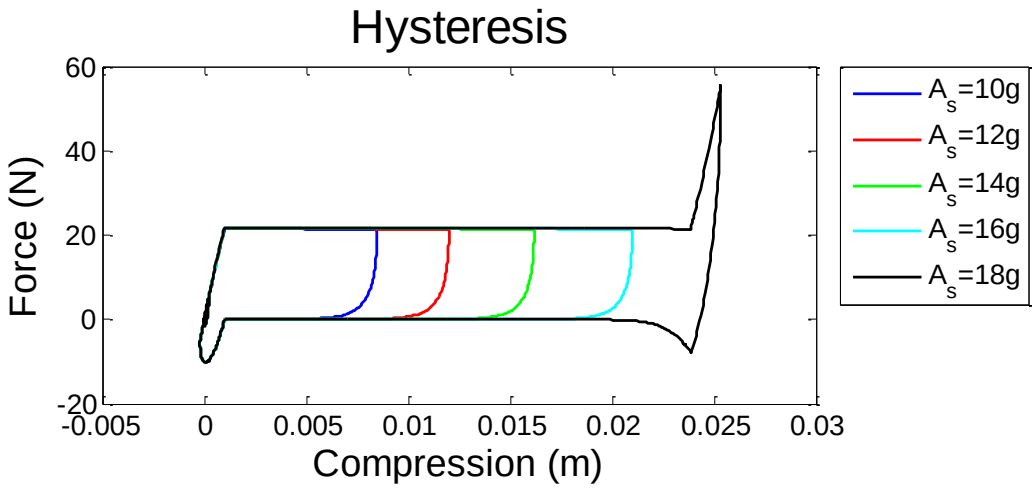

Figure 3.15. *Hysteresis plots for various shock input amplitudes*

3.5 SUMMARY

In this chapter, an analytical model of a shock isolation system utilizing a third-mode buckled beam was derived. The behavior of a beam exhibiting higher-mode buckling was characterized. In general, a higher-mode buckled beam displays a nonlinear piecewise constitutive relationship when transversely displaced at its midpoint. This piecewise behavior allows the beam to mimic a switch that activates at a particular force. The concept of a one-way damper was defined and discussed as well. One-way damping is a key to the success of the design as it allows for the benefits of near-ideal compressive behavior along with return to steady state at reasonable velocity and acceleration levels.

The nonlinearities in the system prevent the derivation of a closed-form solution to the state equations, resulting in the need for numerical integration to predict the dynamic behavior. Simscape, a MATLAB-based modeling package, was used to numerically simulate the response of the system to a shock input. Simulations of the system with and without a one-way damper were made, revealing the importance of the one-way damper in returning the system to steady state. The versatility of the system was displayed through its ability to isolate the mass from a variety of shock input amplitudes and still maintain near-ideal behavior. However, shocking the system beyond its negative stiffness region into its lower first-mode shape leads to high levels of transmitted acceleration due to stiffening.

Chapter 4

System Design and Fabrication

4.1 VIBRATION ISOLATION SYSTEMS

4.1.1 CAD Modeling

The basic form of the vibration isolation systems follows that presented in [7]. As shown in Figure 4.2 and Figure 4.3, the beams are constrained axially between two side walls, one of which is free to move along an axis parallel to the length of the beam and one of which is fixed. A double-helix spring connects the midpoint of the beams with the bottom plate of the structure. The walls are rigidly connected to the bottom plate through the use of set screws. Thus, the walls and bottom plate together form the base of the system from which the mass should be isolated. Axial compression can be placed on the beam through the use of three 10-32 threaded rods which run parallel to the beam.

Modular features, labeled in Figure 4.1, were added to the system to allow for the interchange of components. The spring and beam are fully detachable from each other and from the base of the system. Clamps on the side walls allow for the beams to be clamped rather than sintered directly in to the wall as in [7]. The base of the spring is sintered to a plate which can be bolted onto the base of the system using four ¼”-20 machine screws. The beams and spring can be attached to each other through the use of a small machine screw. The moving wall is fully detachable from the bottom plate and

slides along two guide rails which keep the face of the moving wall parallel to the face of the fixed wall.

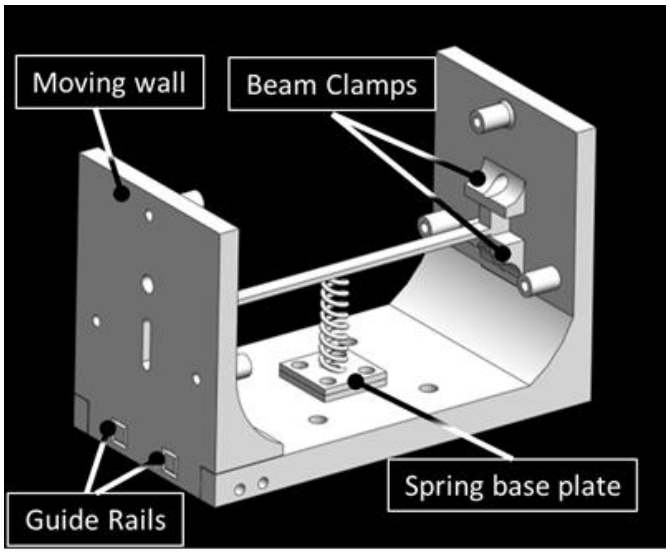

Figure 4.1. *Modular vibration isolation design features*

CAD images of the single-beam and double-beam designs are displayed in Figure 4.2. As the name implies, the single-beam system contains just one beam. The double-beam systems differ from each other with respect to the coupling between the beams. In the uncoupled double-beam system, the beams are horizontally spaced with a connecting link at the midpoint of the beams. This link is designed to be small such that rotation at the midpoint of the beams can still occur, allowing for second-mode buckling. In the coupled double-beam design, the beams are stacked vertically with a relatively large connecting link at the midpoint of the beams. This link is designed such that rotation at the midpoint of the beams is restricted, raising the second-mode buckling limit of the beams and encouraging third-mode buckling.

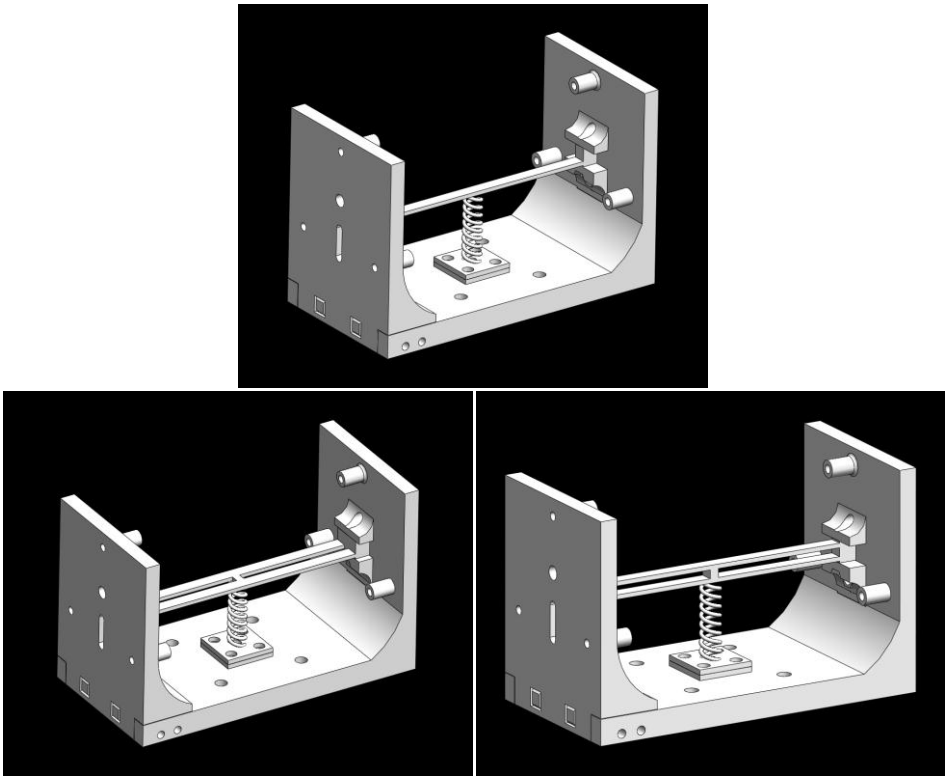

Figure 4.2. *CAD images of the vibration isolation systems: single-beam system (upper), coupled double-beam system (lower-left) and uncoupled double-beam system (lower-right)*

4.1.2 Fabricated Dimensions

Each design was fabricated using SLS. The particular combination of machine, material, and build parameters used in fabricating parts for this project tends to result in over-sintering of the parts. Thus, the fabricated dimensions of each part are typically larger than the designed dimensions. In order to verify the analytical model derived in Chapter 2 against experimental data, the fabricated dimensions should be used as the analytical inputs rather than the designed dimensions. The fabricated dimensions that differ from the designed dimensions in Table 2.3 are listed in Table 4.1. Also listed are material properties and constants needed to perform dynamic analysis on the system. Young's modulus, *E,* and the spring constant, k_s, were determined experimentally

through tensile testing. The masses listed include the mass of the output accelerometer as well as the dynamic mass of the beams and spring. Photographs of the SLS fabricated designs are presented in Figure 4.3.

Table 4.1. *Fabricated dimensions, material properties and constants of vibration isolation systems*

	Single-Beam	**Double-Uncoupled**	**Double-Coupled**
h	2.7 mm	2.81 mm	2.9 mm
w	8.11 mm	8.27 mm	8.14 mm
l_0	153.47 mm	153.59 mm	153.13 mm
m	0.0100 kg	0.0115 kg	0.0117 kg
	Common Material Properties and Constants		
E	1558 MPa		
k_s	860 N/m		
d	2.33 mm		

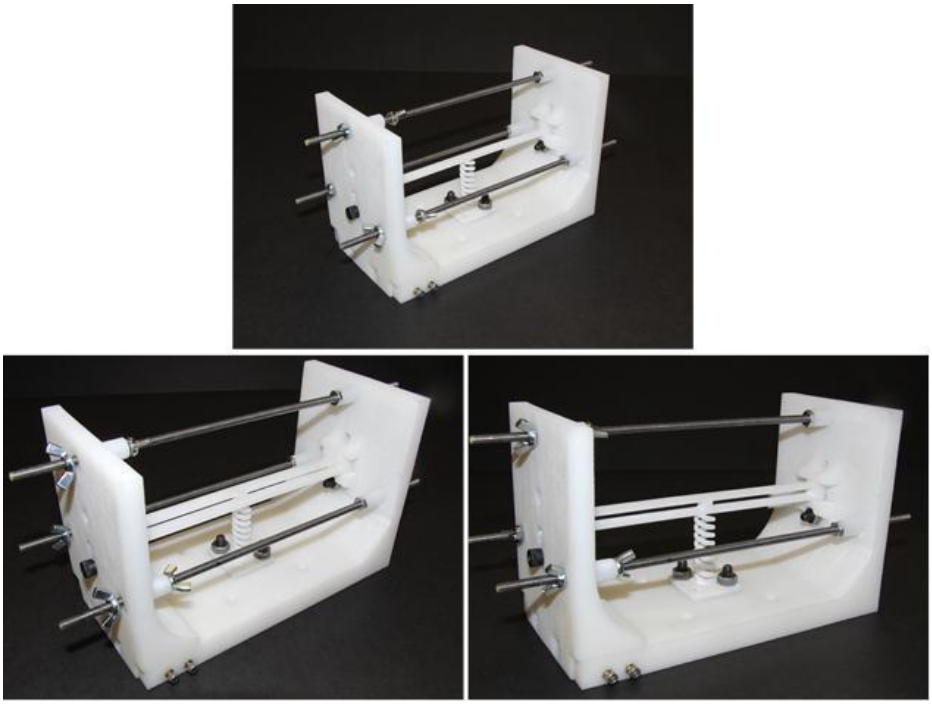

Figure 4.3. *Fabricated vibration isolation systems: single-beam system (upper), uncoupled double-beam system (lower-left), coupled double-beam system (lower-right)*

4.2 SHOCK SYSTEM

4.2.1 CAD Modeling

A CAD image of the shock isolation concept can be seen in Figure 4.4. Due to the similarities in the vibration and shock isolation concepts, the two designs have many similar geometrical features. However, the two designs have many differences as well, driven by the following considerations: the shock isolation model is designed to carry a much larger amount of weight, have significant travel available between the base and the mass, constrain the beam to buckle into the third mode, and incorporate means for one-way damping. The differences are labeled in Figure 4.4.

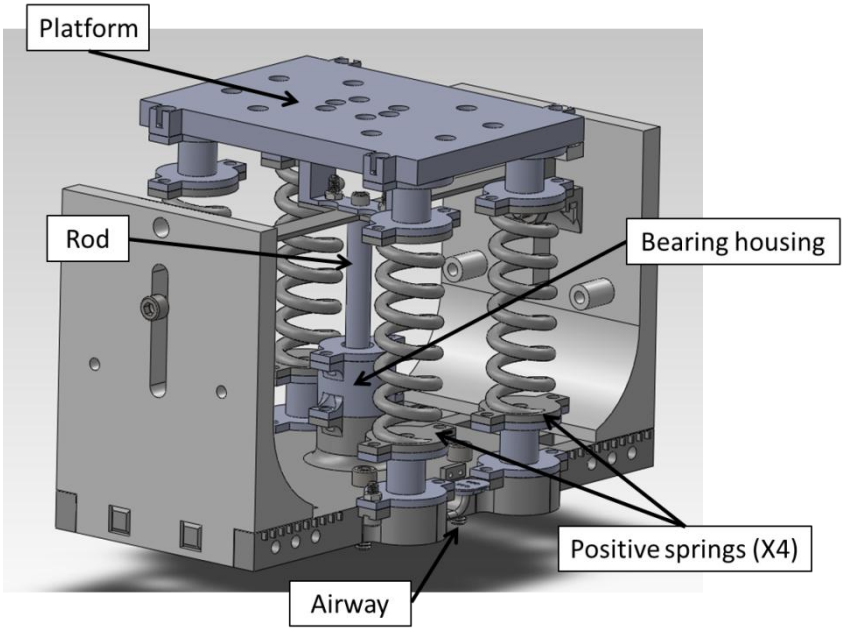

Figure 4.4. *Shock isolation system, labeled to highlight differences from vibration isolation systems*

The additional weight is due to a platform which, in future testing, will carry the vibration isolation system in series. In order to give the platform torsional support, four positive stiffness springs are placed under the four corners of the platform. The springs

are made large to provide sufficient travel before reaching their solid lengths. A rod is attached at the midpoint of the beam to keep the beam from rotating at its midpoint. The rod slides relative to the base through a bearing which is housed in the base. By design, this constraint prevents the beam from buckling into the second mode, causing it to instead buckle into the third mode. As the rod slides toward the base through the linear bearing, it pushes air through holes on either side of the base. In order to make an attempt at providing one-way damping, check valves, which only allow flow in one direction, attach to these holes to provide suction as the rod slides away from the base.

Additional CAD images of the shock isolation design are presented in Figure 4.5. Although the beam in Figure 4.5 is in a horizontal non-buckled shape, when it is compressed it buckles upward into its first mode. As the beam buckles it carries the platform upward with it because the springs are not yet attached. Once the beam is buckled to a desired level, the springs are attached between the platform and base with shims of an appropriate height to ensure that the springs begin at free length.

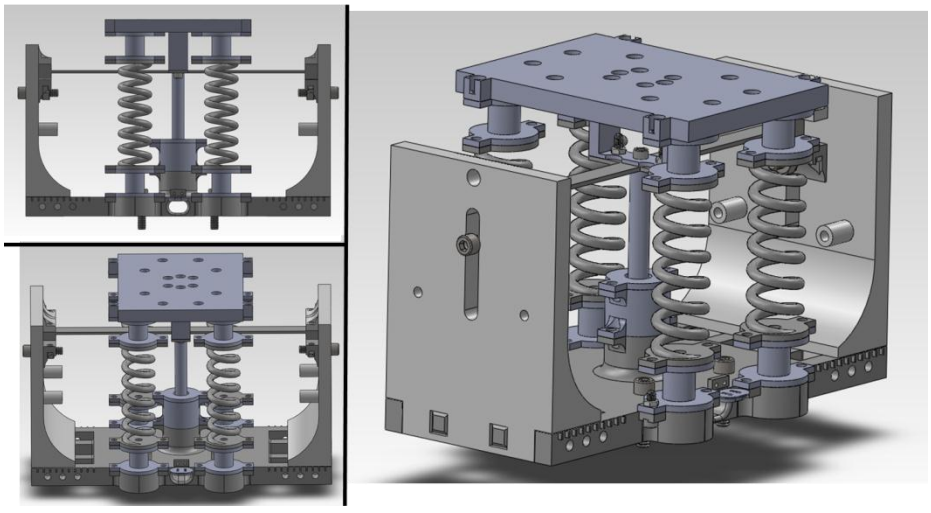

Figure 4.5. *CAD images of shock isolation design*

4.2.2 Fabricated Dimensions

As in the vibration isolation system, the SLS fabricated dimensions are generally larger than the designed dimensions. The fabricated dimensions of the shock isolation system, Young's modulus of the material, and the summed spring rate of the linear springs are recorded in Table 4.2. Young's modulus and the spring rates were determined experimentally through tensile testing. The mass value includes various assembly components as well as additional mass bolted to the platform in the form of an aluminum plate. A photograph of the system can be seen in Figure 4.6.

Table 4.2. *Fabricated dimensions, material properties and constants of shock isolation prototype*

l_0	0.196 m	k_s	2097.8 N/m
h	0.00277 m	E	1270e6 Pa
w	0.0127 m	m	2.1 kg
d	0.005 m		

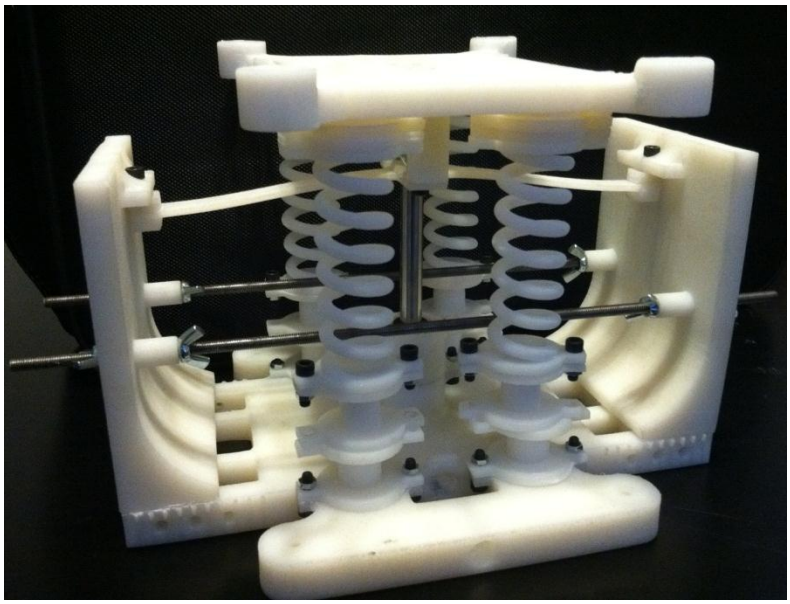

Figure 4.6. *Photograph of shock isolation system*

4.3 SUMMARY

CAD models of the vibration and shock isolation systems were designed with modular features which allow components to be interchanged. Each model was fabricated using SLS. Post-fabricated dimensions of the beams were measured, along with other important properties such as the elastic modulus and the mass of specific components, in order to more accurately compare experimental results with analytical predictions in the following chapters.

Chapter 5

Testing the Vibration Isolation Systems

5.1 Experimental Setup

Each of the vibration isolation systems was tested for its dynamic response through the use of a shaker table. The process of exciting a vibration isolation system and acquiring the transmissibility response is described in this section. The chart in Figure 5.1 maps the signal flow through the equipment. Table 5.1 lists the equipment vendors and model types used for testing. A user first interacts with software to specify the type of signal with which to excite the system. For measuring transmissibility, chirp signals are a very efficient option. The CPU sends this information to a dynamic signal analyzer, which generates the desired signal and sends it to a power amplifier. Once amplified, the signal then travels to the shaker table to excite the vibration isolation system at its base.

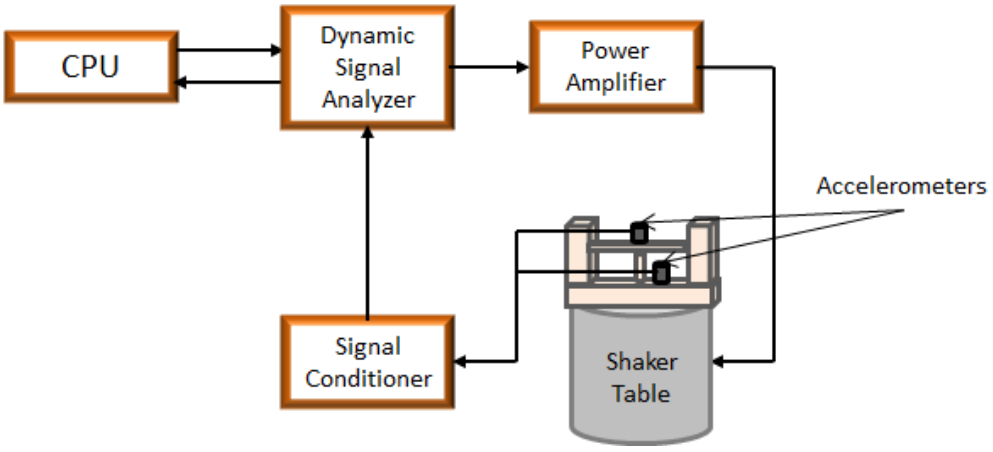

Figure 5.1. *Vibration testing signal map*

Table 5.1. *Vibration testing equipment*

Part	Vendor	Model
Dynamic signal analyzer	DataPhysics	ACE
Power amplifier	Crown Audio	XTi 2000
Shaker table	LabWorks	ET-139
Accelerometers	PCB Piezotronics	352C33
Signal conditioner	PCB Piezotronics	482C Series

Two accelerometers are used to measure the response of the system. One accelerometer rests on the base of the system and the other is placed at the midpoint of the beam. The accelerometer signals are routed through a signal conditioner for preamplification before traveling back to the signal analyzer. The signal analyzer then performs discrete sampling of the signals and sends the resulting data to the CPU. Software converts the data to the frequency domain and plots the transmissibility of the system.

Chirp signals are time-harmonic signals in which the frequency is a function of time. For testing the transmissibility of the vibration isolation systems in the current research, the chosen input frequency range was 0 Hz to 150 Hz. Thus, the frequency of the harmonic input sweeps from 0 Hz to 150 Hz over the length of the chirp signal. The amplitude of the signal is approximately one volt as generated by the dynamic signal analyzer, however this amplitude increases when the signal passes through the power amplifier.

5.1.1 Strain Gauge Setup

In these systems, the beams are compressed through the turning of nuts on threaded rods. In previous research [7], compression on the beams was measured by dividing the number of rotations of the nuts by the pitch of the threads. However, this method of measurement can contain a significant amount of error relative to the low

levels of compression needed to study the systems. A significant source of error lies in the fact that as the beams begin to buckle, the compressive advancements in the moving side wall contributes to bending of the beams rather than to axial compression. In addition, deformation of the side walls and uncertainty in the rotation of the compressive nuts with respect to the threaded rods causes error as well. In the current research, strain gauges are used to measure the level of compression on the beams. When appropriately arranged, strain gauges can measure the amount of axial compression in the beams even if bending is present. In order to arrange the strange gauges on a beam such that only compressive strains are measured, one strain gauge should be placed on the upper face of the beam and another should be placed on the lower face. The two gauges should be placed at the same distance along the length of the beam and oriented parallel to the lengthwise axis of the beam, as in Figure 5.2.

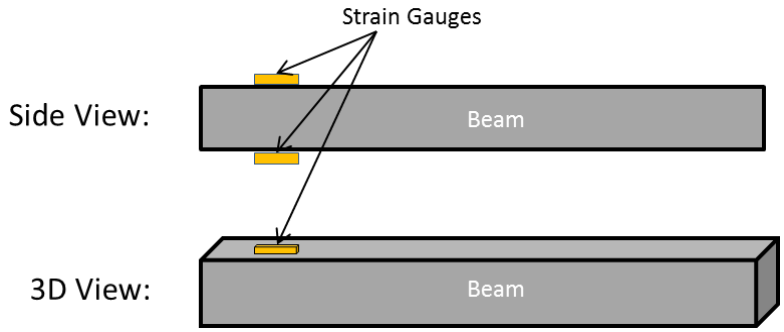

Figure 5.2. *Strain gauge arrangement for measuring compressive strain*

The strain gauges are incorporated into a well-known circuit called the Wheatstone bridge. Wheatstone bridge circuits are constructed such that one can determine unknown resistance values. Because the sensing mechanism of a strain gauge is a change in resistance with a change in strain, these circuits are widely used to determine changes in resistance for strain gauge applications. A schematic of a

Wheatstone bridge is shown in Figure 5.3. V_s and V_o are the input and output voltages, respectively, and labels 1-4 indicate arms of the bridge where electrical components can be placed.

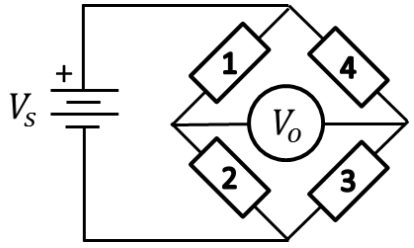

Figure 5.3. *Wheatstone bridge*

In measuring the axial strain in the beams, the strain gauges are incorporated into arms 1 and 3 of the bridge, while arms 2 and 4 contain variable resistors. Circuit analysis of the Wheatstone bridge requires that for the circuit to be balanced, meaning that the output voltage equals zero, the ratio of resistances in arms 1 and 3 should equal that of arms 2 and 4, or

$$\frac{R_1}{R_3} = \frac{R_2}{R_4}. \tag{5.1}$$

Variable resistors are often used in conjunction with Wheatstone bridges in order to balance the bridge when strain is not present. If all resistances in the bridge are initially equal and only small strains are present, the output voltage is directly related to the changes in resistance in each arm through the following relationship [21]:

$$V_o = V_s \frac{1}{4}\left[\frac{\Delta R_1}{R_1} - \frac{\Delta R_2}{R_2} + \frac{\Delta R_3}{R_3} - \frac{\Delta R_4}{R_4}\right]. \tag{5.2}$$

For this particular application, the resistances in arms 2 and 4 are fixed to equal the initial resistance in the strain gauges. In addition, the gauge factors of the strain gauges are equivalent. Given that the relationship for the gauge factor of a strain gauge is

$$\mathrm{GF} = \frac{\left(\Delta R/_R\right)}{\varepsilon}, \tag{5.3}$$

Equation 5.2 can be rewritten as follows:

$$V_o = V_s \frac{\mathrm{GF}}{4}[\varepsilon_1 + \varepsilon_3]. \tag{5.4}$$

Due to the arrangement of the strain gauges shown in Figure 5.2, the sum of strains ε_1 and ε_3 equals $2\varepsilon_a$, or twice the total axial strain in the beam. The axial strain in the beam is thus related to the output voltage through:

$$\varepsilon_a = \frac{2}{V_s \mathrm{GF}} V_o. \tag{5.5}$$

The selection of strain gauge resistance is of particular importance for measuring strain in Nylon 11 and other plastics which may act as thermal insulators. Originally, 120Ω strain gauges were used to measure strain in the nylon beams. However, when compared with experimentally determined strain in a tensile test, the strain gauge output was highly inaccurate. This error could be a result of both changes in gauge resistivity with changing temperature and differences in the thermal expansion coefficient of the gauge and the Nylon beam. The relatively low resistance of the strain gauges resulted in enough power dissipation to induce these temperature effects. In order to avoid this error, the 120Ω strain gauges were replaced with 350Ω strain gauges. The higher resistance

resulted in less power dissipation by the strain gauges and more accurate readings. In addition to increasing the gauge resistances, one can also utilize a voltage divider to reduce the amount of power input into the Wheatstone bridge. The plot in Figure 5.4 shows strain gauge data as a function of time during tensile testing of the beams.

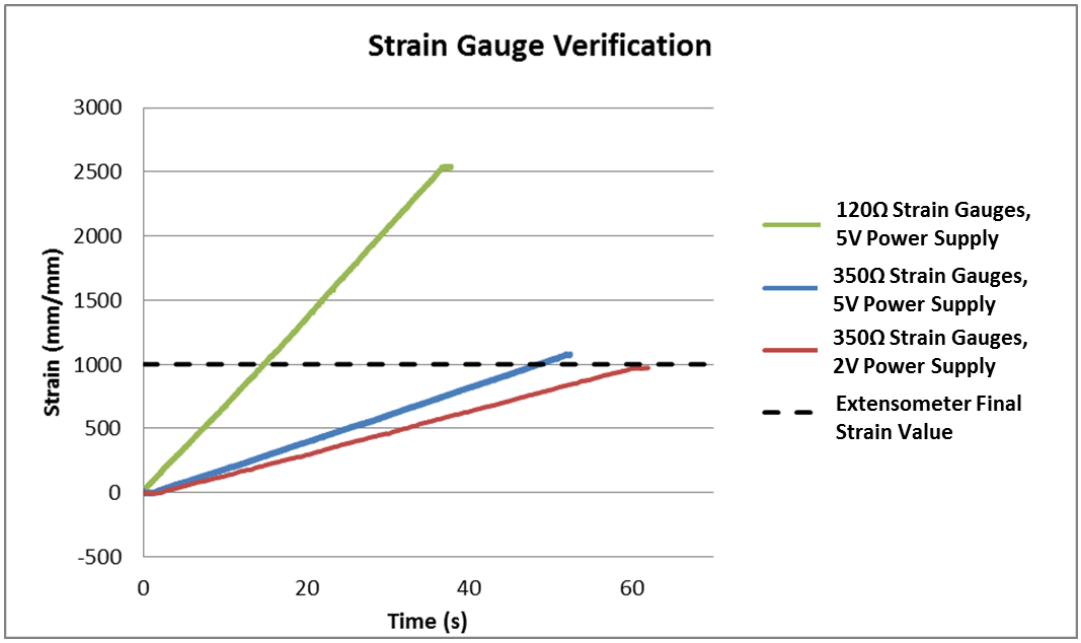

Figure 5.4. *Strain gauge verification plot*

The three curves represent three different combinations of strain gauge resistance and input voltage. During the tensile tests, an extensometer was also used to determine the strain in the beam. The strain value determined by the extensometer at the end of each test is displayed as a horizontal dashed line. For each curve, any deviation in the final strain gauge value from this line indicates error in the strain gauge measurement. As shown in Figure 5.4, the 350Ω strain gauges produce much more accurate results than the 120Ω strain gauges. Decreasing the input voltage also increases the accuracy of the strain gauge output.

5.1.2 Accelerometer Wire Orientation

In performing the vibration measurements, the orientation of the accelerometer that rests on top of the beam is critical to obtaining good measurements. If the wire is situated perpendicular to the length of the beam as depicted in Figure 5.5(a), low frequency torsional vibration modes are induced which disrupt the transverse motion of the isolation system. In this case, the transverse transmissibility of the system is difficult to determine. However, if the wire is oriented parallel to the length of the beam as in Figure 5.5(b), the transverse mode is primarily excited and the desired transmissibility is readily measured.

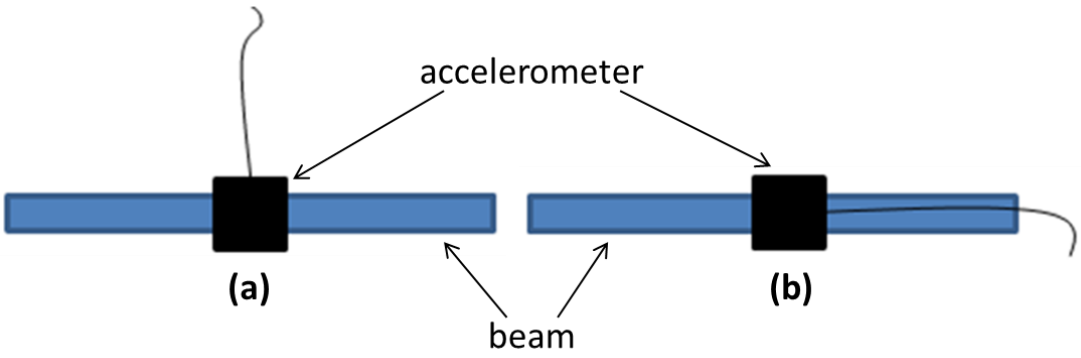

Figure 5.5. *Accelerometer wire orientation: (a) perpendicular versus (b) parallel*

Representative transmissibility plots for the two cases are displayed in Figure 5.6. In the perpendicular case, multiple resonances occur due to the combination of the torsional and transverse vibrational modes. In the parallel case, the transmissibility signal is very clean and representative primarily of the transverse motion.

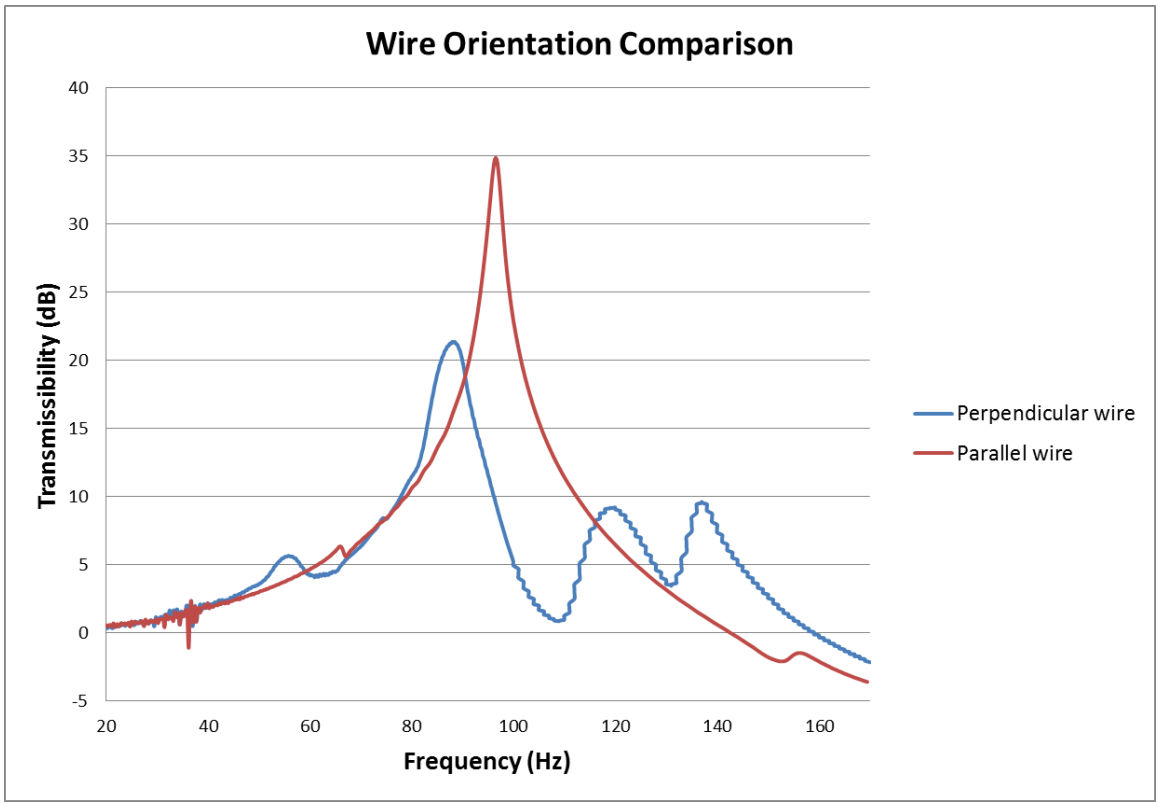

Figure 5.6. *Transmissibility plots for two accelerometer orientations*

5.2 Experimental Results and Discussion

The vibration isolation systems described in Section 4.1 were tested and the results presented in this section. The dimensions and material properties of the vibration isolation systems are listed in Table 4.1, and the chirp signal used to excite the systems is described in Section 5.1.

5.2.1 Transmissibility

The experimental transmissibility of the three vibration isolation systems follows similar trends to the data from [7]. However, in the current research, the use of strain gauges to measure compression in the beams causes the data to match much more closely with analytical predictions. The experimentally determined transmissibility curves of the

single-beam system, plotted in Figure 5.7, correspond well with the analytically predicted curves generated from Equation 2.34. Although the magnitudes of the experimental curves at resonance are consistently less than those of the analytical curves, the frequencies at which the peaks occur are very consistent. This correspondence between resonant frequencies provides strong validation of the analytical models derived in Chapter 2. The discrepancy in peak magnitudes of the experimental and analytical curves could be due to off-axis accelerometer motion along with unaccounted-for material damping in the beam. The magnitudes of the resonance peaks in the analytically determined curves can be lessened by choosing a higher damping coefficient.

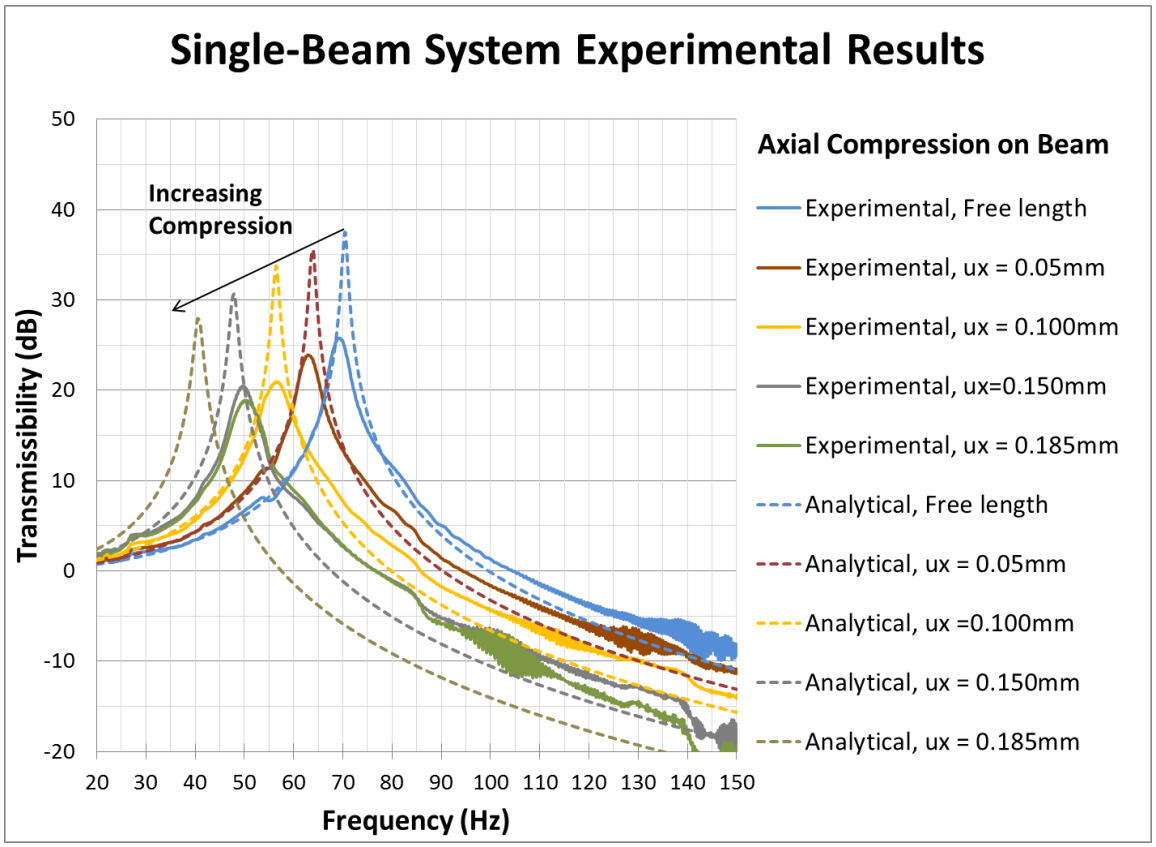

Figure 5.7. *Single-beam system transmissibility*

In the single-beam system, the system begins to buckle into its first mode near a compression of 0.15 mm. Once this buckling begins to occur, any further compression at levels under the first-mode buckling limit contributes not only to increased compressive strain, but also to increased bending strain in the beam. As the beam gradually bends into its first-mode shape under increasing compression, a transition occurs at which the beam no longer decreases in stiffness with increased compression, but rather increases in stiffness. This effect can be seen in Figure 5.7 as the experimental resonance frequency of the system begins to increase for small compressions greater than 0.15 mm. As the beam is compressed at levels below the critical buckling limit of the system, the tendency of the beam to gradually bend into higher amplitude first-mode shapes is referred to as soft-buckling in this research. Soft-buckling, which is further discussed in Section 5.2.2, occurs due to geometric and boundary condition imperfections in the systems.

The experimentally determined transmissibility curves for the double-beam systems are plotted alongside analytical predictions in Figure 5.8 and Figure 5.9.

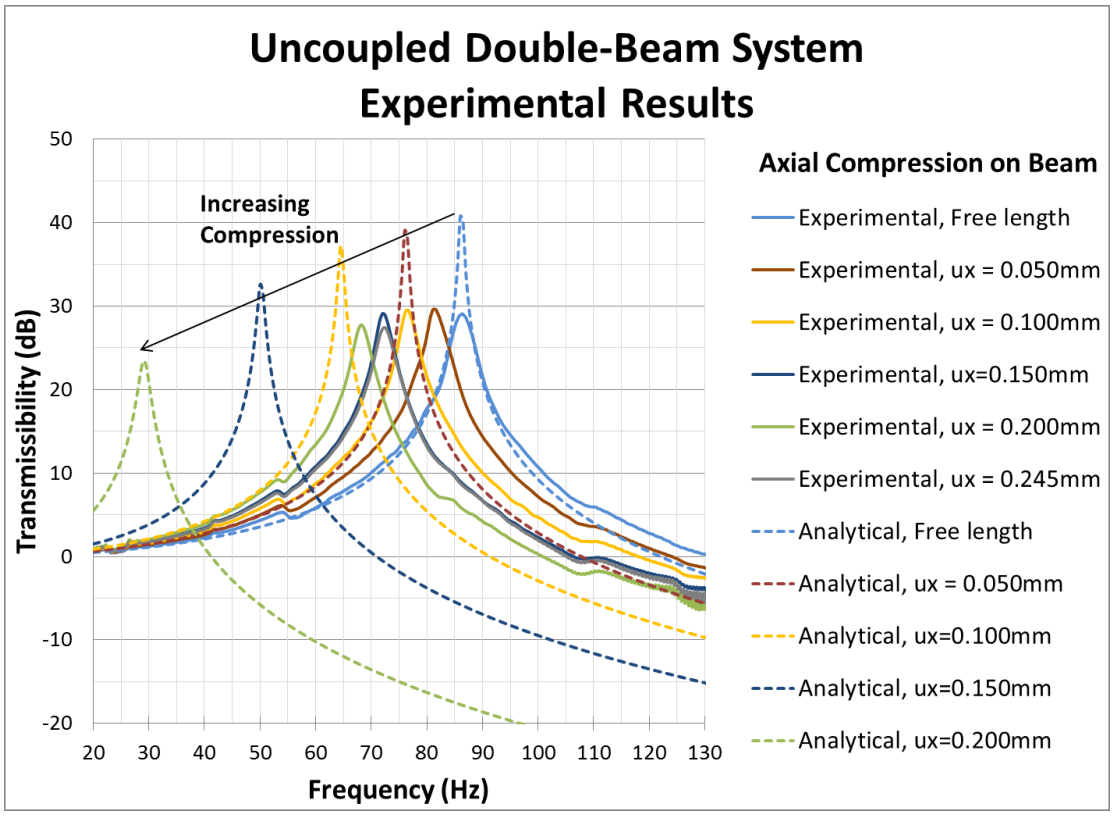

Figure 5.8. *Uncoupled double-beam system transmissibility*

As the beams in the uncoupled double-beam system are placed under increased axial compression, the analytical and experimental curves deviate further from each other than in the single-beam system. This deviation is due to the fact that the soft-buckling effect is much more prevalent in the uncoupled double-beam system than in the single-beam system. The initial uncompressed resonant peak from the experimental data still aligns well with the analytical predictions.

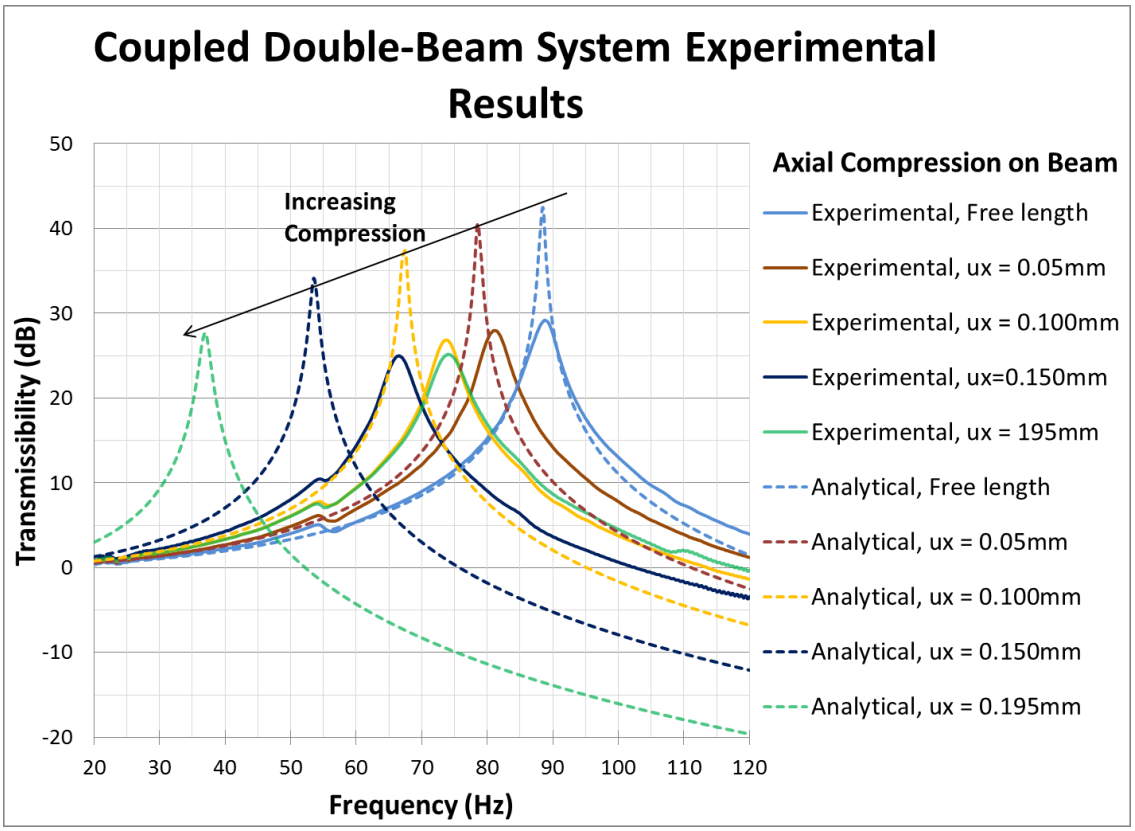

Figure 5.9. *Coupled double-beam system transmissibility*

As compared to the uncoupled double-beam system, the experimental curves in the coupled double-beam system more closely match the analytical curves. Although the soft-buckling effect still prevents the double-coupled beam system from reaching the expected low levels of resonance frequency, the fact that soft-buckling is less prevalent represents a benefit over the uncoupled double-beam system. However, it is not evident that the difference in coupling between the two prototypes is the reason for this benefit. Other factors, such as differences in imperfections between the beams and boundary conditions, could be the primary reasons for the inconsistency between the two designs. If a stiffer constraining spring is used in future testing, it is likely that the coupled double-beam system would display a greater reduction of overall system stiffness prior to the

beams buckling into a higher mode, as compared to the uncoupled double-beam system. This is due to the restriction of second-mode buckling caused by the coupling link in the coupled double-beam design.

5.2.2 Soft-Buckling Effect

Given the fabricated dimensions and constants listed in Section 4.1.2 for each system, the first-mode critical buckling limit (Equation 2.36) for each system occurs at a lower compression level than that of any other buckling mode. Thus, each system should buckle into the first mode when the beams are compressed. Theoretically, each system should be able to reach zero stiffness when compressed up to its first-mode buckling limit, considering that this buckling limit is defined to equal the compression level at which the total system stiffness is zero. However, from a practical standpoint, geometric and boundary condition imperfections cause the systems to buckle with much less compression than predicted. This premature buckling is referred to as soft buckling in this research. Soft-buckling presents the largest difficulty in bringing the systems to near-zero resonant frequencies.

To understand the meaning of soft-buckling, one can consider the following potential imperfection in beam geometry for the vibration isolation systems: the midpoint of the beam experiences an initial transverse displacement. This type of imperfection is likely present in the fabricated prototypes due to the curling of parts, a common cause of dimensional inaccuracies in SLS. An exaggerated view of this example imperfection is shown in Figure 5.10.

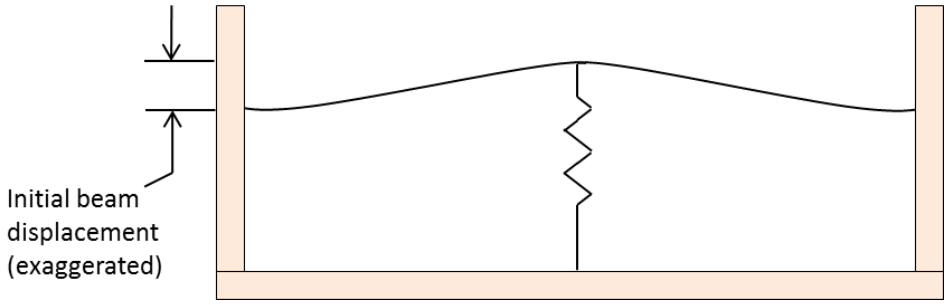

Figure 5.10. *Potential geometrical imperfection in the vibration isolation prototypes*

Soft-buckling means that as the beam is compressed at levels below the first-mode buckling limit of the system, the system gradually buckles into a higher amplitude first-mode shape. Theoretically, if a beam with zero imperfection is compressed prior to the system reaching its first-mode critical buckling limit, the beam will experience purely compressive strains. If a beam experiences purely compressive strains, then no mode shape is present and the beam remains flat. However, when soft-buckling occurs in an imperfect system, the beam experiences both bending and compressive strains even when the compression levels are below all buckling limits. As the beam is compressed at levels below the first-mode buckling limit of the system, the amount of bending present in the beam corresponds to the extent of soft-buckling present in the system.

Figure 5.11 shows the effect of soft-buckling on the behavior of the system. The curves, generated through FEA modeling [22], are representative system stiffness versus compression curves for varying levels of imperfection. As seen from these curves, even the slightest imperfection can have a large impact on the beams' behavior when placed under axial compression. As the beam is compressed, the system reaches a minimum stiffness value near the predicted level of pre-compression, but the lowest achievable stiffness is much higher than predicted. This phenomenon worsens as the amount of

imperfection (measured as the distance between the midpoint of a perfect beam and a beam with preexisting curvature) increases.

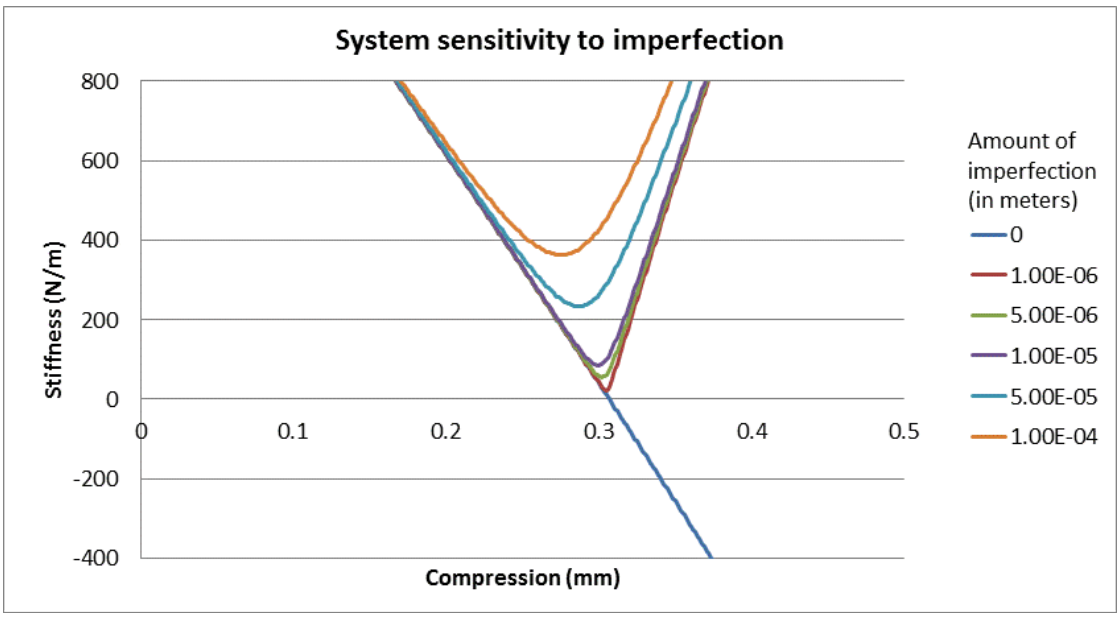

Figure 5.11. *Single-beam system sensitivity to imperfection [22]*

Specifically, as shown in Figure 5.11, the representative system with zero imperfection crosses into the negative stiffness region at 0.3 mm of compression. Practically, the system could never reach this negative region because the smallest amount of imperfection would cause buckling into one of its bistable configurations. Therefore, 0.3 mm is the theoretical first-mode buckling limit of the system. The orange curve in Figure 5.11 shows that given a small imperfection of 0.1 mm initial beam displacement, the lowest amount of stiffness the system can reach is roughly 350 N/m. Other forms of imperfection are also likely to exist in the prototypes which further contribute to soft-buckling, such as moments imposed on the beam end-points by the compressing wall. It is clear that a high level of precision is needed to reach the near-zero system stiffness required to reach low resonant frequencies.

Material creep in the beams could also be a factor in causing the discrepancy between experimental and theoretical results. The prototypes were fabricated with Nylon 11 material which is susceptible to creep. Creep is noticeable in the specimens if they remain under compression for more than approximately five minutes.

5.2.3 System Stiffness Versus Compression Curves

Viewing the stiffness of the systems as a function of the axial compression on the beams provides additional insight into the soft-buckling behavior of the prototypes. In order to produce the experimental curves in Figure 5.12, Figure 5.13, and Figure 5.14, the system stiffness values for each level of compression were calculated using the definition of resonance frequency for a second-order system, $\omega_n = \sqrt{\frac{K}{m}}$. Thus, the resonant frequencies for each level of compression in transmissibility plots and the total dynamic masses were used to determine the system stiffnesses. It should be noted that the resonant frequencies in the transmissibility plots are in units of hertz, whereas the aforementioned equation for resonance frequency assumes units of radians per second. Dividing ω_n by 2π converts the resonance frequency to hertz.

Figure 5.12 displays the analytically predicted and experimentally measured single-beam system stiffness versus axial compression, along with vertical lines to indicate the first and second-mode critical buckling limits. The slopes of the experimental and analytical stiffness versus compression curves are very similar until the system begins to soft-buckle. Since the first-mode buckling limit of the system occurs at a lower compression level than the second-mode buckling limit of the beam, the system is expected to buckle into the first mode at the first-mode critical compression limit. However, the system begins to buckle into the first mode at a much lower compression level than expected, roughly 0.15 mm, as a result of soft-buckling.

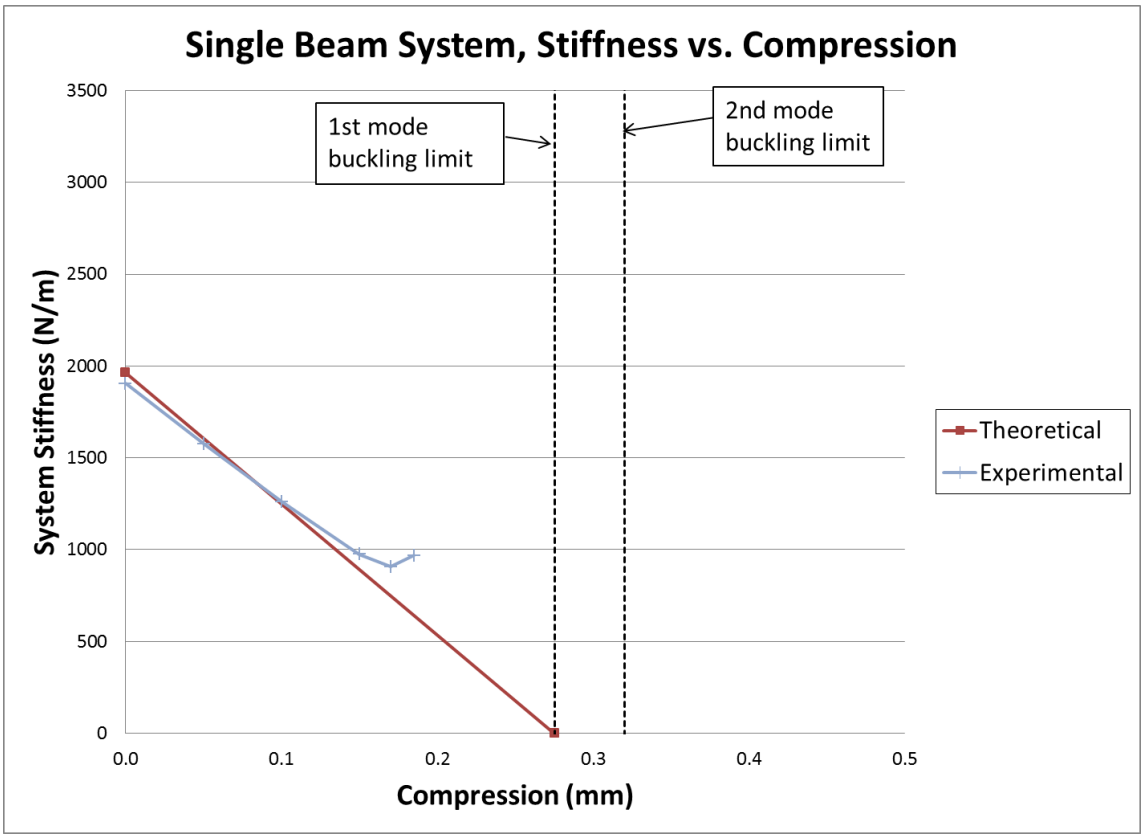

Figure 5.12. *Single-beam system stiffness versus compression*

The stiffness versus compression plots for the two double-beam systems are displayed in Figure 5.13 and Figure 5.14. Compared with the single-beam system, the experimentally determined stiffness versus compression curves of the double-beam systems do not match as closely with the analytically predicted curves. The double-beam systems have a higher tendency to soft-buckle, which may be because the constraining spring is not as proportionately stiff with respect to the stiffness of the beams, and therefore cannot resist the soft-buckling as well. In fact, the uncoupled double-beam prototype begins soft-buckling almost immediately upon introducing axial compression on the beams. The differences in slope between the experimental and analytical curves in Figure 5.13 and in Figure 5.14 indicate this soft-buckling behavior.

The uncoupled double-beam prototype tends to soft-buckle to a greater extent than the other two vibration isolation systems. As previously mentioned, the difference in soft-buckling between the two double-beam prototypes could be due to the difference in coupling between the beams. This result would indicate that the coupled double-beam design provides the benefit of greater stability during compression; however, it is not entirely clear whether the difference in coupling is the cause of this inconsistency between the two double-beam designs. Once again, boundary condition differences and differences in manufacturing imperfections could also contribute to the inconsistency.

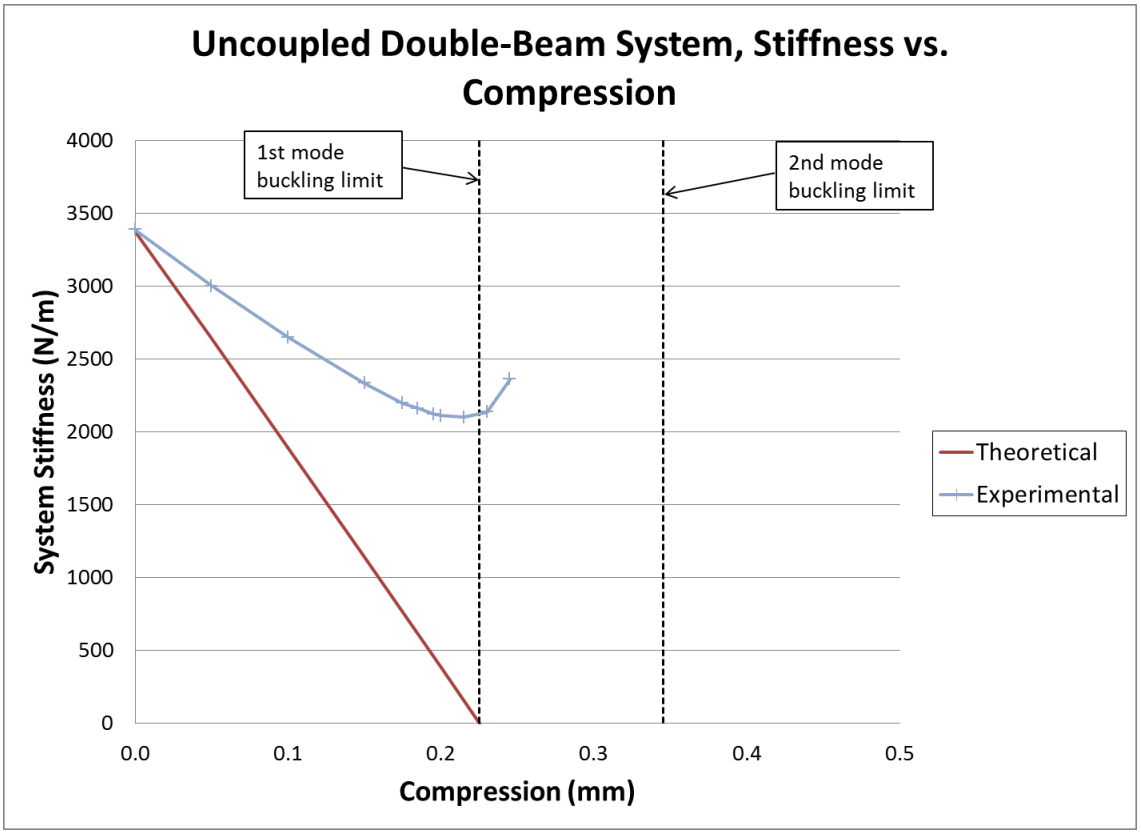

Figure 5.13. *Uncoupled double-beam system stiffness versus compression*

The similarity between the initial analytical and experimental stiffness versus compression slopes in the coupled double-beam design indicate a lesser extent of soft-buckling than in the uncoupled double-beam design. An important observation from Figure 5.14 is that the initial slope of the experimental data is noticeably steeper than in the other two designs. This steep negative slope represents the potential of the system to counteract a more positively stiff spring prior to buckling into a higher mode. If a stiffer positive spring is used, the system has an increased payload carrying capacity. Unfortunately, soft-buckling prevents the system from realizing its full potential.

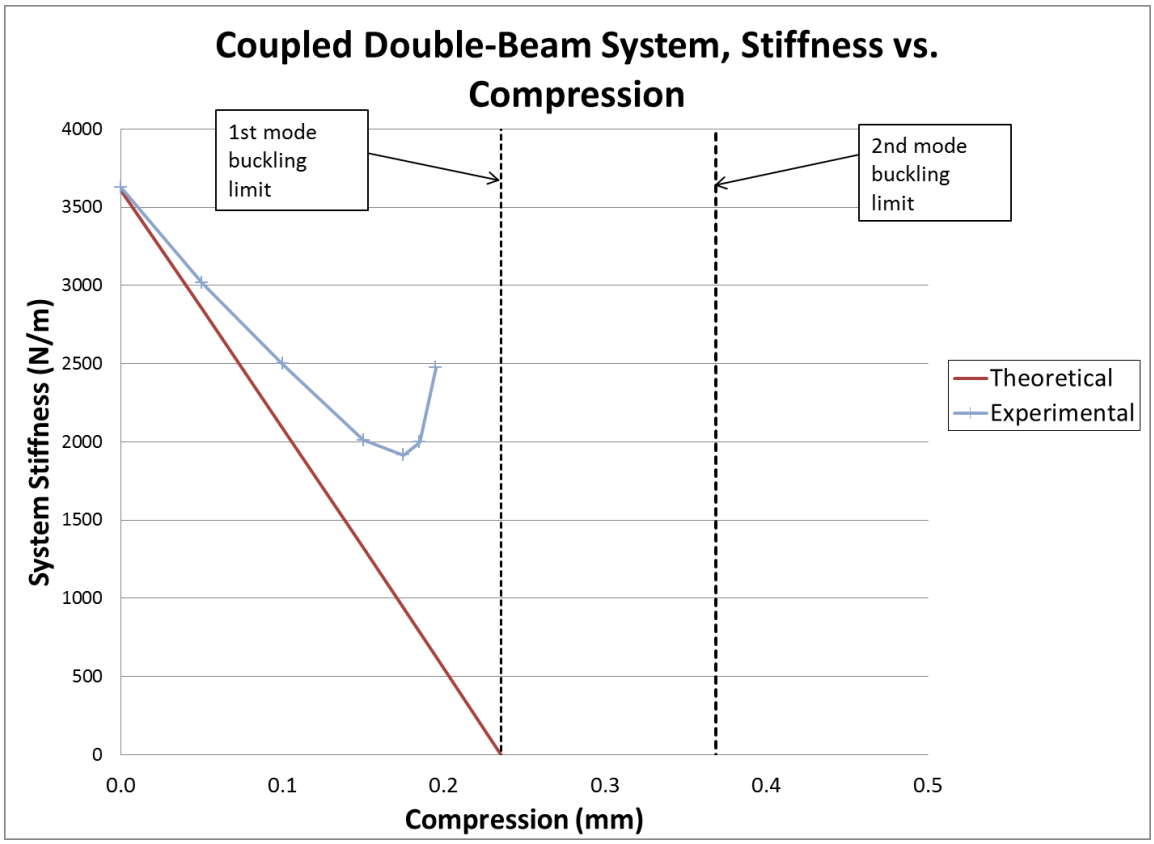

Figure 5.14. *Coupled double-beam system stiffness versus compression*

5.3 SUMMARY

Transmissibility testing was performed for each vibration isolation system. Strain gauges were used to obtain accurate levels of compression in the beams such that in the absence of soft-buckling, the experimental data corresponds well with analytical predictions. Trends of decreasing resonance frequency with increasing axial compression on the beams were observed, and the inability of the systems to reach the expected low levels of resonance frequency was investigated. The soft-buckling phenomenon in the compressed beams was discussed as the primary reason for this inability. Soft-buckling occurs due to geometric imperfections in the system as well as to boundary condition flaws. Small levels of imperfection were modeled using FEA in an example study, inducing soft-buckling and drastically affecting the transverse stiffness characteristics of a beam placed under compression.

As opposed to the single-beam design, the coupled double-beam design displayed greater reductions in total stiffness and resonance frequency with respect to axial compression. Although soft-buckling prevented the double-beam systems from displaying the desired low levels of dynamic stiffness, these greater reductions in stiffness indicate the potential of the coupled double-beam system to counteract a more positively stiff spring prior to buckling into a higher mode. This characteristic represents the ability of the coupled double-beam system to carry higher payloads. Soft-buckling prevented the uncoupled double-beam from displaying this benefit. The difference in coupling between the two double-beam designs was noted as a possible, but not definitive, reason for the greater extent of soft-buckling in the uncoupled double-beam design.

Chapter 6

Testing the Shock Isolation System

6.1 Experimental Setup

The shock testing was carried out using the same equipment and setup described in Section 5.1. Therefore, the signal map from Figure 5.1 represents the shock testing as well and is reproduced below in Figure 6.1. The sole difference between the two types of testing lies in the input signal used to excite the systems. Whereas the vibration tests use a chirp signal to excite the base, the shock tests use a low frequency square wave signal to excite the base. The square wave travels through the equipment as a voltage signal until the shaker table converts it to velocity. As the derivative of velocity with respect to time is acceleration, the velocity square wave represents a form of impulse in terms of acceleration.

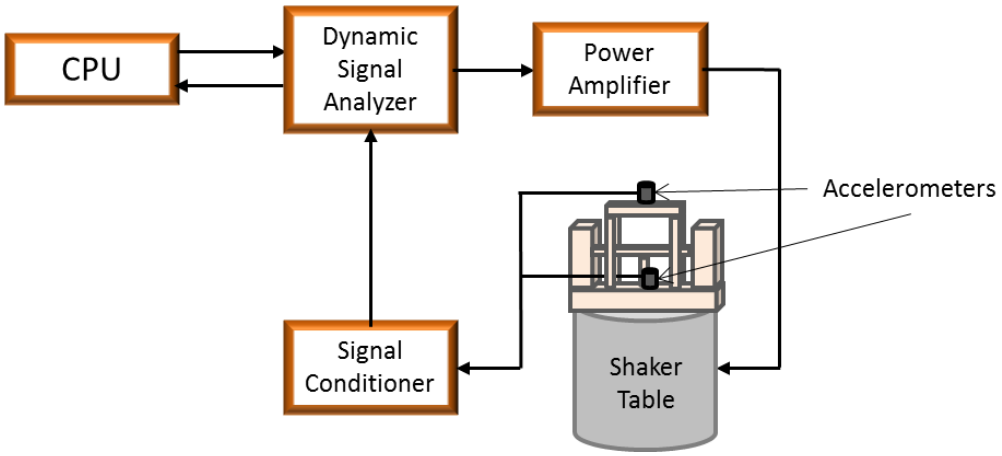

Figure 6.1. *Shock testing signal map*

Due to the bending experienced by the beams in the shock prototype, strain gauges cannot be used to accurately determine the distance between the endpoints of the beam. Once the beam is fully buckled, any further compression from the sliding walls of the system contributes only to further bending of the beam. Since a measurement of compressive strain with zero or low bending present in the beam is needed to accurately determine the distance between the walls, strain gauges cannot be used for this purpose. As a side note, strain gauges could still be used to determine the level of compressive strain within the beam in order to validate critical buckling limits for first and third-mode buckling. However, this validation is not performed in the current research.

6.2 Experimental Results and Discussion

6.2.1 Force Versus Displacement Curves

Prior to measuring the response of the shock isolation prototype to an impulse load, force versus displacement curves of the beam and system were directly measured through the use of an Instron tensile testing machine. Mounting holes located on the base and platform allow for the attachment of handles in order to make tensile measurements possible. The jaws of the Instron machine were used to clamp onto these handles for displacement-controlled testing. In the first set of tensile tests, these constitutive curves were measured for the beam alone for varying levels of axial beam compression. This measurement allows for the comparison of experimental data with the analytically derived constitutive relationship of the beam (refer to Equation 3.12). In order to obtain the total system constitutive relationship, the four positive stiffness springs were then attached in parallel with the beam. Alternatively, the linear constitutive relationships of the springs, also measured individually through tensile testing, could be directly summed

with the constitutive curve of the beam. Photographs of the tensile testing setups for the beam alone and for the system are displayed in Figure 6.2.

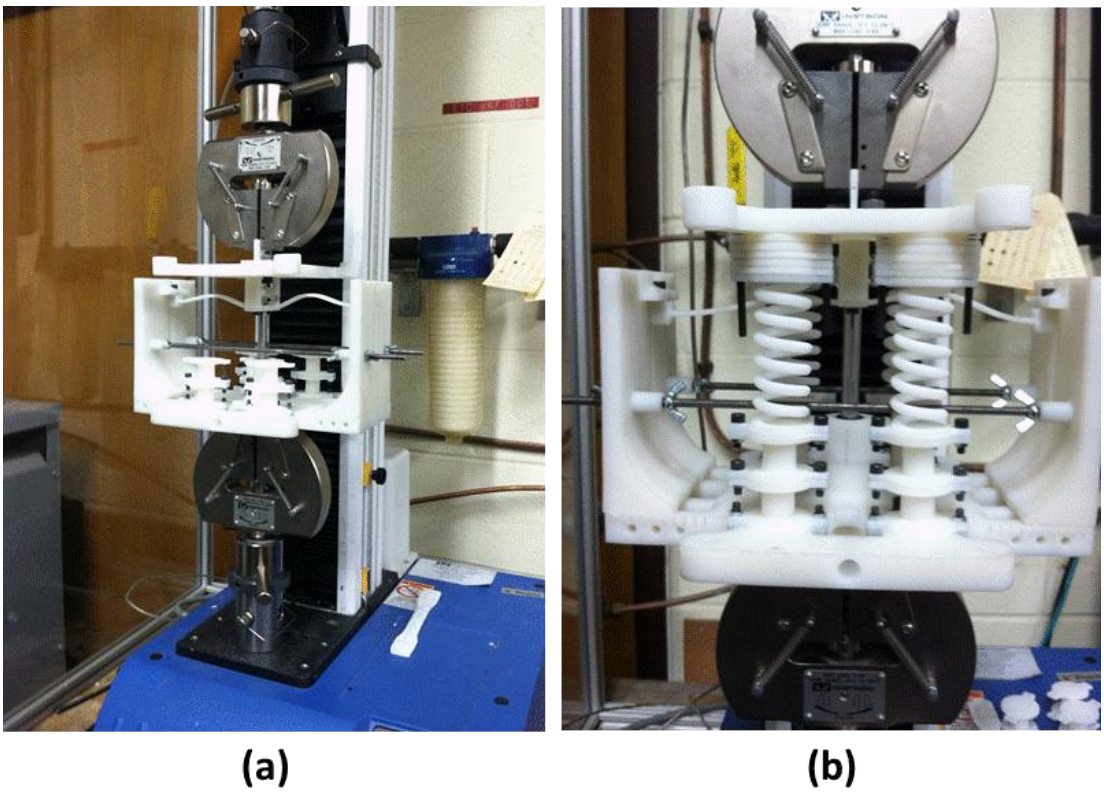

Figure 6.2. *(a) Constrained beam tensile testing setup and (b)Shock isolation system tensile testing setup*

In the photographs of Figure 6.2, the beam is buckled into its third-mode shape while the tensile testing jaws displace the platform and base relative to each other. Note that in Figure 6.2(b), shims are positioned in between the springs and the platform. These shims allow the springs to rest at free length when the system is in its stable first-mode buckled configuration.

The plots in Figure 6.3 show the results of the tensile testing of the beam. Dashed lines are used to represent the analytical predictions made by Equation 3.12, and solid

lines represent the measured data from tensile testing. An important issue to note is that the level of repeatability for these constitutive measurements is low. As the beam is compressed to different levels, the compressive walls have a tendency to pivot in an unpredictable fashion about the guide rods on the base rather than smoothly slide. A potential means of avoiding this issue would be to use linear bearings and steel rods to mate the walls with the base. This potential design improvement should be investigated in future work. The measured constitutive curves in Figure 6.3, then, are representative of types of trends seen in the tensile testing, but they are not necessarily indicative of the exact behavior of the beam with respect to axial compression.

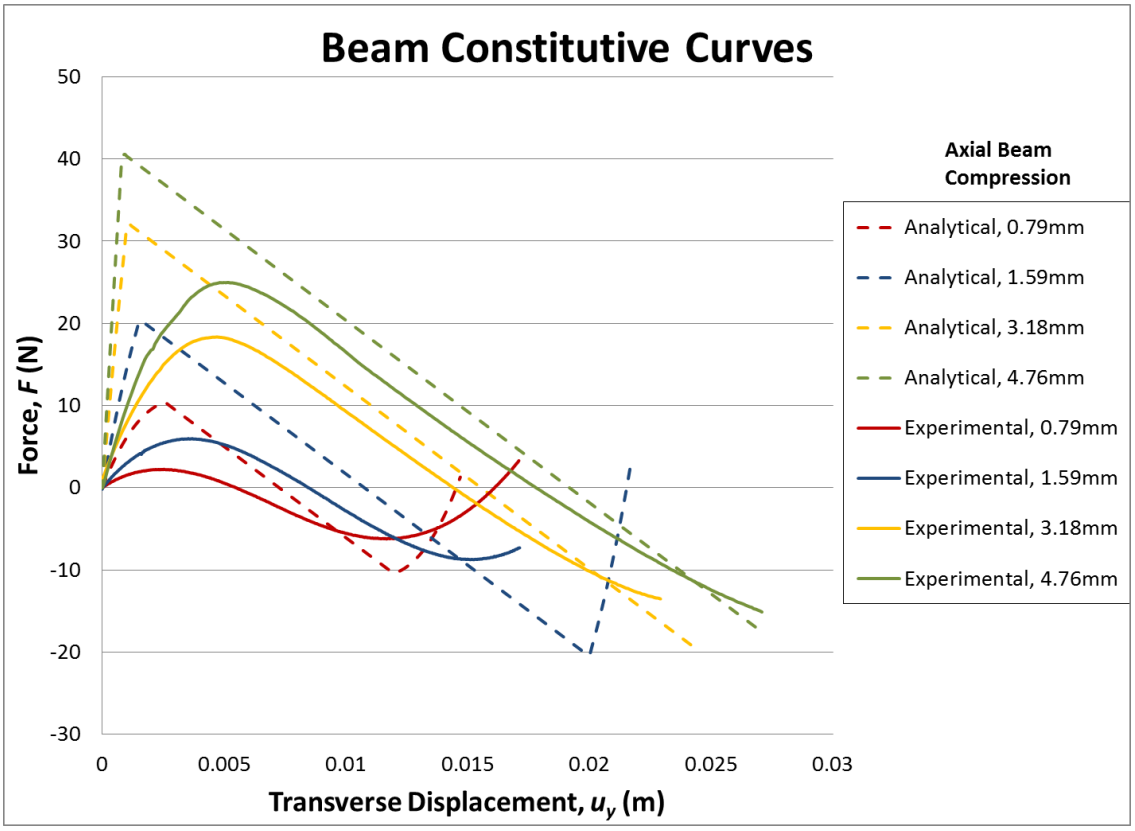

Figure 6.3. *Beam analytical versus experimental constitutive curves*

When measuring the 3.18 mm and 4.76 mm compression curves displayed in Figure 6.3, the beam visibly transitioned from a first-mode buckled shape into a third-mode shape as transverse displacement was applied. When measuring the 0.79 mm and 1.59 mm curves, however, the beam appeared to stay in a first-mode shape. The transition from first to third mode in the 3.18 mm and 4.76 mm compression tests is represented in the constitutive curves by the transition from a third-order polynomial to a region of linear, negative slope at roughly 5 mm of transverse displacement.

A common trend in all of the constitutive beam measurements, including those in Figure 6.3, is that the initial stiffness of the beam is not as high as expected. This could be due to the fact that the compressive walls of the system appear to flex under the axial load of the beam as the beam is compressed. Rigid boundary conditions are assumed in the derivation of the analytical model, so any flexibility in the actual prototype could cause a difference between the experimental and analytical curves. Material creep could also be a factor in the error between the experimental and analytical curves. If compressive strain in the beams is relieved through material creep during the tensile tests, it is likely that the experimental curves would display lower levels of initial stiffness. This discrepancy should be addressed in future prototypes such that the more ideal predicted behavior of the curves is preserved in the prototypes. Since an ideal shock isolator has infinite initial stiffness, the prototype's initial stiffness should be maximized.

A positive note about the experimental trends in Figure 6.3 is that when the beam is under relatively high compression, the level of negative stiffness matches well with analytical predictions. As seen in the orange and green curves of Figure 6.3, the linear portions of the analytical and experimental curves follow a very similar negative slope. This result is expected because once the beam is buckled into the third mode, the negative stiffness value is predicted to remain constant in Equation 3.12 even as more compression

is applied from the side walls. Thus, potential issues such as non-rigid boundary conditions should not affect the level of negative stiffness as long as the beam remains buckled in the third mode.

Referring back to Figure 6.2(b), constitutive curves of the total system were measured as well. The 3.18 mm and 4.76 mm curves, plotted in Figure 6.4, display the desired trends of having relatively high stiffness at low displacements, and having near-zero stiffness at a given force threshold for further displacements. It is important to note, however, that the system only maintains this near-constant force behavior for a given range of transverse displacement, after which the beam buckles into its lower first-mode shape and becomes highly stiff.

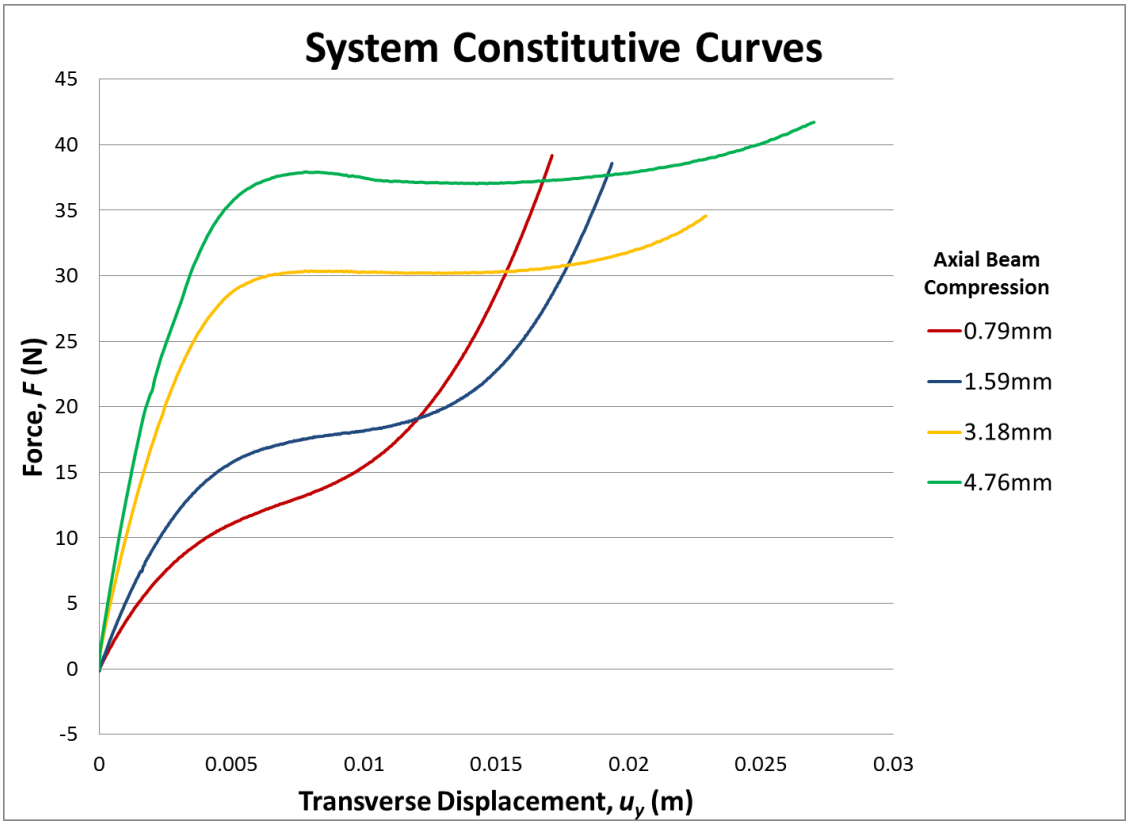

Figure 6.4. *System experimental constitutive curves*

The two curves of lower compression also display softening, but the axial compression in the beam is not high enough in either case to create the magnitude of negative stiffness required to fully counteract the positive springs. Thus, these curves do not quite reach the near-zero stiffness levels that are displayed in the orange and green curves.

6.2.2 Shock Testing

As previously mentioned, the shock isolation system was tested through the use of a low frequency, velocity square wave input signal. The system was tested for varying levels of beam compression. For the sake of discussion, the case in which the beam was compressed to 4.76 mm is presented in this section.

6.2.2.1 Acceleration Versus Time

The raw input and output accelerometer data is plotted in Figure 6.5. The input shock load reaches an acceleration of roughly 15 g's, and the mass is isolated to experience no more than roughly 1 g of acceleration (in the positive direction). The acceleration response of the mass clearly displays the ability of the system to provide isolation at a threshold acceleration level and absorb the energy of the shock at that level of acceleration. One-way damping has not been applied to the current prototype, resulting in the relatively large values of negative acceleration present in the experimental data. One-way damping, described in Section 3.3.2, should be explored in future work as a way to mitigate this negative shock.

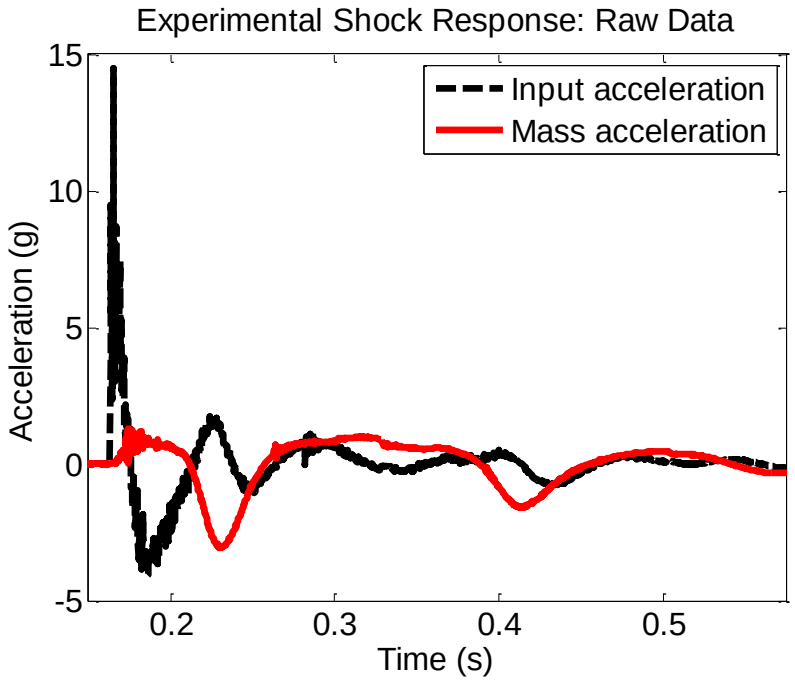

Figure 6.5. *Raw data shock response*

High frequency components of the signal cause difficulty in visualizing and characterizing the input shock. In order to better visualize the shock response data, a low-pass filter can be applied to the data. Applying an FIR low-pass filter to the shock response data yields the plot in Figure 6.6. The filter used was 50^{th} order with a cutoff frequency of 200 Hz. As a result of the data filtering, the initial positive shock can be viewed and described in terms of a representative wave form, such as versine, with a given time duration and peak amplitude. Performing this filtering also allows for clean hysteresis plots, as presented in further paragraphs.

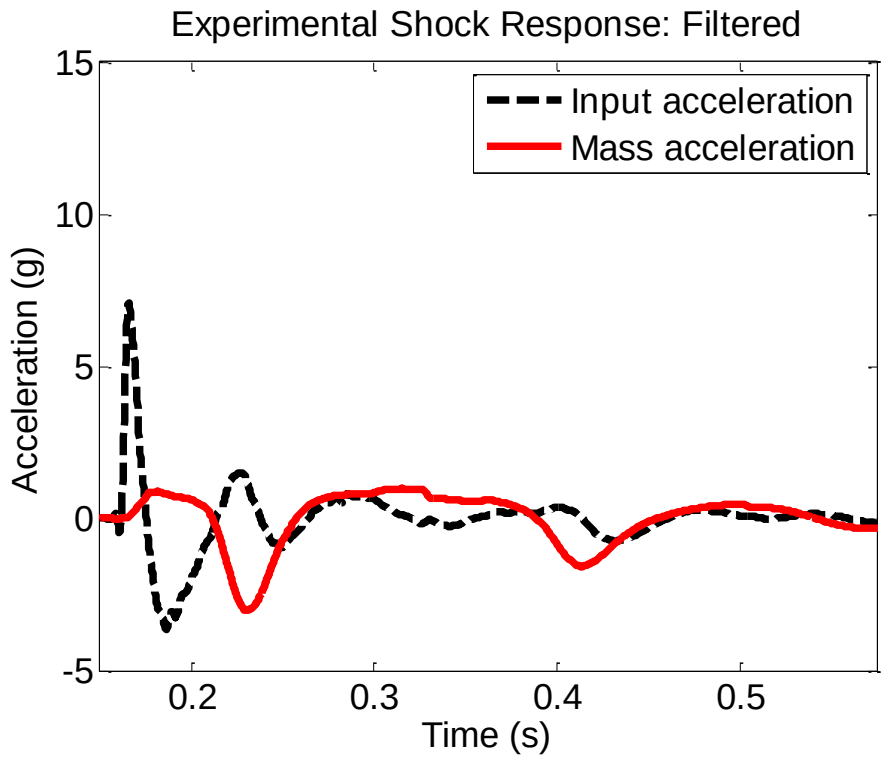

Figure 6.6. *Filtered Shock Response*

6.2.2.2 Experimental and Analytical Comparisons

Given the post-manufactured parameters listed in Table 4.2, along with the previously stated 4.76 mm compression level of the beam, the response of the system to the experimental shock data can be simulated. Comparing simulated results with the experimental data sheds light on differences between the analytical models and the physical prototypes. Using the analytical models developed in Chapter 3, the simulated response of the system is overlaid with the experimental data in Figure 6.7. The experimental input data, represented by a black dashed line, was used directly to simulate the response of the system.

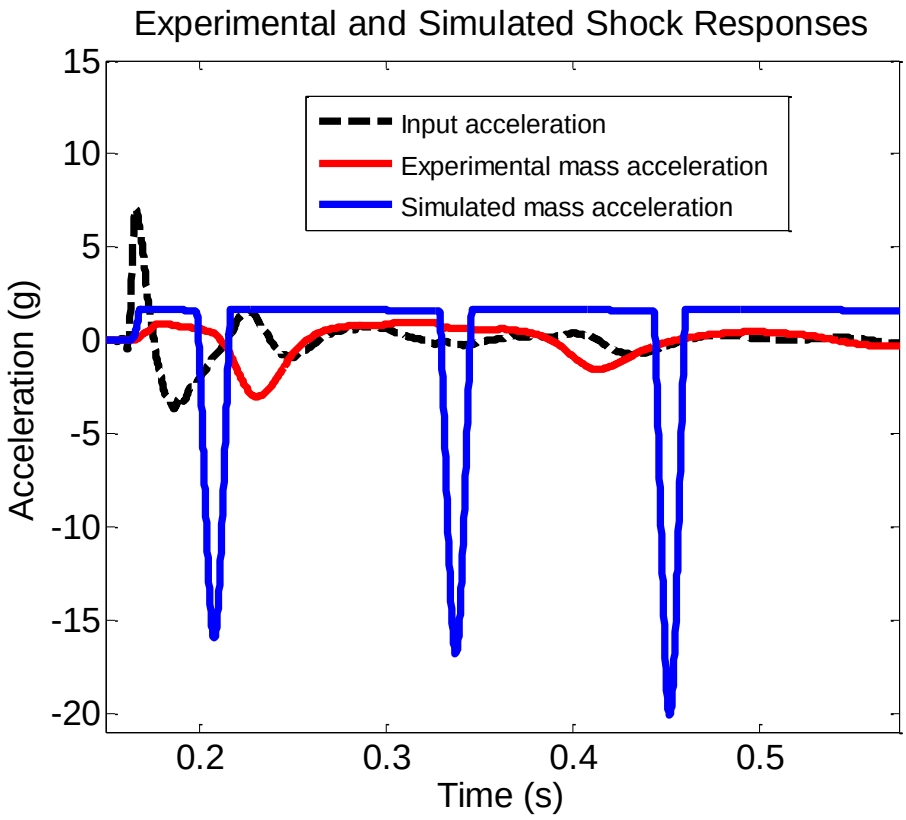

Figure 6.7. *Experimental and simulated shock response*

As seen in Figure 6.7, the experimental and simulated results share similar trends but differ in many ways as well. Both curves display shock isolation at a positive threshold acceleration level, and both curves show higher levels of negative acceleration than positive acceleration. However, the magnitudes of the negative accelerations reached in the simulation are much higher than in the experimental data. In addition, the threshold positive acceleration level is slightly higher in the simulation than in the experiment. Furthermore, although not displayed in Figure 6.7 for purposes of comparison, the simulated system requires much more time to return to steady-state.

Primary reasons for these differences include the following: both the initial stiffness and force threshold level of the analytical constitutive curve of the beam are

higher than that of the prototype (refer to Figure 6.3), and friction between the bearing and guide rod exists in the prototype and is not accounted for in the analytical model. The lower force threshold level in the prototype explains the lower level of positive acceleration transmission, and the lower initial stiffness explains the lower level of negative acceleration. Negative accelerations occur when the system decompresses to its stiff initial configuration, and with a lower initial stiffness, the prototype stores much of the energy through relatively large displacements and low force levels rather than through high forces and small displacements. The presence of friction in the prototype, along with the lower initial stiffness, explains why the experimental shock response returns to steady state much more quickly than the simulated response.

A more rigid, more precise prototype should be investigated in future research as a means of reducing the differences between the measured and predicted constitutive curve of the beam. The lower levels of initial stiffness in the prototype detract from the performance of the system by making the constitutive relationship less ideal for shock isolation. However, in order to more accurately model the prototype in the current research, the 4.76 mm compression constitutive data presented in Figure 6.3 can be used directly to describe the behavior of the beam. Creating a piecewise curve fit of this data yields the constitutive relationship for the beam in Equation 6.1. This equation is plotted and overlaid with the constitutive data in Figure 6.8.

$$F_t(u_y) = \begin{cases} (8.307e7)u_y^3 - (1.6944e6)u_y^2 + (1.139e4)u_y \ , \ u_y \leq 0.0054 \\ -(1.955e3)u_y + 35.70 \ , \ u_y > 0.0054 \end{cases} . \qquad (6.1)$$

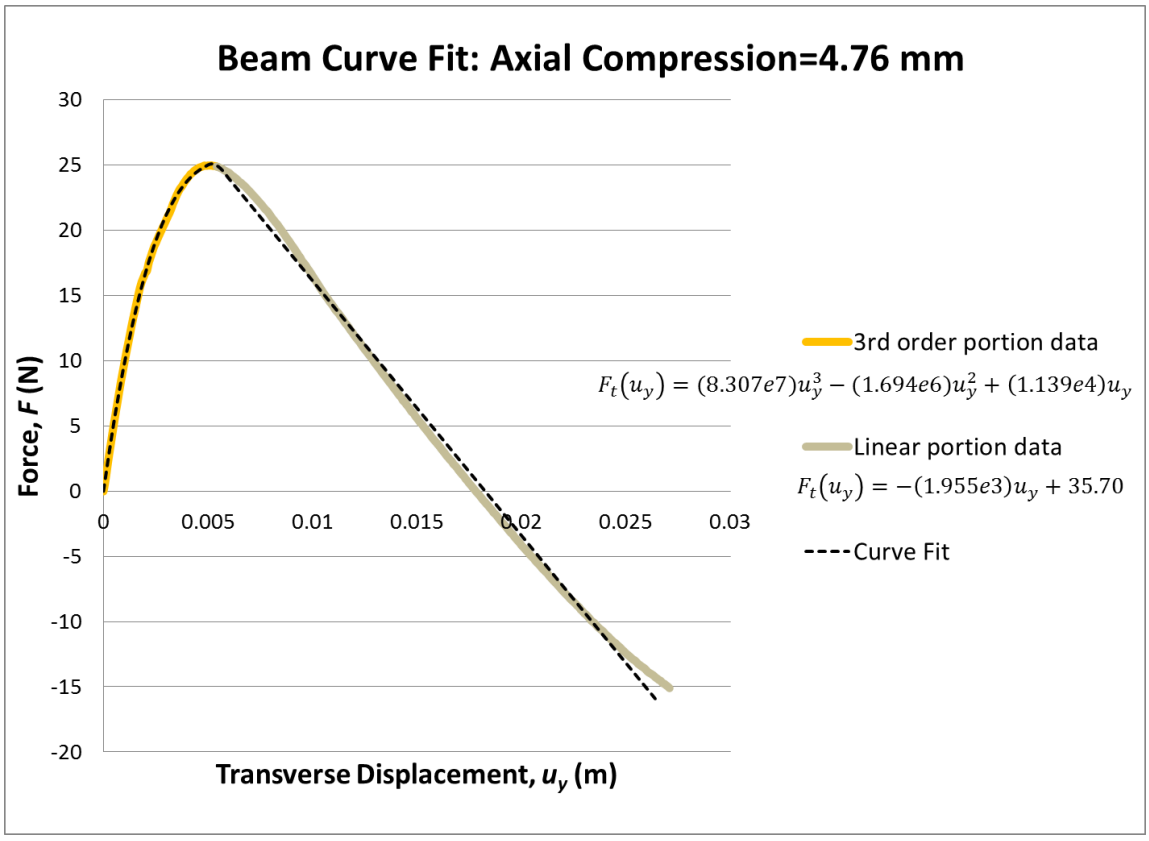

Figure 6.8. *Beam constitutive curve fit for an axial compression of 4.76 mm*

Introducing friction into the analytical model to simulate the losses between the rod and bearing also increases the accuracy of the model. An estimate of the friction forces present in the system can be obtained by examining the experimental hysteresis loop. To determine the variables needed to plot the hysteresis loop, the force can be calculated by multiplying the experimental mass acceleration data with the mass, and the relative displacement between the base and the mass can be calculated by performing two integrals of the relative acceleration with respect to time. Calculating and plotting the force against the transverse displacement of the beam yields the hysteresis loop of the system shown in Figure 6.9.

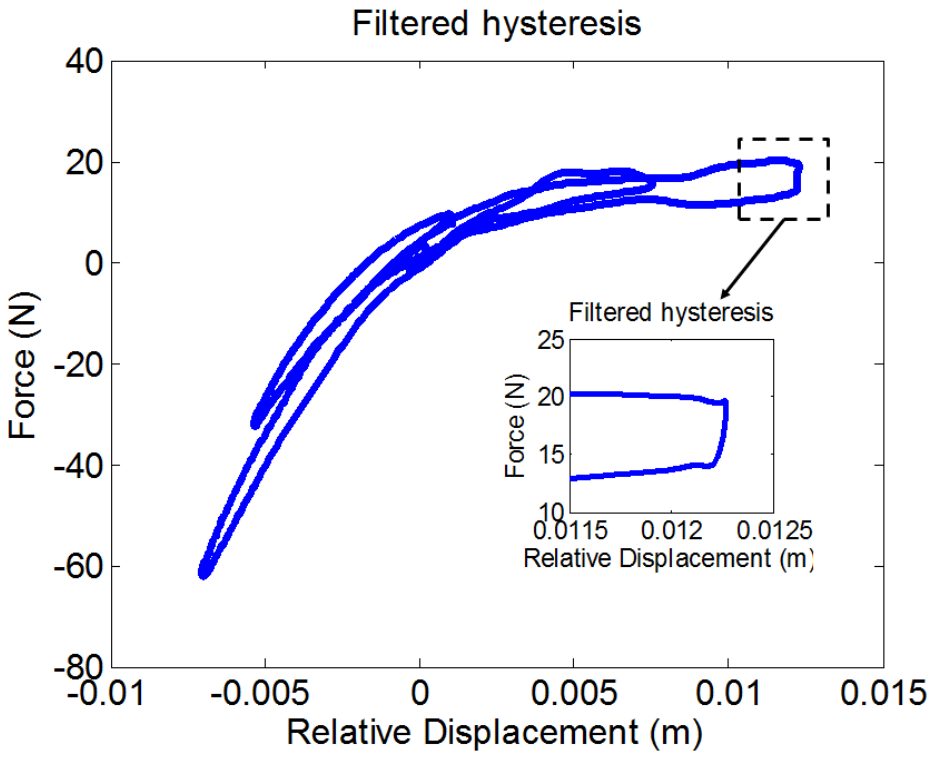

Figure 6.9. *Experimental hysteresis plot*

Although the hysteresis plot is not entirely clear, an estimation of the friction forces present can be made by examining the data closely. The change in force at the instant in which the system transitions from compressing (positive change in relative displacement) to decompressing (negative change in relative displacement) is assumed to be caused by static friction. Examining the data closely in the magnified portion of Figure 6.9, this change in force is roughly 6 N. Thus, the static force due to friction is assumed to be ± 3 N, meaning that static friction provides +3 N of force as to oppose compression and −3 N of force to oppose decompression. Kinetic friction is assumed to be ± 2.9 N for modeling purposes.

Incorporating the curve fit for the beam and the friction forces into the dynamic model of the system, the simulated shock response mimics the experimental data much

more closely. However, differences between the two responses still exist. These differences are likely a result of the inability present in the current prototype to compress the beam to a highly precise or repeatable level. Figure 6.10 shows the simulated shock response for the updated model along with the experimental response.

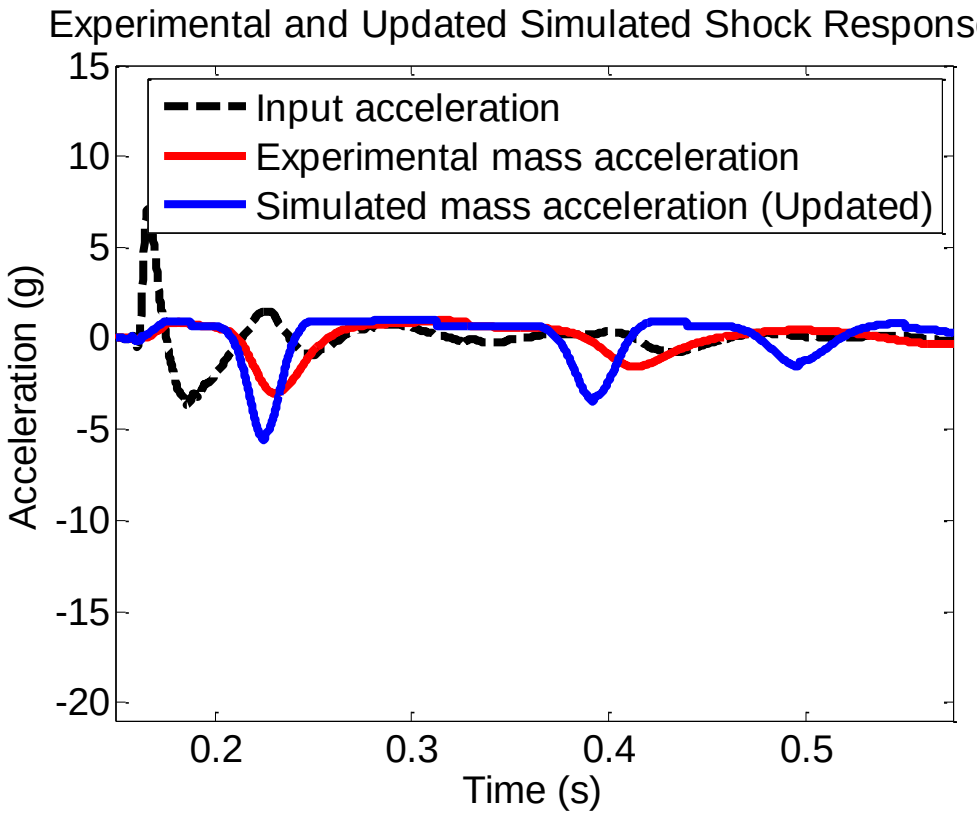

Figure 6.10. *Experimental and updated simulated shock responses*

6.3 SUMMARY

The shock isolation system was tested for its ability to isolate a mass from a base shock load. Although the lower than expected initial stiffness levels in the physical prototype detract from the overall performance of the system, the ability of the system to act as a switch to transmit shock at a given acceleration level is clearly displayed. This ability of the system to isolate at near-constant force is indicative of a system

approaching ideal shock isolation behavior. Differences between the physical and analytical constitutive relationships of the beam create inconsistencies between the experimental and analytical shock responses. Therefore, the response of the system was better predicted by measuring the constitutive relationship of the beam directly and incorporating it into the dynamic model through the use of curve fitting. However, improvements should be made to the prototype such that the measured constitutive relationship of the beam more closely matches the analytically derived relationship. Doing so will yield improved shock isolation performance due to the higher initial stiffness of the system.

Chapter 7

Closure

7.1 SUMMARY

The research presented in this thesis focuses on the modeling, design, and experimentation of systems containing negative stiffness mechanisms for vibration and shock isolation. The negative stiffness element studied in this research is an axially compressed beam. If a beam is compressed past a critical value, it becomes bistable with a region of negative stiffness in the transverse direction. In previous research, a system containing an axially compressed beam was modeled and tested for vibration isolation [7]. In the current research, variations of this model were studied and tested for both vibration and shock isolation. Furthermore, the mathematical model used to represent the compressed beam in [7] was improved and expanded in current research.

In addition to the vibration isolation system presented in [7], two systems, each including an additional beam, were studied for vibration isolation in Chapter 2. The uncoupled double-beam system contains two beams arranged horizontally in parallel. A coupling link between the beams is designed to be small such that the beams remain in parallel mechanically but have the freedom to buckle into different second-mode configurations. The coupled double-beam system contains two beams arranged vertically in parallel. A coupling link between the beams is designed such that the beams must buckle into the same mode shape when under axial compression. In addition, the coupling link is designed to prevent rotation at the midpoint of the beams, therefore

increasing the likelihood of buckling into a third-mode configuration prior to the second mode. These additional systems are designed and to display an increased level of negative stiffness compared to the single-beam system studied in [7].

Ideal shock isolation was discussed in Chapter 3. An ideal shock isolator is infinitely stiff for zero relative displacement but provides isolation at a constant force for higher displacements. When a system experiences a shock load, this constitutive relationship prevents the isolated mass from experiencing more than a threshold level of acceleration while minimizing the relative displacement required to do so. Negative stiffness can be used to approach this ideal behavior. Connecting a linear spring at the midpoint of a first-mode buckled beam creates third-order behavior that can be tailored according to the stiffness of the linear spring and the axial compression on the beam. If the beam is compressed past its third-mode buckling limit and rotation is prevented at the midpoint of the beam, it will buckle into the third mode as transverse displacement is applied. This third-mode buckling creates the piecewise behavior required to approach ideal shock isolation. If the positive stiffness of the linear spring is designed to equal the negative stiffness of the beam when buckled into the third mode, the system displays high initial stiffness under small displacements and zero stiffness for larger displacements.

As presented in Chapter 4, the vibration and shock isolation systems were fabricated in Nylon 11 through the use of Selective Laser Sintering (SLS). SLS is an additive manufacturing technology which creates components directly from CAD files by sintering powder, layer-by-layer, into a solid part. The systems were designed with modular features such that parts are readily interchangeable. Thus, various configurations can be tested using a common base structure and constraining walls, saving both the cost and time of fabricating multiple structures.

Chapter 5 presents the test results for the vibration isolation systems. Each system displays the desired trend of decreasing resonance frequency with increasing axial compression on the beams. In addition, the coupled double-beam displays higher reductions in stiffness per unit of beam compression than the other two designs. This trend indicates the potential of the coupled double-beam system to counteract stiffer positive springs and therefore support larger mass. However, the low levels of resonance frequency predicted by the analytical models in Chapter 2 are not displayed in the experimental results. Soft buckling was identified as the primary cause of error between analytical models and experimental results. Soft buckling occurs due to imperfections in the system geometry and boundary conditions. FEA modeling shows that the behavior of an axially compressed beam is highly sensitive to imperfection. Imperfections prevent the systems from reaching the near-zero system stiffness desired for low frequency vibration isolation. The uncoupled double-beam system was the most susceptible to soft buckling in this research. However, more testing should be done to determine if this result is a product of manufacturing flaws or of the design itself.

Chapter 6 presents test results for the shock isolation system. The experimental results display the ability of the shock isolation system to isolate a mass from a shock at threshold force and acceleration levels. Given a positive input acceleration of roughly 7 g's for 0.01 seconds, the system prevents the mass from experiencing no more than roughly 1 g of acceleration in the positive direction. However, the lower-than-expected levels of initial stiffness in the system detract from the overall performance of the system by creating a less ideal constitutive curve. It is suspected that flexible boundary conditions as well as creep in the buckled beam are the primary causes of this lower stiffness behavior. The differences between the constitutive curve of the prototype beam and that predicted by the analytical model in Chapter 3 are the primary cause of

inconsistencies between the simulated and experimental dynamic responses. Performing a curve fit of the measured beam constitutive relationship and inserting it into the dynamic model, the simulated results match much more closely with the experimental results. This provides a strong level of validation for the dynamic model.

7.2 FUTURE WORK

Many improvements can be made to the prototypes presented in this thesis. It has become clear through this research that the transverse behavior of axially compressed beams is highly sensitive to imperfection. While SLS technology has many characteristics beneficial to this research, such as rapid design iteration as well as a high level of design freedom, it does not have the precision required to fully demonstrate the capabilities of the systems under study. For the vibration isolation systems, the use of precision-machined metal components would greatly reduce the effects of soft buckling. Thus, lower levels of resonance frequency would be achievable. For the shock isolation system, the use of aluminum sliding walls would increase the rigidity of the system such that the walls do not flex as the beam is compressed. This should improve the alignment between the analytically modeled and experimentally measured constitutive curves of the beam. In addition, rods and bearings can be used to mate the base with the sliding walls in each system such that the walls slide smoothly with respect to the base. This smooth motion should prevent the walls from pivoting about the base as compression is applied, therefore providing purely compressive boundary conditions on the beams.

A method of providing one-way damping should be fully investigated for future use in the shock isolation system. One-way damping provides a way for the system to maintain its ideal behavior while under increasing compression and dissipate the absorbed shock energy while decompressing. As improvements are made to the shock

isolation system resulting in increased initial stiffness, one-way damping will be required to prevent the mass from experiencing high levels of negative acceleration as it returns to its initial configuration after experiencing a shock.

In future testing, the shock and vibration isolation systems will be tested in series. The high initial stiffness of the shock isolation system gives it the ability to shunt a low amplitude input load, directly transmitting it to the mass. Thus, if the shock isolation system is inserted in between a low amplitude input vibration load and a vibration isolation system, the vibrations should be transmitted directly to the vibration isolation system. However if a shock is applied to the base of the shock isolation system, the vibration isolation system should quickly reach a level of high stiffness causing the shock isolation system to absorb the shock. Thus, the nonlinear behaviors present in the shock and vibration isolation systems give the combined system the ability to isolate a mass from both vibration and shock loading. This capability can be referred to as structural logic, as the system can respond in different ways according to the loading type. In order to further explore this concept of structural logic, genetic algorithms will be employed to discover and optimize various configurations of mechanical components.

Appendix A: *MATLAB Code*

TRANSMISSIBILITY CODE

```
%Transmissibility plotting (As-Designed)
clear all;
close all;
%% Parameters

%Dimensions----------%
%Beam
lo=0.155; %Beam free length, m
w=0.008; %width, m
h=0.0025; %height, m
A=w*h; %Cross-sectional beam area, m

%Spring (double helix, so two springs)
D=0.01; %Mean coil diameter, m
d=0.00213; %Wire diameter, m
L0=0.043; %Spring free length, m
pitch=0.01; %m/rotation
Na=L0/pitch-1; %Number of active coils
N=Na+1; %Total number of coils
%--------------------------------------%

%Material properties%----------%
rho=975; %Density from [8], kg/m^3
eta=0.03; %Material loss factor from [8]
E=1225e6; %Young's Modulus from [8], Pa
G=477e6; %Shear Modulus from [8], Pa
%--------------------------------------%

%Constants----------------------------------------------------------------------%
I=w*h^3/12; %Area moment of inertia of beam, m^4
ks=(2)*G*d^4/(8*D^3*Na); %Spring stiffness, N/m ((2) because double-helix)
uxcr1=4*pi^2*I/(A*lo); %Critical beam 1st mode buckling limit
uxcr1_sys=(ks*lo^3/(2*pi^4*E*I)+1)*uxcr1; %Critical system 1st mode buckling limit
ux=uxcr1_sys*[0 0.1 0.2 0.3 0.4 0.5]; %Compression in beam, ux
ms=N*rho*(pi*D)*(pi*d^2/4); %Mass of spring, kg
mb=lo*w*h*rho; %Mass of beam, kg
maccel=0.0084; %Mass of accelerometer, kg
m=maccel+1/3*(2*ms)+0.38357*mb; %Total mass, kg (2*ms because double-helix)
```

```
wns=sqrt(ks/m); fns=wns/(2*pi) %Resonance frequency of spring and mass in
                        %rad/s and Hz
%-------------------------------------------------------------------------------%

%% Single-beam transmissibility

%Single-beam constants:
kN=2*pi^4*E*I/lo^3*(1-ux/uxcr1); %Beam transverse stiffness, N/m
K=ks+kN; %Total single-beam system stiffness, N/m
wn=sqrt(K/m); %Natural frequency of single-beam system, rad/sec
fn=wn/(2*pi); %Natural frequency of single-beam system, Hz

%Frequency vector:
f=0:0.001:100;
cs=ks*eta./(2*pi*f); %Frequency dependent dashpot coefficient

%Create H vector for each level of compression i
for i=1:length(ux);
   zeta(i,:) = cs./(2*m*wn(i)); %Damping ratio
   %Transfer function:
   H(i,:) = (j*2*zeta(i,:).*(fn(i)./f)+(fn(i)./f).^2) ./ (j*2*zeta(i,:).*(fn(i)./f)+(fn(i)./f).^2-1);
end

figure(1);
%Magnitude of H
magH=abs(H);
subplot(2,1,1);semilogy(f,magH,'LineWidth',[3]); axis tight;
uxmm=ux*1000;
label=sprintf('u_x=');
h=legend([label,num2str(uxmm(1),2)],[label,num2str(uxmm(2),2)],...
   [label,num2str(uxmm(3),2)],[label,num2str(uxmm(4),2)],...
   [label,num2str(uxmm(5),2)],[label,num2str(uxmm(6),2)],...
   'Location', 'BestOutside');
v=get(h,'title');
set(v,'string',sprintf('Axial beam \n compression (mm)'));
%set(gca,'GridLineStyle','-','MinorGridLineStyle','-','LineWidth',[0.1]);
%grid on
xlabel('Frequency (Hz)');
ylabel('Transmissibility (dB)');

%Phase of H
phaseH=180/pi*angle(H);
subplot(2,1,2); plot(f,phaseH,'LineWidth',[3]);
```

```
h=legend([label,num2str(uxmm(1),2)],[label,num2str(uxmm(2),2)],...
   [label,num2str(uxmm(3),2)],[label,num2str(uxmm(4),2)],...
   [label,num2str(uxmm(5),2)],[label,num2str(uxmm(6),2)],...
   'Location', 'BestOutside');
v=get(h,'title');
set(v,'string',sprintf('Axial beam \n compression (mm)'));
% set(gca,'GridLineStyle','-','MinorGridLineStyle','-','LineWidth',[0.1]);
% grid on
xlabel('Frequency (Hz)');
ylabel('Phase (degrees)');

%% Double-beam transmissibility
kN2=2*kN; %Double-beam transverse stiffness, N/m
K2=ks+kN2; %Total double-beam system stiffness, N/m
wn2=sqrt(K2/m); %Natural frequency of double-beam system, rad/sec
fn2=wn2/(2*pi); %Natural frequency of double-beam system, Hz

%Create H vector for each level of compression i
for i=1:length(ux);
   zeta(i,:) = cs./(2*m*wn2(i)); %Damping ratio
   %Transfer function:
   H2(i,:) = (j*2*zeta(i,:).*(fn2(i)./f)+(fn2(i)./f).^2) ./
(j*2*zeta(i,:).*(fn2(i)./f)+(fn2(i)./f).^2-1);
end

figure(2);
%Magnitude of H2
magH2=abs(H2);
subplot(2,1,1);semilogy(f,magH2,'LineWidth',[3]); axis tight;
h=legend([label,num2str(uxmm(1),2)],[label,num2str(uxmm(2),2)],...
   [label,num2str(uxmm(3),2)],[label,num2str(uxmm(4),2)],...
   [label,num2str(uxmm(5),2)],[label,num2str(uxmm(6),2)],...
   'Location', 'BestOutside');
v=get(h,'title');
set(v,'string',sprintf('Axial beam \n compression (mm)'));
%set(gca,'GridLineStyle','-','MinorGridLineStyle','-','LineWidth',[0.1]);
%grid on
xlabel('Frequency (Hz)');
ylabel('Transmissibility (dB)');

%Phase of H2
phaseH2=180/pi*angle(H2);
subplot(2,1,2); plot(f,phaseH2,'LineWidth',[3]);
```

```
h=legend([label,num2str(uxmm(1),2)],[label,num2str(uxmm(2),2)],...
    [label,num2str(uxmm(3),2)],[label,num2str(uxmm(4),2)],...
    [label,num2str(uxmm(5),2)],[label,num2str(uxmm(6),2)],...
    'Location', 'BestOutside');
v=get(h,'title');
set(v,'string',sprintf('Axial beam \n compression (mm)'));
% set(gca,'GridLineStyle','-','MinorGridLineStyle','-','LineWidth',[0.1]);
% grid on
xlabel('Frequency (Hz)');
ylabel('Phase (degrees)');
```

MSD SIMSCAPE MODEL

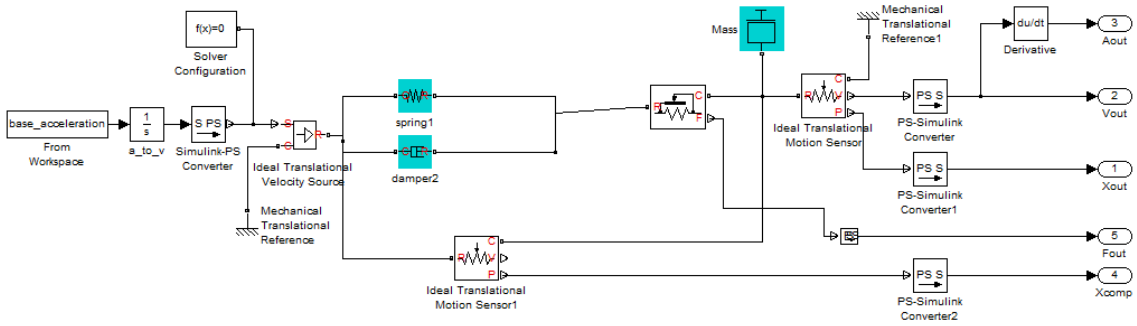

MSD SET PARAMETERS FUNCTION

```
function setparams(slua_name,x)

if nargin==0
    slua_name = 'baseline';
    x = [19168 783];
    load_system(slua_name);
end

set_param([slua_name '/spring1'],'spr_rate',num2str(x(1),10));
set_param([slua_name '/damper2'],'D',num2str(x(2),10));

if nargin==0
    close_system(slua_name,1);
end

end
```

MSD SHOCK RUN FUNCTION

```
%[xmax amax]=runshock(slua_name,x) returns the maximum overall compression
%and acceleration in the shock isolation system "slua_name"
%
%if slua_name='baseline', x=[k c]
%where k=spring stiffness, c=damper coefficient
function [xmax amax] = runshock(slua_name,x)
if nargin==0
   slua_name = 'baseline';
   x = [1682.86 41.80]; %[k c]
   load_system(slua_name);
end
%%
%Shock load
A = 10*9.80665;  %m/s^2, shock input amplitude
T = 0.01; %seconds, shock time duration
T2 = 200; %seconds, time to the next shock
dt = 0.0001;
N = 30/dt + 1; %the number of time samples for the shock
evalin('base','clear all');
evalin('base','global base_acceleration');
global base_acceleration;
base_acceleration = zeros(N,2);
Tnext = 1;
shocked = false;
for i=1:N
   base_acceleration(i,1)=(i-1)*dt;
   if base_acceleration(i,1)>=Tnext && base_acceleration(i,1)<=Tnext+T
      base_acceleration(i,2)=(A/2)*(1-cos(2*pi()*base_acceleration(i,1)/T));
      shocked = true;
   elseif shocked
      Tnext = Tnext + T2;
      shocked = false;
   end
end
%%
%Run Simulation
if nargin==0
   setparams(slua_name,x);
end
[t,x,y] = sim(slua_name);

Xout=y(:,1);
```

```
Vout=y(:,2);
Aout=y(:,3);
xcomp=y(:,4);
Fout=y(:,5);

% %Plots: Mass dynamics and hysteresis
set(0,'DefaultLineLineWidth',2);
set(0,'DefaultAxesFontSize',16);
% % Mass displacement------------------------
% figure(1);
% plot(t,Xout,'b');
% title('mass displacement')
% % Mass velocity----------------------------
% figure(2)
% plot(t,Vout,'r');
% title('mass velocity')
% Mass acceleration------------------------
% figure(3)
% plot(t,Aout/9.80665,'k');
% title('mass acceleration');
% Hysteresis-------------------------------
figure(4);
plot(xcomp,Fout,'b'); hold on;
title('Linear MSD Hysteresis','FontWeight','bold');
xlabel('Compression (m)');
ylabel('Force (N)');
%legend(sprintf('A_s=10g'),sprintf('A_s=12g'),sprintf('A_s=14g'),...
   %sprintf('A_s=16g'),sprintf('A_s=18g'));
%Compression------------------------------
% figure(5);
% plot(t,xcomp);
% title('Compression');
% xlabel('time (t)');
% ylabel('compression (m)');
%%
%Results
xmax = max(y(:,4));
amax = max(y(:,3))/9.80665;

if nargin==0
   close_system(slua_name,0);
end
```

```
end
```

MSD SHOCK OPTIMIZATION FUNCTION

```
%optimize.m
function [xbest fbest] = optimize()

clear all; close all;
evalin('base','clear all');
evalin('base','close all');
if nargin==0
   targets = [0.1 0.0025 1.45];%[0.1 0.1 2]; %target vib. g's, compression, and shock g's
   weights = [0.0 0.001 0.999]; %weights of targets
end
slua_name='baseline';
load_system(slua_name);

%% Set initial parameters and bounds
lb = [0 0];
ub = [inf inf];
x0 = [5000 30]; %[k c]

%% Set up Nelder Mead optimization
its = 0;
options = optimset('Display','iter','TolFun',1e-5,'TolX',inf);
[xbest,fbest]=fminsearch(@(x) obj_Nelder(x),x0,options);
xbest
fbest

if nargin==0
   close_system(slua_name,0);
end

%% Nelder-Mead Optimization Functions
function o = objEval_Nelder(y)
   vars = y(1:length(x0)); %store objective variables for penalty check
   y = y((length(vars)+1):(length(vars)+3));%store outputs for obj fn calc
   %Apply compromise programming
   d=(y-targets)./targets;
   if d(1)<0;
      d(1)=0;
   end
   if d(2)<0;
```

```
    d(2)=0;
  end
  if d(3)<0;
    d(3)=0;
  end
  o = sum(weights.*d.^2);
end

function o = obj_Nelder(x)
  its = its + 1;
  Neg=sum(x<=0);
  if Neg>0;
    o=inf;
  else
  setparams(slua_name,x);
  %amaxss = runvibe(slua_name,x);
  amaxss = 0.0;
  [xmax amax] = runshock(slua_name,x);
  o = objEval_Nelder([x amaxss xmax amax]);
  disp([num2str(its) ', amaxss=' num2str(amaxss,3) ', xmax=' num2str(xmax,3) ...
    ', amax=' num2str(amax,3) ', obj=' num2str(o,3)...
    ', k =' num2str(x(1),3) ', c=' num2str(x(2),3)]);
  end
end
%%
function stop = outfun(x,optimValues,state)
  stop = false;
end
end
```

SHOCK ISOLATION SYSTEM SET PARAMETERS FUNCTION

```
function Set=setparams(slua_name,BeamConstitEqn,gravity,x)
  load_system(slua_name);
  if gravity==true;
    g=-9.80665;
  else
    g=0;
  end
  set_param([slua_name '/Gravity'],'Value',num2str(g,10));
  if BeamConstitEqn==true; %Analytical beam equation is used
    E=1613.97*10^6;
    Sy=30*10^6;
```

```
rho=7850;
eta=0.03;

l=x(1);
h=x(2);
w=x(3);
delta=x(4);
cOWD=x(5);
m=x(6);

%Calculate F(x) parameters of the beam:
Area=w*h;
I=w*h^3/12;
ux=delta*l;
uxcr1=4*pi^2*I/(Area*l);
Pcr3=4*(2*pi)^2*E*I/(l^2);
uxcr3=4*(2*pi)^2*I/(Area*l);
uy0=2*sqrt(1/3*h^2*(ux/uxcr1-1))
kN3=(2*pi^4*E*I/l^3)*(1-uxcr3/uxcr1)
%Set spring stiffness equal to negative stiffness in beam
ks=abs(kN3)
%Calculate interesting design parameters:
F_thresh=-kN3*uy0
deltamax=(((Sy+Pcr3/Area)*l/(4*E*pi*h))^2*l+uxcr3)/l %third-mode
                                    %stress constraint
ksys_init=(2*pi^4*E*I/l^3)*((2*ux+uxcr3)/uxcr1-3)
wn=sqrt(ksys_init/m)
fn=1/(2*pi)*wn
%Calculate the viscoelastic damping coefficient from the springs
cs=ks*eta/sqrt(ksys_init/m);
%Translate nonlinear equation to Ax^3+Bx form (for the Simscape
%block)
A=(2*pi^4*E*I/l^3)*(Area/(16*I)) %Third-order term
B=(2*pi^4*E*I/l^3)*(1-ux/uxcr1) %First-order term

load_system(slua_name);

%Set Simscape Parameters
set_param([slua_name '/Beam'],'A',num2str(A,10));
set_param([slua_name '/Beam'],'B',num2str(B,10));
set_param([slua_name '/Beam'],'kN3',num2str(kN3,10));
set_param([slua_name '/Beam'],'uy0',num2str(uy0,10));
set_param([slua_name '/Spring'],'spr_rate',num2str(ks,10));
```

```
    set_param([slua_name '/OneWayD'],'D',num2str(cOWD,10));
    set_param([slua_name '/LVD'],'D',num2str(cs,10));
    set_param(slua_name,'MaxConsecutiveZCsMsg','none');
    set_param([slua_name '/Mass'],'mass',num2str(m,10));

  else %Curve-fit beam equation is used
    A=x(1);
    B=x(2);
    k_init=x(3);
    IntX=x(4);
    LO=x(5);
    kN3=x(6);
    c_OWD=x(7);
    m=x(8);
    cs=10;
    ks=2097.8;

    set_param([slua_name '/InstronBeam'],'A',num2str(A,10));
    set_param([slua_name '/InstronBeam'],'B',num2str(B,10));
    set_param([slua_name '/InstronBeam'],'k_init',num2str(k_init,10));
    set_param([slua_name '/InstronBeam'],'IntX',num2str(IntX,10));
    set_param([slua_name '/InstronBeam'],'LO',num2str(LO,10));
    set_param([slua_name '/InstronBeam'],'kN3',num2str(kN3,10));
    set_param([slua_name '/Spring'],'spr_rate',num2str(ks,10));
    set_param([slua_name '/OneWayD'],'D',num2str(c_OWD,10));
    set_param([slua_name '/LVD'],'D',num2str(cs,10));
    set_param(slua_name,'MaxConsecutiveZCsMsg','none');
    set_param([slua_name '/Mass'],'mass',num2str(m,10));
  end

end
```

SHOCK ISOLATION SYSTEM RUN FUNCTION

```
clear all;
clc
slua_name='ShockIso';
load_system(slua_name);
gravity=true; %true=the force due to gravity on the mass is active
%General Parameters: (c=oneway damper, m=mass)
cOWD=0.01;m=2.1; %[cOWD=200 for analytical plots in Chapter 3]
BeamConstitEqn=true; %true="beam" block is used in the Simscape model
                     %false="InstronBeam" block is used in the Simscape
```

```
                %model
if BeamConstitEqn==true;
   %BeamConstitEqn Parameters: (where delta=ux/l)
   %l=0.2;   h=0.00243; w=0.0122; delta=0.01;   % Analytical parameters
                                    % (Chapter 3)
   l=0.196; h=0.00277; w=0.0127; delta=0.0243;  % Experimental parameters
                                    % (Chapter 6)
   x=[l h w delta cOWD m]
else
   %CurveFit Parameters: (all used to define the curve-fit)
   A=0.0831*1000^3; B=-1.6944*1000^2; k_init=11.391*1000; IntX=.00541678;
   LO=35.697; kN3=-1.9551*1000;
   x=[A  B  k_init  IntX LO kN3 cOWD m];
end
%%
%%Shock load
InputData=true; %True=shock input is from experimental data
            %False=shock input is from a versine profile
if InputData==true
   filtered=true; %True=experimental input is filtered, False unfiltered
   if filtered==true;
      [ti a dummy1 dummy2]=ExtractAccel;
   else
      [dummy1 dummy2 ti a]=ExtractAccel;
   end
   base_acceleration=[ti a];
else
   A = 10*9.80665;  %m/s^2, shock input amplitude
   T = 0.01; %seconds, shock time duration
   T2 = 20;
   dt = 0.0001;
   N = 1/dt + 1; %the number of time samples for the shock
   base_acceleration = zeros(N,2);
   Tnext = 0.5;
   shocked = false;
   for i=1:N
      base_acceleration(i,1)=(i-1)*dt;
      if base_acceleration(i,1)>=Tnext && base_acceleration(i,1)<=Tnext+T
         base_acceleration(i,2)=(A/2)*(1-cos(2*pi()*base_acceleration(i,1)/T));
         shocked=true;
      elseif shocked
         Tnext = Tnext + T2;
         shocked = false;
```

```
      end
   end
end
%% Run Simulation
setparamsTotal(slua_name,BeamConstitEqn,gravity,x); %Set parameters
                                        %in the Simscape model
[t,x,y] = sim(slua_name); %Run Simscape model


Xout=y(:,1);
Vout=y(:,2);
Aout=y(:,3);
xcomp=y(:,4);
vcomp=y(:,7);
Fout=y(:,8);
%% Plots
%close all;
set(0,'DefaultLineLineWidth',3)
set(0,'DefaultAxesFontSize',14)
% %Plots: Mass dynamics and hysteresis
% % Mass displacement----------------------------------------------------
% figure();
% plot(t,Xout,'b');
% title('mass displacement')
% % Mass velocity--------------------------------------------------------
% figure()
% plot(t,Vout,'r');
% title('mass velocity')
% Mass acceleration----------------------------------------------------
figure(2)
% plot(base_acceleration(:,1),base_acceleration(:,2)/9.80665,'k--'); hold on;
plot(t,Aout/9.80665); xlim([0.15 0.575]); ylim([-21 15]);
title('Experimental and Updated Simulated Shock Responses');
xlabel('Time (s)');
ylabel('Acceleration (g)');
% legend('Input acceleration','Mass acceleration')
legend('Input acceleration','Experimental mass acceleration',...
   'Simulated mass acceleration (Updated)');
% Hysteresis-----------------------------------------------------------
figure();
xrel=cumtrapz(t,vcomp);
F=m*Aout;
plot(xrel,F,'k-'); hold on;
```

```
title('Hysteresis');
xlabel('Compression (m)');
ylabel('Force (N)');
% %Hysteresis (in g's vs x)----------------------------------------------
% figure()
% plot(xcomp,Aout/9.80665); hold on;
% title('g-level');
% xlabel('Compression (m)');
% ylabel('g-level (g"s)');
% %Compression-----------------------------------------------------------
% figure();
% plot(t,xcomp);
% title('Compression');
% xlabel('time (t)');
% ylabel('compression (m)');


%%
%Results
xmax = max(xcomp);
amax = max(Aout)/9.80665;
amin = min(Aout)/9.80665;

% if nargin==0
%     close_system(slua_name,0);
% end
```

Appendix B: *SLS Parameters*

Machine Used: 3D Systems Sinterstation HiQ

Parameter	Setting
Part Bed Temperature	187 °C
Feed Bin Temperatures	142 °C
Laser Power	38 W
Inner/Outer Ratio	0.8
Scan Spacing	0.01 in
Layer Time	20 s
Layer Thickness	0.0004 in
Roller Speed	10 in/s

Bibliography

[1] "Official Website of the United States Navy." [Online]. Available: http://www.navy.mil/view_single.asp?id=71291. [Accessed: 23-Apr-2012].

[2] Barry Controls, "Isolator Selection Guide." [Online]. Available: http://www.barrycontrols.com/UserFiles/File/Engineering/iso_select(1).pdf. [Accessed: 22-Apr-2012].

[3] Barry Controls Engineering Department, "Passive Shock Isolation." [Online]. Available: http://www.barrycontrols.com/uploads/tech/PassiveShock.pdf. [Accessed: 22-Apr-2012].

[4] D. L. Platus, "Negative-Stiffness-Mechanism Vibration Isolation Systems," *SPIE*, vol. 3796, pp. 98-105, 1999.

[5] N. Zhou and K. Liu, "A tunable high-static–low-dynamic stiffness vibration isolator," *Journal of Sound and Vibration*, vol. 329, pp. 1254-1273, Apr. 2010.

[6] Carrella, M.J. Brennan, T.P. Waters, and K. Shin. On the design of a high-static-low-dynamic stiffness isolator using linear mechanical springs and magnets. Journal of Sound and Vibration, 315(3):712-720, 2008.

[7] L. B. Kashdan, "Evaluation of Negative Stiffness Elements for Enhanced Material Damping Capacity," The University of Texas at Austin, 2010.

[8] M. R. Haberman, "Design of High Loss Viscoelastic Composites Through Micromechanical Modeling and Decision Based Materials Design," Georgia Institute of Technology, 2007.

[9] Minus K Technology, "Transmissibility Curves for Vibration Isolation Tables, Platforms, Isolators & Systems." [Online]. Available: http://www.minusk.com/content/technology/transmissibility_curves_vibration_isolation_isolators_tables.html. [Accessed: 22-Apr-2012].

[10] T. Mizuno, "Vibration Isolation System Using Zero-Power Magnetic Suspension," in *IFAC 15th Triennial World Congress*, 2002.

[11] T. Mizuno, T. Toumiya, and M. Takasaki, "Vibration Isolation System Using Negative Stiffness," *JSME International Journal*, vol. 46, no. 3, pp. 807-812, 2003.

[12] F. Cottone, H. Vocca, and L. Gammaitoni, "Nonlinear energy harvesting.," *Physical review letters*, vol. 102, no. 8, Feb. 2009.

[13] R. S. Lakes, T. Lee, A. Bersie, and Y. C. Wang, "Extreme damping in composite materials with negative-stiffness inclusions.," *Nature*, vol. 410, no. 6828, pp. 565-567, 2001.

[14] H. M. Paynter, "The Gestation and Birth of Bond Graphs," 2000. [Online]. Available: http://www.me.utexas.edu/~longoria/paynter/hmp/Bondgraphs.html. [Accessed: 22-Apr-2012].

[15] D. C. Karnopp, D. L. Margolis, and R. C. Rosenberg, *System Dynamics: Modeling, Simulation, and Control of Mechatronic Systems*, 5th ed. Hoboken, NJ: John Wiley & Sons, Inc., 2012.

[16] D. J. Inman, *Engineering Vibration*, 3rd ed. Upper Saddle River, NJ: Prentice Hall, 2008.

[17] P. Albuzhev, *Vibration Protection and Measuring Systems with Quasi-Zero Stiffness*. Hemisphere Publishing Company, 1989.

[18] M. Vangbo, "An analytical analysis of a compressed bistable buckled beam," *Sensors and Actuators A: Physical*, vol. 69, no. 3, pp. 212-216, 1998.

[19] R. G. Budynas and J. K. Nisbett, *Shigley's Mechanical Engineering Design*, 8th ed. New York, NY: McGraw-Hill, 2008.

[20] D. Shahan, B. Fulcher, C. C. Seepersad, M. R. Haberman, and P. S. Wilson, "Robust design of negative stiffness elements fabricated by selective laser sintering," in *Solid Freeform Freeform Fabrication Symposium*, 2011.

[21] K. Hoffmann, "Applying the Wheatstone Bridge Circuit." [Online]. Available: http://www.hbm.com.pl/pdf/w1569.pdf. [Accessed: 22-Apr-2012].

[22] D. Shahan, B. Fulcher, C. C. Seepersad, M. R. Haberman, and P. S. Wilson, "INTUNE Structural Logic Program R&D Status Report (August 2011)." 2011.

Vita

Benjamin Fulcher was born in Temple, Texas and attended Belton High School. He entered the mechanical engineering department at The University of Texas at Austin in 2006 and graduated with Honors in 2010. While an undergraduate student UT Austin, he was an active member of the Tau Beta Pi Engineering Honor Fraternity. Upon receiving his Bachelor's degree in 2010, he entered the Master's program in mechanical engineering at UT Austin. He graduated from UT Austin with a Master's degree in mechanical engineering in 2012.

Email Address: bafulcher@utexas.edu

This thesis was typed by the author.